Structure and Dynamics of Gap Junction Membrane Channels

Ali Khalid Khan
Charlottesville, VA

Bachelor of Science in Chemistry, University of Virginia, 2009

A Dissertation presented to the Graduate Faculty of the University of Virginia in Candidacy for the Degree of Doctor of Philosophy

Department of Molecular Physiology and Biological Physics

University of Virginia
August 2018

Abstract

Gap junction channels (GJC) form at cell-to-cell interfaces and are composed of hexameric hemichannels called connexons that dock end-to-end across the narrow extracellular gap. This allows direct intercellular exchange of ions and important metabolites up to ~15 Å in diameter. Connexins are the monomeric substituents of connexons and constitute a family of polytopic membrane proteins that have four transmembrane α-helices (TMD), two extracellular loops (E1 and E2), and three cytoplasmic domains (N-terminus (NT), intracellular loop (CL), and C-terminus (CT)).

GJCs are essential to most types of mammalian tissue, and channel dysfunction can lead to a wide variety of pathological defects. In the heart, cardiac gap junctions are responsible for the propagation of action potentials between adjacent myocytes by mediating intercellular ionic conduction. Consequently, they play a critical role in normal conduction and also in triggering fatal arrhythmias. In the cochlea, the Cx26 GJC plays a key role in K^+ recycling, and over 100 point mutations to this channel result in sensorineural hearing loss. Cx26 GJCs and hemichannels also play an essential role in maintaining keratinocyte homeostasis, and dysfunction can result in several types of skin disease. In Schwann cells, the Cx32 GJC facilitates cytoplasmic continuity between myelin sheets, and mutations to any domain of this protein results in X-linked Charcot-Marie-Tooth disease (CMT).

In the scenario of myocardial infarction, anaerobic respiration leads to low intracellular pH, which inhibits GJCs. We used single-particle, electron cryo-microscopy (cryoEM) and mass spectrometry to identify conformational changes associated with pH-

mediated regulation. The cryoEM structure of the Cx26 GJC at neutral pH recapitulated the previous GJC crystal structures. The GJC structure was well defined within the transmembrane and extracellular domains, whereas the N-terminal domains were conformationally heterogenous. Three-dimensional classification of particles at pH 6.4 revealed two conformational states, one resembling the physiological pH structure and another with pore-occluding densities. Lysine crosslinking with tandem mass spectrometry revealed closer association between the N-terminal domains and the cytoplasmic loops at acidic pH relative to neutral pH. The cryoEM maps suggests that acidic pH results in association and ordering of the N-terminal domains to form the “ball-and-chain” gating particle.

To investigate the hemichannel structure, we expressed and purified the Cx26 hemichannel by mutating a key connexon docking residue (N176Y) in the E2 loop. Using single-particle cryoEM, we reconstructed the hemichannel reconstituted in a nanodisc membrane mimetic to 4.3 Å resolution. Our cryoEM map recapitulates the TMD of previous GJC structures and appears to be in an open conformation suggesting that hemichannels are a constitutively open and require a stimulus to close *in vivo*.

In order to better understand Cx32 in the context of CMT, we expressed and purified Cx32 GJC with a C-terminal truncation at residue 250. Though the channel displayed aggregation upon concentration in a nanodisc or amphipol membrane mimetic, the protein displayed stable behavior in FA-3 detergent. The sample in detergent will now be vitrified in order to determine the structure by single-particle cryoEM.

To optimize protein purification conditions for future structural studies of the cardiac GJC Cx43, we have screened the expression and oligomeric state of several Cx43

orthologues using fluorescence-detection size-exclusion chromatography. While expression of Cx43 was successful in HEK293 cells, detergent solubilization resulted in the channel dissociating into connexin monomers. Using the structure of the Cx26 GJC, we engineered disulfide crosslinks in either the TMD or the extracellular domain to stabilize the oligomeric state of the channel. Crosslinks in the TMD resulted in enrichment of the hemichannel species, while crosslinks in the extracellular domain resulted in the enrichment of the full GJC. The extracellular domain crosslinks suggest that the Cx43 extracellular domains adopts a conformation similar to the Cx26 extracellular docking interface to form GJCs.

Dedication

بِـسْـمِ اللهِ الرَّحْمَـانِ الرَّحِيـــم

First and foremost, I am grateful and thankful to God for enabling my education and my successes in life. I dedicate this thesis to all those that have supported me and positively influenced me to reach this large milestone in my life.

To my beloved mother and father, Dr. Rana Khalid and Dr. Khalid Khan, thank you for raising me, and encouraging me to become the best version of myself. Throughout my life, there were many ups and downs, and during all of it, you gave me your unconditional love and support that I will never be able to repay. To my brothers, extended family, in-laws, nieces, and nephews, thank you for your support and love. My life is wonderful because you all are in it.

Behind a great man is a great woman, and behind a great woman is herself. To my wife, Nadia Tanoli, thank you for love and support these past years. You made tremendous amounts of sacrifice for me in your own education and career so that I may pursue mine. Thank you for putting up with the long nights and my long rants. I am grateful that you are my best friend in life.

I would like to thank my Ph.D. mentor Dr. Mark Yeager. He gave me freedom and support in the laboratory to pursue my interests and think independently. Thank you for developing my critical thinking abilities, my ability to write, and my ability to present. Thank you for the financial support and encouragement you gave me to travel to meetings

and for introducing me to some of the best scientists of our era. You set the bar for scientific excellence and achievement very high, and in my pursuits to achieve it, my abilities transcended my own expectations. I will miss our long conversations about science, medicine, and life. Your enthusiasm for your career was contagious, and I hope I can have the same for mine.

To my laboratory colleagues, past and present, thank you for your support all these years. Dr. Brad Bennett, Dr. Susan Leonhardt, Dr. Barbie Pornillos, Dr. Kelly Dryden, Dr. Michael Purdy, and Dr. Bill McIntire, thank you for the countless hours you spent teaching me, training me, and answering my questions. You set very high standards for yourselves as scientists, which encouraged me to set the bar just as high. Maciej Jagielnicki and Xueyao Jin, it was wonderful to learn the field of electron cryo-microscopy with you two. Maciej, thank you for being my teammate on the connexin projects. Sandra Poulos, thank you for your assistance with the Cx32 project.

I want to give thanks to my Ph.D. thesis committee (Dr. Edward Egelman, Dr. Peter Kasson, Dr. Jochen Zimmer, and Dr. David Cafiso) for guiding my work and helping me stay on task. I consider you all elite scientists, and while it was tough at times, I am glad you pushed my science to be of the highest quality. I also want to thank the director of the biophysics Ph.D. program, Robert Nakamoto, for his assistance, support, and mentorship throughout my graduate career.

I would like to thank the University of Virginia Medical Scientist Training Program (MSTP) and my MSTP colleagues supporting me through medical school and graduate

school. I want to give special thanks to the MSTP director, Dr. Dean Kedes, for his kind words and support for my studies in biophysics and medicine.

I also want to thank my mentors and advisors from my years prior to the MSTP program, including Dr. David Cafiso, Dr. Jason Chruma, Dr. Vladimir Sidorov, Dr. Linda Columbus, Dr. Graeme Gerrans, Dr. Robert Burnett, Dr. William Pease, and Dr. Andrew Koch. Your support through the years enabled me to pursue my M.D. and Ph.D. degrees.

The work presented herein has been funded by Dr. Mark Yeager's NIH RO1 grant (HL48908) and my own NIH F30 grant (HL129702).

To all those mentioned and not, thank you!

Abbreviations

2D, two-dimensional;

3D, three-dimensional;

A_{280}, absorbance at 280 nm;

AFM, atomic force microscopy;

amphipol, Amphipol A8-35;

BacMam, baculovirus mediated gene transduction of mammalian cells;

BS3, bis(sulfosuccinimidyl)suberate;

CC, cross correlation;

CCD, charge-coupled device;

CH_3CN, acetonitrile;

CL, cytoplasmic loop domain;

CMC, critical micelle concentration;

CMT, Charcot-Marie-Tooth disease;

CPM, 7-diethylamino-3-(4'-maleimidylphenyl)-4-methylcoumarin;

cryoEM, electron cryo-microscopy;

CT, carboxyl-terminus domain;

CTF, contrast transfer function

CV, column volume

Cx, connexin;

Cx26, connexin 26;

Cx32, connexin 32;

Cx40, connexin 40;

Cx43, connexin 43;

Cα, carbon alpha;

Cβ, carbon beta;

d250, C-terminal truncation at residue 250

DDM, n-Dodecyl-β-D-Maltopyranoside;

DM, N-decyl-β-D-maltopyranoside;

DQE, detector quantum efficiency;

DTT, dithiothreitol;

E. coli, *Escherichia coli*

E1, extracellular loop 1 domain;

E2, extracellular loop 2 domain;

eGFP, enhanced green fluorescent protein

EM, electron microscopy;

EtOH, ethanol;

EX1, component of hydrogen-deuterium exchange kinetics;

FA-3, façade-EM;

FOS, FLAG-One-Strep tag

FSC, Fourier Shell Correlation;

fSEC, fluorescence-detection size-exclusion chromatography

GJC, gap junction channel;

Gjα1, connexin 43;

Gjα5, connexin 40;

Gjβ1, connexin 32;

Gjβ2, connexin 26;

HD, hydrogen-deuterium;

HDX, hydrogen deuterium exchange;

HEPES, (4-(2-hydroxyethyl)-1-piperazineethanesulfonic acid);

HIS, 6x-polyhistidine tag

HPLC, high-pressure liquid chromatography;

IMAC, immobilized metal affinity chromatography

M1, transmembrane helix 1;

M2, transmembrane helix 2;

M3, transmembrane helix 3;

M4, transmembrane helix 4;

MD, molecular dynamics

MES, 2-(N-morpholino)ethanesulfonic acid;

MI, myocardial infarction;

ML, maximum likelihood;

MOI, multiplicity of infection

MS, mass spectrometry;
MS/MS, tandem mass spectrometry;
MSP2N2, membrane scaffold protein 2N2;
MWCO, molecular weight cut-off;
NT, amino-terminus domain;
OG, n-Octyl-β-D-Glucopyranoside;
ON, overnight;
PCR, polymerase chain reaction;
PDB and pdb, Protein Data Bank;
PEG, polyethylene glycol;
RMSD, root-mean-square deviation;
SDS, sodium dodecyl sulfate–polyacrylamide gel electrophoresis;
SEC, size-exclusion chromatography;
Sf9, Spodoptera frugiperda
SMA, styrene maleic acid co-polymers;
SNR, signal-to-noise ratio;
Std, molecular weight standards
TBA, tetrabutylammonium;
TBSb, tetrabutylantimony;
TCEP, tris(2-carboxyethyl)phosphine;
TEV, Tobacco etch virus
TFA, Trifluoroacetic acid;
T_m, melting temperature;
TMD, transmembrane domain;
Tris, tris(hydroxymethyl)aminomethane;
UA, uranyl acetate;
WT, wild-type;

Table of Contents:

Abstract..... ii

Dedication v

Abbreviations viii

Chapter 1. Introduction 1

1.1.Structural biology of gap junction channels……..……..1
1.1.1. Functional properties of gap junction channels ……..…1
1.1.2. α-helical structure of the transmembrane domains and proposed role in closure…….....4
1.1.3. Role of the N-terminus in voltage sensing, voltage gating, and chemical gating……6
1.1.4. Role of the C-terminus in pH-mediated gating and for regulation by cytoplasmic proteins……...8
1.1.5. Hemichannel regulation……...8
1.2.Significance of gap junction channels in select human diseases…….....10
1.2.1. Heart disease……..10
1.2.1.1.Tissue injury leads to gap junction channel inhibition…..10
1.2.1.2.Comparison of the cardiac connexins, Cx43 and Cx40….13
1.2.2. Deafness……16
1.2.3. Skin Disease……...19
1.2.4. Charcot-Marie-Tooth disease…….……21

Chapter 2. pH-gating of gap junction channels: visualization of a "ball-and-chain" by cryoEM 24

2.1.Acidic pH stabilizes a conformation of the Cx26 GJC with a pore occlusion……..24
2.2.Hydrogen deuterium exchange reveals dynamic N-terminus at physiological pH…….31
2.3.Acidic pH induces movement of M2 helix……..33
2.4.Increased NT-CL association at acidic pH……..35
2.5.Concluding remarks…….38
2.6.Methods……44
2.7.Extended data figures and tables……..……56

Chapter 3. CryoEM structure of a connexin hemichannel 73

3.1.Results……..……....74
3.1.1. Expression and Purification of Cx26 hemichannels …….74
3.1.2. Sample optimization for single-particle cryoEM……...……76
3.1.3. Comparison of the Cx26 gap junction channel and hemichannel structures in a nanodisc…….…….83
3.1.4. 3D classification of hemichannel particles reveals variability in the extracellular domains…….88
3.2.Discussion……...…….93
3.3.Methods……96
3.4.Extended data figures……..…103

Chapter 4. Expression, purification, and stabilization of the Cx32 gap junction channel 105

4.1.Results……..……..……105
4.2.Discussion……...……...113
4.3.Methods……...……..……114

Chapter 5. Expression, purification, and stabilization of the cardiac gap junction channel Cx43 118

5.1.Results……120
5.1.1. FSEC analysis of Cx43 orthologues……...…120
5.1.2. Stabilization of hexameric and dodecameric channels by engineered disulfide crosslinks……...…….121
5.2.Discussion……...…….…..128
5.3.Methods……..……....130

Chapter 6. Future Directions 134

6.1.pH-gating of Gap Junction Channels: Visualization of a “ball-and-chain” by cryoEM……..……134
6.2.CryoEM structure of a connexin hemichannel……..135
6.3.Expression, purification, and stabilization of the Cx32 gap junction channel……...…136
6.4.Expression, purification, and stabilization of the cardiac gap junction channel Cx43……..….137

Appendix. Summary of single-particle cryoEM image processing 139

References.....150

Chapter 1
Introduction

1.1. Structural biology of gap junction channels

1.1.1. *Functional properties of gap junction channels*

Gap junction channels (GJCs) aggregate into plaques at cell-cell interfaces (**Figure 1.1A**) and behave as direct conduits between neighboring cells, allowing intercellular passage of ions, metabolites and other important signaling molecules of up to ~1 kDa (2). These channels are typically open under resting conditions and close in response to a variety of physiological and pathological stimuli including intercellular voltage, low intracellular pH, and increased cytoplasmic calcium concentration (3). A hemichannel, also called a connexon, is formed by a hexameric oligomer assembled in a circular arrangement with a central pore. The gap junction channel is formed by the end-to-end docking of two connexons. Different connexin isoforms can assemble in various ways. Connexons may be homomeric or heteromeric, and channels may be formed by connexons having the same or different protomeric compositions **(Figure 1.1B)**. Connexins are multi-pass α-helical membrane proteins with 4 transmembrane domains (TMDs; termed M1-M4), three cytoplasmic domains (amino terminus [NT], cytoplasmic loop [CL], and carboxyl-terminus [CT]), and 2 extracellular loops (termed E1 and E2) (**Figure 1.2**) (4, 5). A central

conducting pore appears to be a conserved motif of all gap junction channels (6). The TMDs and extracellular loops display the highest sequence conservation (7) while the 3 cytoplasmic regions have more sequence divergence. The major nomenclature in common use is to denote connexins as their kDa sizes, based on their relative monomeric mobilities on SDS-PAGE (8). An alternate naming system based on genetic similarity and docking compatibility is also used. For example, the cardiac connexins Cx40 and Cx43 belong to the α group and can be referred to as Gjα5 and Gjα1, respectively. Cx26 and Cx32 belong to the β group and can be referred to as Gjβ1 and Gjβ2, respectively (3).

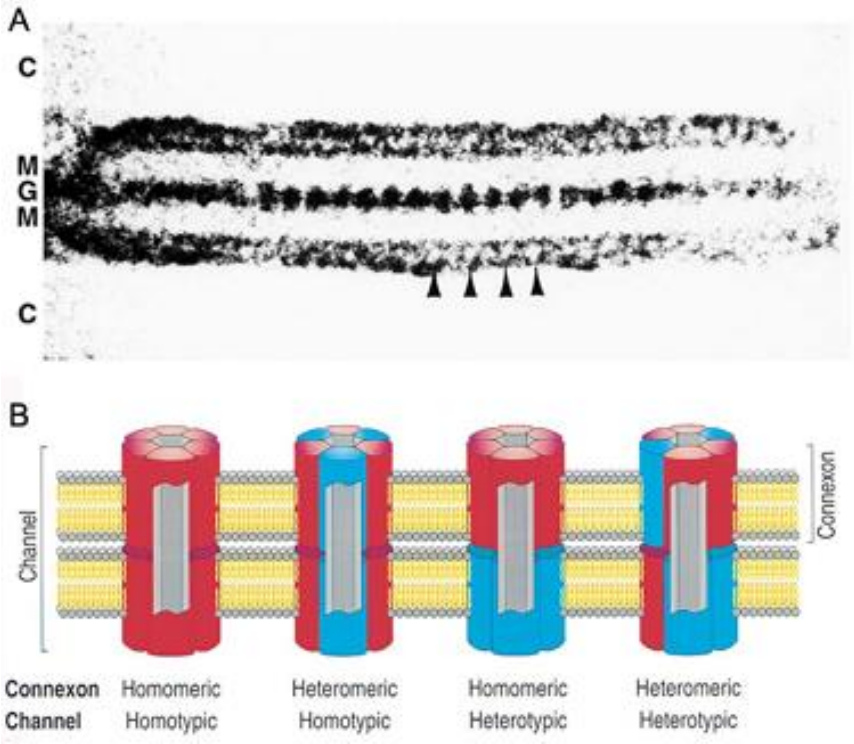

Figure. 1.1: **General organization of gap junction channels at the cell-cell interface.** (A) Negative stain EM "edge-view" image of a 2D crystal of Cx43 gap junction channels. The cytoplasmic, membrane and extracellular gap regions are indicated by the letters C, M, and G, respectively. Stain is excluded from lipid bilayer but adheres to proteinaceous regions. Image is from (9). (B) Schematic of possible connexin arrangements within connexons. Image is from (7).

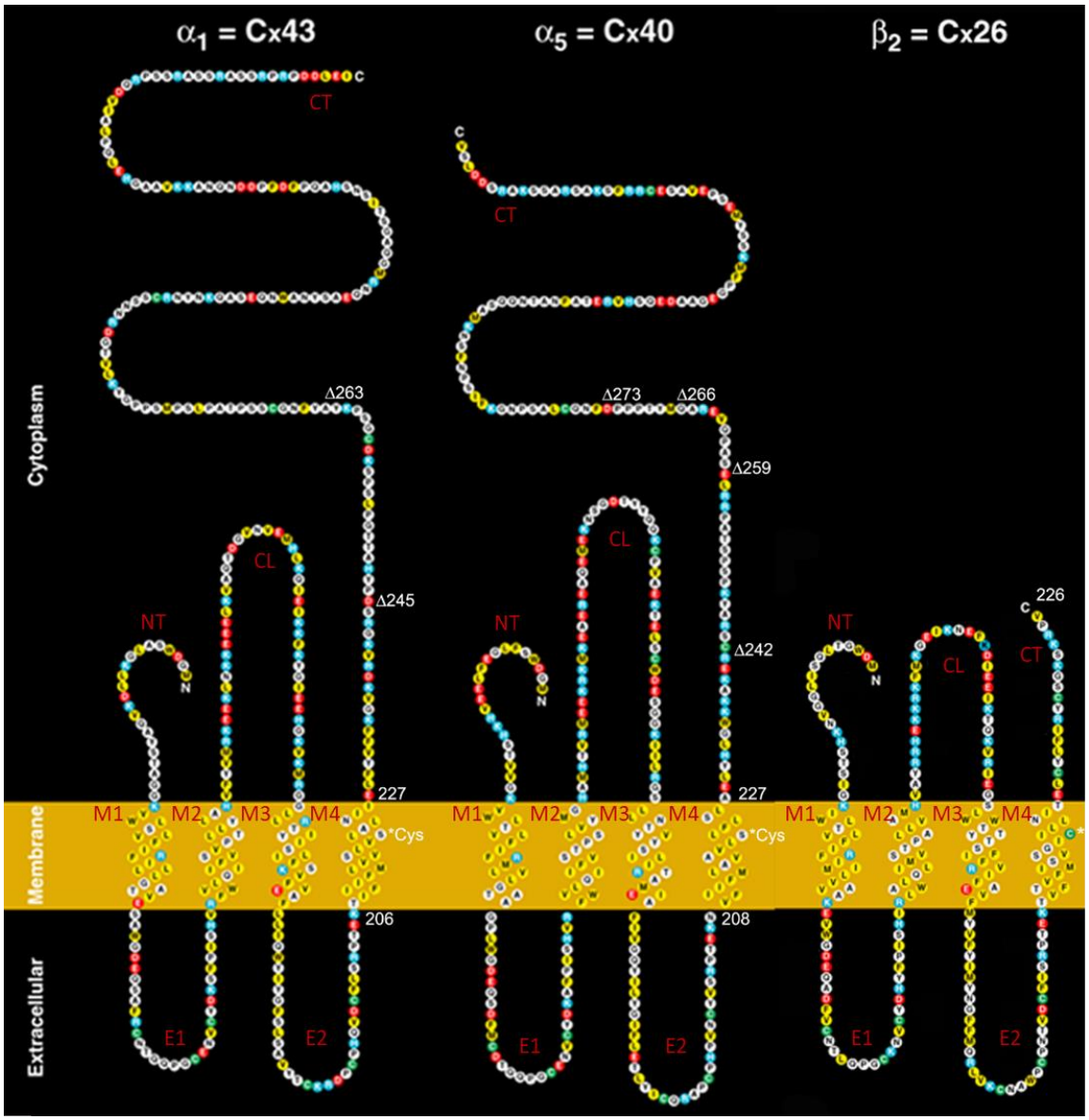

Figure 1.2: Membrane Topology of Connexin Proteins. Displayed is the topology model of Cx43, Cx40, and Cx26. Connexin protein contains four transmembrane domains (M1-M4), two extracellular loops (E1 and E2), and three cytoplasmic domains (amino terminus [NT], cytoplasmic loop [CL], and carboxyl-terminus [CT]). Image is modified from (10).

1.1.2 *α-helical structure of the transmembrane domains and proposed role in closure*

Early electron microscopy (EM) studies (11, 12) provided rudimentary measurements of gap junction channel dimensions: ~25Å connexin diameter, ~20Å pore diameter, and ~40Å extracellular gap. Early EM of rat liver gap junctions suggested that, upon exposure to a physiologically high concentration of calcium, the connexin subunits undergo a rotation that close the channel in a manner analogous to a camera iris (**Figure 1.3**) (12). Two-dimensional (2D) projections generated from EM revealed the higher order structure of gap junction channels (12, 13). Eventually, a cryo-microscopy (cryoEM) map of Cx43 at 7.5 Å in-plane resolution showed that each connexon contains 24 rod-like densities readily interpreted as individual transmembrane α-helices (14). Coupled with analysis of cryoEM data from Cx32 (15), the Cx43 projection (13) and three-dimensional (3D) maps (14) revealed that there is a 30° stagger of apposing connexons. At this resolution, the primary sequence identity of each helix could not be assigned and therefore were arbitrarily designated helices A-D (for M1-M4). To help address the ambiguity of the helical assignments, an improved cryoEM map of Cx43 **(Figure 1.4A)** (5.7 Å in-plane resolution) was used as a basis from which to generate a Cα model for the transmembrane α-helices within a connexon (16). On the basis of the map, sequence conservation, spatial arrangement and mutagenesis data, the primary sequence of M1–M4 was assigned to the observed α-helices. This assignment predicted that M1 and M3 are pore-lining and that M4 is the helix on the perimeter of the connexon, agreeing with earlier electrophysiology and mutational data (4, 17). This assignment was corrected when two X-ray crystal structures

for Cx26 were solved independently by the Tsukihara (18) and Yeager (1) laboratories **(Figure 1.4B)**, respectively, revealing that M1 and M2 are the pore lining helices.

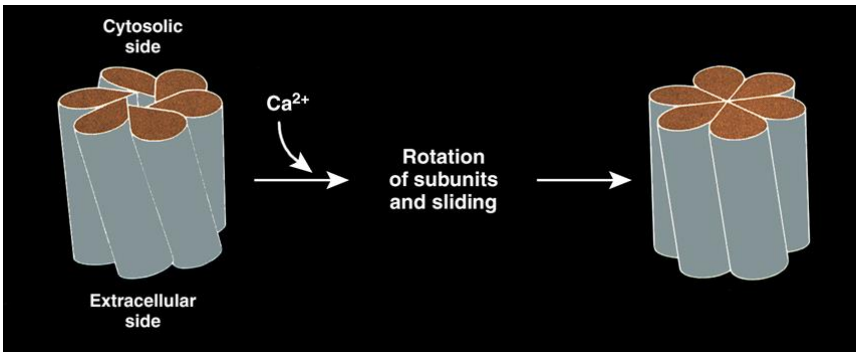

Figure 1.3. Camera-iris model for Ca^{2+} mediated gating of GJC (12). EM studies on rat liver GJCs in the presence Ca^{2+} of suggest that each connexin subunit rotates and slides in a manner similar to a camera-iris leading to closure of the pore.

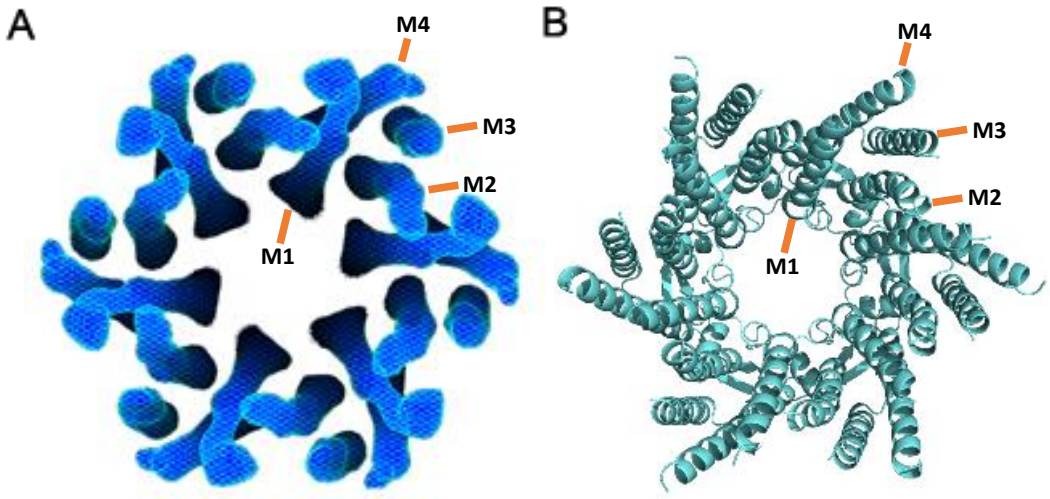

Figure 1.4: Cytoplasmic views of Cx43 and Cx26. (A) CryoEM 3D map of Cx43 at 5.7 Å in-plane resolution from 2D crystals (16). (B) X-ray crystal structure of Cx26 at 3.3 Å resolution (1). Note the conserved architecture of the helical bundle.

1.1.3 *Role of the N-terminus in voltage sensing, voltage gating, and chemical gating*

The NT has been implicated as part of the voltage sensor as well as the "gating plug" that can close over the pore or induce the TMD helices to restrict ionic flow (19). The NT may also be a general binding site for channel-modulating ligands. Cx40 (but not Cx43) binds polyamine compounds at an N-terminal site that overlaps with its voltage sensor domain (20). For Cx40 and Cx43, it has been shown that mutations of two charged residues within the NT does not affect channel conductance but does abrogate voltage-dependent gating (21). Most studies propose or assume a physical gate to the pore existing at or near the TMD/extracellular loop interface (22). 2D crystallography studies of Cx26 also suggest that the NT gates the pore in response to chemical stimuli. A 2D crystal structure of human Cx26 M34A GJC crystallized at pH 5.8 in the presence of several connexin inhibitors (Mg^{2+}, Ca^{2+}, and carbenoxolone (3)) revealed an occluding density in the channel pore (**Figure 1.5**) (23). While domain assignment of the occlusion could not be made, a follow-up 2D crystal structure with an NT deletion in residues 2 – 7 showed decreased occluding density suggesting that the NT forms the gate (24).

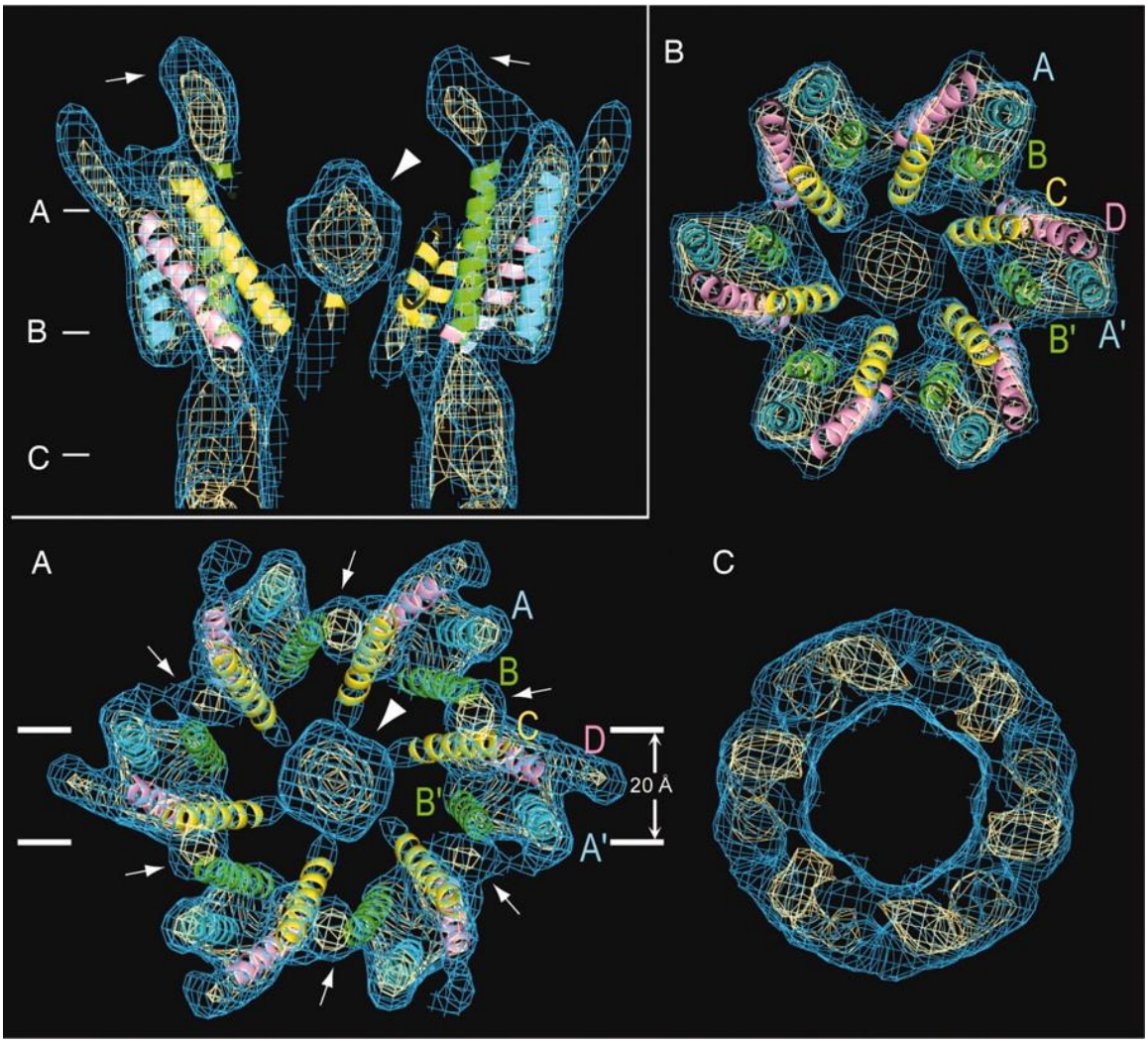

Figure 1.5: 2D crystal structure of Cx26 M34A reveals a pore occluding density. Inset on the top left shows a 25 Å thick section perpendicular to the membrane within a hemichannel. Arrows point to cytoplasmic protrusions and the arrow head points to a pore-occluding density. Panels A – C show 30 Å thick sections parallel to membrane corresponding to positions A – C marked in inset. The four transmembrane helices are labeled A (cyan, A′), B (green, B′), C (yellow), and D (pink). Image is from (23).

1.1.4 *Role of the C-terminus in pH-mediated gating and in regulation by cytoplasmic proteins*

The CT is the major scaffold for binding of intracellular proteins and is a target of post-translational modifications, containing several identified phosphorylation sites (25). Therapeutic peptides, such as rotigaptide and AAP10 (26), can re-establish gap junction intercellular communication (GJIC) in certain channels (27, 28), possibly by regulating the phosphorylation state of the CT (29). Truncations at the CT and intracellular acidification can have drastic effects on conductance. pH-induced closure of the CT is believed to be initiated by a disruption of interactions between the CT and CL (30), which leads to blocking of the pore in a “ball-and-chain” fashion, similar to voltage-gated ion channels (31).

1.1.5 *Hemichannel regulation*

Connexins expressed in cells are thought to assemble as hemichannels that are transported to the plasma membrane. The hemichannels travel to sites of gap junction plaques and dock with hemichannels in the apposed membrane to form a complete dodecameric channel (32). Numerous functional studies have shown that connexins can operate as both hemichannels and GJCs (33-35), and that they exhibit properties of both ligand and voltage-gated channels (3). The physiological roles of hemichannels and gap junction channels can be distinguished by their characteristic regulation. GJCs serve as intercellular connections and are in a constitutively open state so that tissues function as syncytia, whereas hemichannels communicate with the extracellular space and by default are in a closed state (3).

A 2002 study using atomic force microscopy (AFM) revealed conformational changes on the extracellular surfaces of Cx26 hemichannel plaques upon addition of Ca^{2+} that were consistent with the steric model of gating (**Figure 1.6**) (36). The limited resolution of the surface topography, however, did not identify which regions of the protein were undergoing conformational changes (e.g., TMD and/or extracellular loops). Although our analysis of intact GJCs suggested an electrostatic mechanism for Ca^{2+}-mediated regulation (1), it could still be the case that hemichannels are regulated by a steric mechanism. Consequently, it would be valuable to compare the structures of GJCs and hemichannels with and without Ca^{2+}.

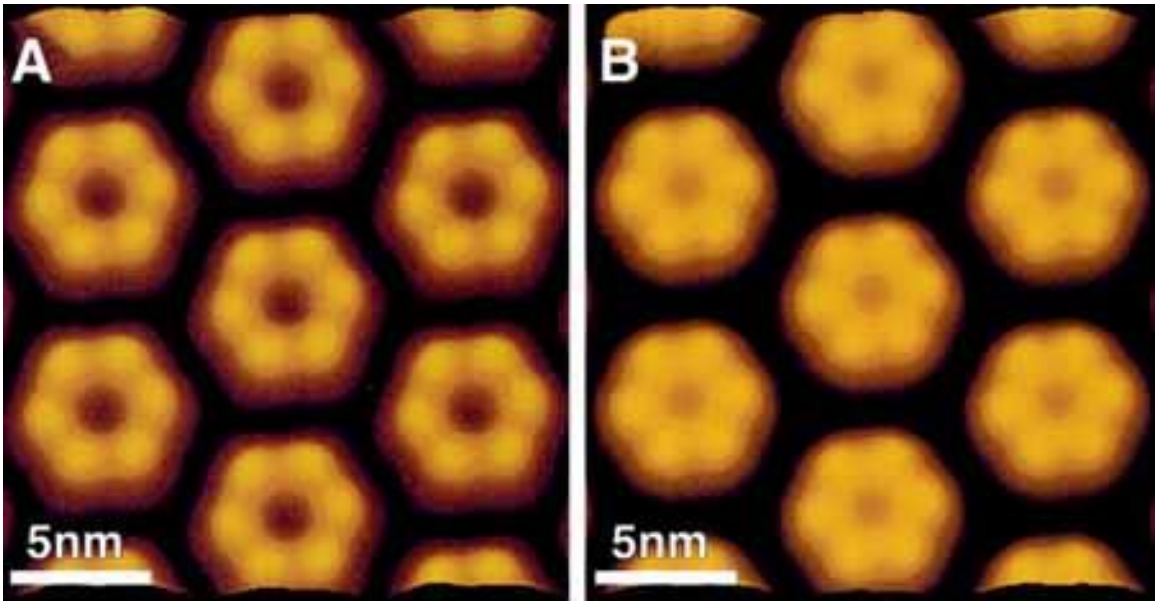

Figure 1.6. Atomic force microscopy of the extracellular surface of the Cx26 hemichannel as a function of Ca^{2+}. The extracellular surface of the Cx26 hemichannel is displayed in an idealized 2D lattice in the absence (**A**) and presence (**B**) of 0.5 mM Ca^{2+}. In the presence of Ca^{2+}, extracellular protrusions move towards the center of the pore. Images are from (36).

1.2. Significance of gap junction channels in select human diseases

1.2.1. *Heart disease*

Cardiac gap junctions electrically couple adjacent myocytes, allowing for a coordinated propagation of an action potentials through the heart (37). Following a myocardial infarction, a disruption of channel activity due to tissue injury (38) or remodeling of the junctions (39) can cause non-uniform, anisotropic current flow, which can lead to fatal ventricular arrhythmias. Currently, cardiovascular disease is the leading cause of death in the United States, and this is primarily due to myocardial infarction (MI) and sudden cardiac death from ventricular tachycardia and fibrillation. The substrates of ischemia and myocardial scarring after MI (40, 41) increases the risk for potentially lethal ventricular arrhythmias due to severe alterations in intercellular current flow and fluctuations in pH and calcium (42).

Although quite expensive, implantable defibrillators are currently the best treatment for at-risk patients to prevent sudden death (43). Antiarrhythmic drug trials have proven disappointing with some drugs actually having a pro-arrhythmic effect (44, 45). Gap junctions could be a potential antiarrhythmic target (27).

1.2.1.1 Tissue injury leads to gap junction channel inhibition

From a structural standpoint, the molecular basis for channel closure and regulation is not well understood. Such information would be valuable for the design of new classes of antiarrhythmic drugs that would specifically target gap junction channels. In the context of tissue injury such as myocardial infarction, decreased membrane integrity of

intracellular Ca^{2+} stores such as the sarcoplasmic reticulum and anaerobic respiration results in high intracellular Ca^{2+} and acidic pH, respectively. Both of these conditions lead to block of intercellular communication via GJCs. As mentioned, early cryoEM studies suggested that the TMDs close the channel by rotating in a manner similar to a camera-iris (**Figure 1.3**) (12). To explore Ca^{2+}-mediated regulation of GJCs, our group previously solved X-ray structures of the human Cx26 GJC in the presence and absence of Ca^{2+} (1). The two structures were nearly identical, ruling out both a large-scale structural change and a local steric constriction of the pore. Ca^{2+} coordination sites reside at the interfaces between adjacent subunits, near the entrance to the extracellular gap, where local, sidechain conformational rearrangements enable Ca^{2+}-chelation. Computational analysis revealed that Ca^{2+} binding generates a positive electrostatic barrier that results in ionic conduction block (**Figure 1.7**) in contrast to the previous camera-iris model (**Figure 1.3**) involving steric occlusion of the channel pore (12).

In contrast to the Ca^{2+}-induced electrostatic regulation of GJCs, closure induced by acidic pH is presumed to occur via physical occlusion by a "ball-and-chain" mechanism. Many studies suggest the gating particle is the CT portion of the protein because pH inhibition in multiple GJC isoforms, with the exception of Cx26, Cx32, Cx45 and Cx46, can be abolished by truncating the CT and restored by adding it back as a peptide (46-48). 2D crystallography studies of the Cx26 M34A at pH 5.8, however, suggests that the NT serves as a gating particle, though the crystallization conditions did contain several other GJC inhibitors that may have caused this effect (23, 24). Aside from the gating particle, an interaction between residue N14 in the NT and H100 in the M2-CL interface in Cx26 also

seems to be essential for pH gating (49). In **Chapter 2**, I will discuss our studies regarding pH regulation of GJCs that suggest pH gating is mediated by an N-terminal, oligomeric ball-and-chain mechanism.

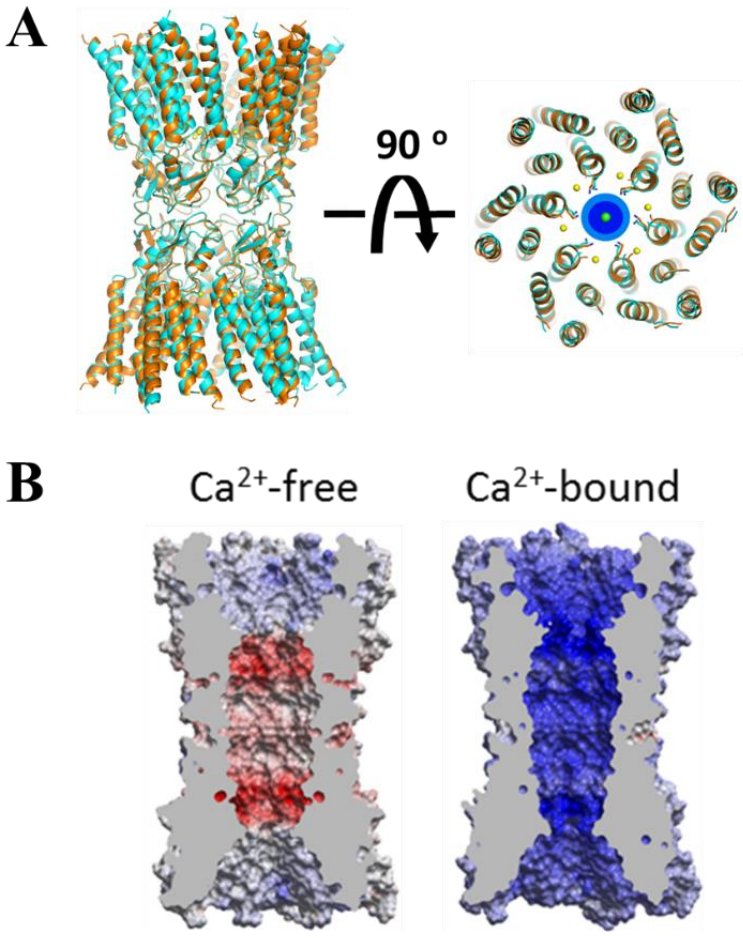

Figure 1.7. Ca^{2+} induced electrostatic block of GJCs. (**A**) Two aligned crystal structures solved in our lab of Cx26 bound (cyan) and unbound (orange) to its inhibitor Ca^{2+} (gold spheres). Binding of calcium did not cause any large scale conformational changes, and both structures can accommodate K^+ (green sphere) with two shells of hydration shown in dark and light blue. (**B**) Electrostatic surface potential calculation of the pore suggests that binding of Ca^{2+} creates a positive surface potential (blue) that blocks cation permeation. Positive and negative electrostatic potentials are shown in blue and red, respectively (color scale is -15 to 15 kT e^{-1}). Images adapted from (1).

1.2.1.2. Comparison of the cardiac connexins, Cx43 and Cx40

Cx43 and Cx40 are the most abundant heart isoforms (39). Although they share 62% sequence similarity (75% within their putative TMD helices), Cx40 and Cx43 possess significantly different conductance properties (25) and cardiac expression profiles. Cx40 is primarily enriched in the His-Purkinje fibers and in specialized conducting tissue in the atrioventricular node, whereas Cx43 is distributed throughout the myocardium (**Figure 1.8)**. Cx43 has a larger limiting pore diameter yet has a single channel conductance at a markedly reduced rate (~100 pS) compared to Cx40 (~200 pS) (50). Cx40 maintains an ionic selectivity ratio favoring passage of cationic species (4:1 cation/anion) whereas Cx43 is not strongly selective (51). The structural basis for these functional differences remains a mystery, and electrostatic surface potential calculations of Cx40 and Cx43 homology models based on the Cx26 structure did not reveal any significant differences (**Figure 1.9**). We hypothesize that the discrepancy between pore diameter and conductance properties has two possible explanations. First, the conductance rate is a result of electrostatics dictated by the pore lining residues. Second, it is possible that the pore structure is quite dynamic with many sub-states existing when the channels are going from a closed to an open state (or vice-versa). The pore diameters of Cx40 and Cx43 were originally determined indirectly by observing the permeation of different sized substrates through the channels (52, 53). If the pore is dynamic, previous experiments may have been limited to observe a single state. Ultimately, obtaining high-resolution structures of Cx40 and Cx43 can help elucidate these differences. **Chapter 5** will discuss our studies towards expression and stabilization of Cx43 for high-resolution structure determination via cryoEM.

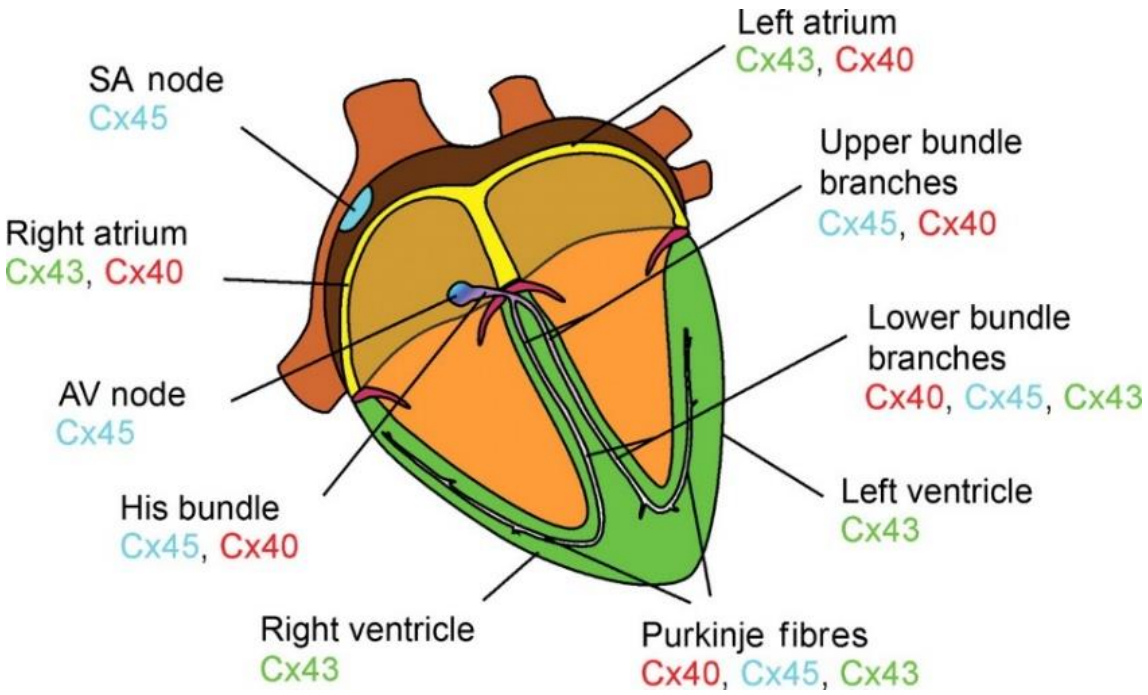

Figure 1.8: Connexin expression patterns in the mammalian heart. Image from (39).

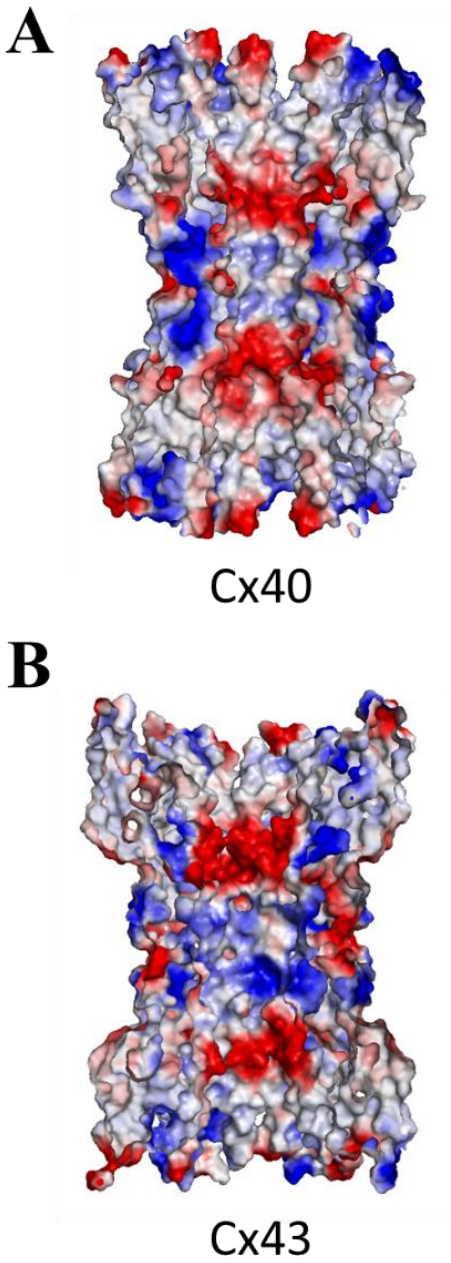

Figure 1.9. Electrostatic surface potential calculations of Cx40 and Cx43 homology models reveal no significant differences. Electrostatic surface potentials of the Cx40 (**A**) and Cx43 (**B**) were calculated using the vacuum electrostatics feature in PyMOL (Schrödinger, LLC). Homology models were generated based on the structure of the Cx26 GJC (1) using the program Modeller (54, 55).

1.2.2. *Deafness*

Occurring in roughly 1 to 2 births out of 2000, the most common gap junction mutation-linked pathology is sensorineural hearing loss (56, 57). GJC mediate K^+ recycling in the cochlea (**Figure 1.10**). Stimulation of hair cells results in K^+ influx via mechanosensitive K^+ channels, followed by K^+ absorption into supporting cells by the KCC4 K^+/Cl^- co-transporter. K^+ then passes through a network of supporting cells and fibrocytes via gap junctions Cx26 and Cx30 until it reaches the endolymph through the stria vascularis. It is prominently hypothesized that gap junction dysfunction results in a toxic accumulation of K^+ in hair cells leading to cell death and hearing loss (58). Approximately 170 mutations have been identified in Cx26 resulting in syndromic or non-syndromic deafness (56). While most common of these are deletion mutations that cause frameshift or truncation of the protein, over 100 of these mutations are single point mutants (57, 58). Among the specific point mutations that form functional junctional channels (**Figure 1.11**), structural details are lacking; however, the crystal structure of Cx26 bound to Ca^{2+} revealed that the calcium coordination site coincides with a cluster of mutations at the M1/E1 boundary (1). Our group is interested in studying the structural consequences of mutations involved in Ca^{2+} binding via X-ray crystallography, but thus far, mutant protein constructs have shown weak diffraction or have been difficult to crystallize. Our cryoEM studies discussed in **Chapter 2** highlight a more efficient method for determining high-resolution structures of the Cx26 GJC and can facilitate structure determination of Cx26 deafness mutants without the need for crystallization.

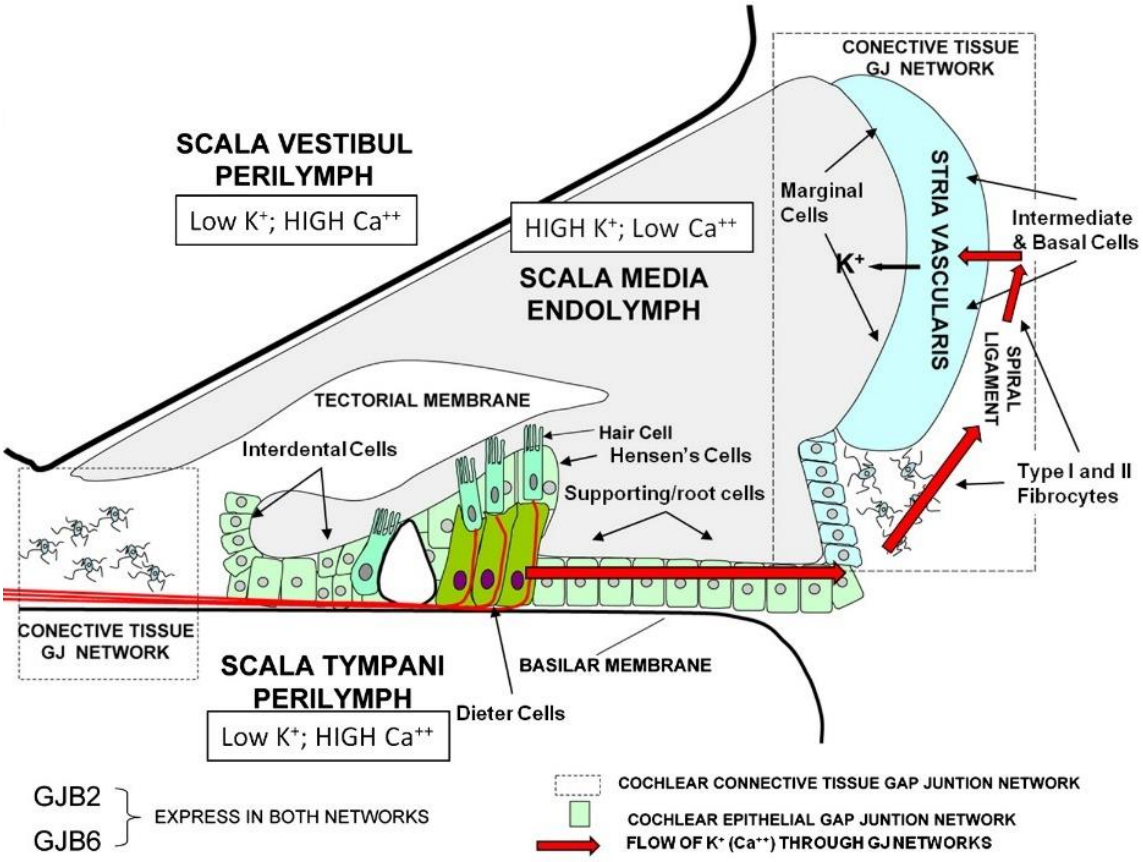

Figure 1.10. K^+ recycling in the human cochlea. K^+ flow (red arrow) from the hair cells passes through supporting/root cells and fibrocytes via gap junction channels Cx26 (Gjβ2) and Cx30 (Gjβ6) until reaching the endolymph. Image is from (58).

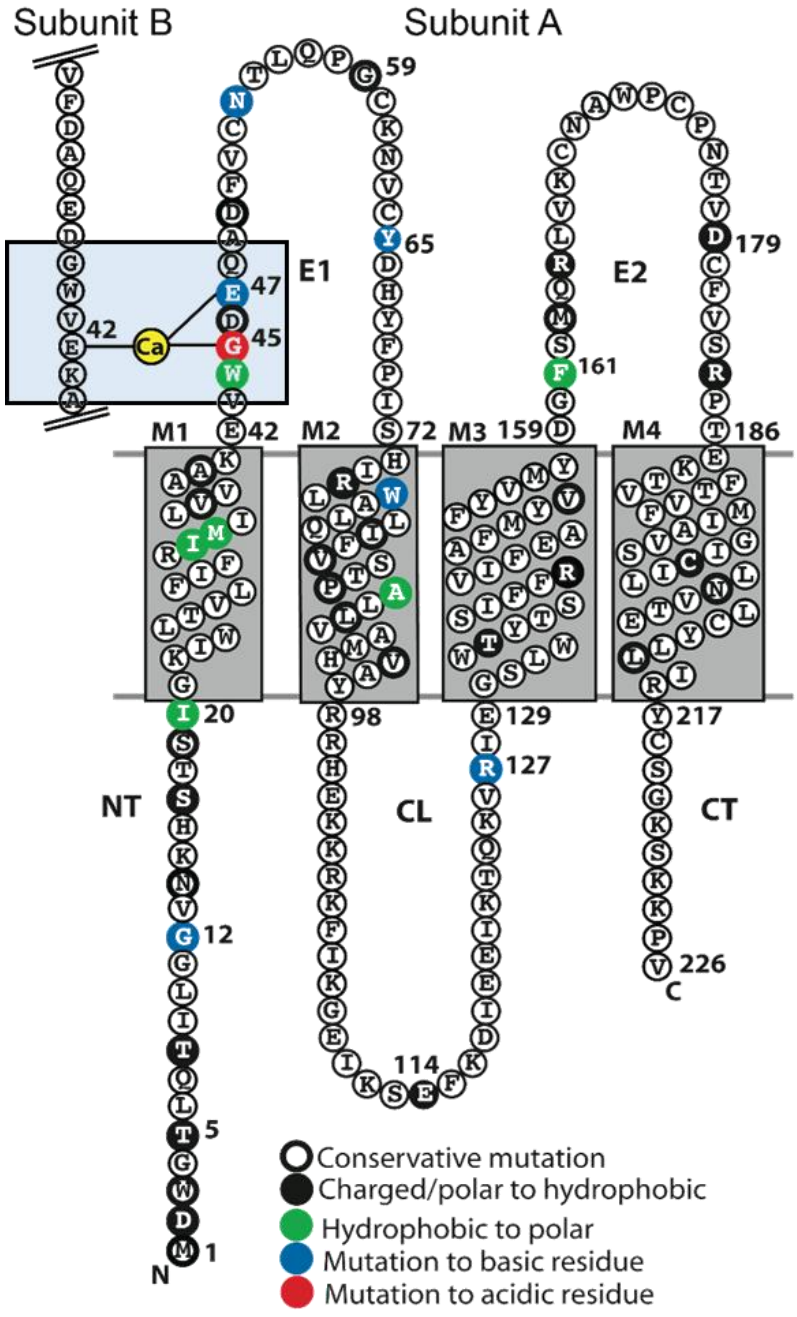

Figure 1.11. Cx26 point mutations involved in sensorineural hearing loss. Over 100 single point mutations in Cx26 leads to syndromic and non-syndromic deafness. Labeled on a topology model of Cx26 are point mutations of connexins that traffic to the membrane and have been tested for function *in vitro*. Boxed in blue is a cluster of mutations that coincides with the site of Ca^{2+} coordination in the X-ray crystal structure (1).

1.2.3. *Skin Disease*

In the basal, spinous, and granular keratinocyte layers of the skin, Cx26, Cx30, Cx30.3, Cx31, and Cx43 are believed to maintain epidermal integrity and homeostasis (**Figure 1.12A**). Not surprisingly, mutations in these isoforms are responsible for eleven different genetic skin diseases that are characterized by skin thickening (**Figure 1.12C**) or break down of the epidermal barrier (**Figure 1.12D**). Often linked with deafness, point mutations in Cx26 are responsible for six of these diseases, and most studies regarding skin disease have focused on this isoform. Most Cx26 skin disease mutations are found in the pore-lining residues or in the extracellular domain (**Figure 1.12B**) inhibiting GJC formation and increasing hemichannel activity. Interestingly, some of these mutations cause formation of active heteromeric channels with Cx43, an α connexin that does not normally associate with β connexins like Cx26 (56, 59). As with the study of deafness mutations, the work presented in **Chapter 2** provides a more efficient method for studying structural changes in Cx26 skin disease mutants. In addition, since many skin disease mutations cause aberrant hemichannel activity, the cryoEM studies of the Cx26 hemichannel presented in **Chapter 3** can provide a method for evaluating structural changes associated with hemichannel disease mutations.

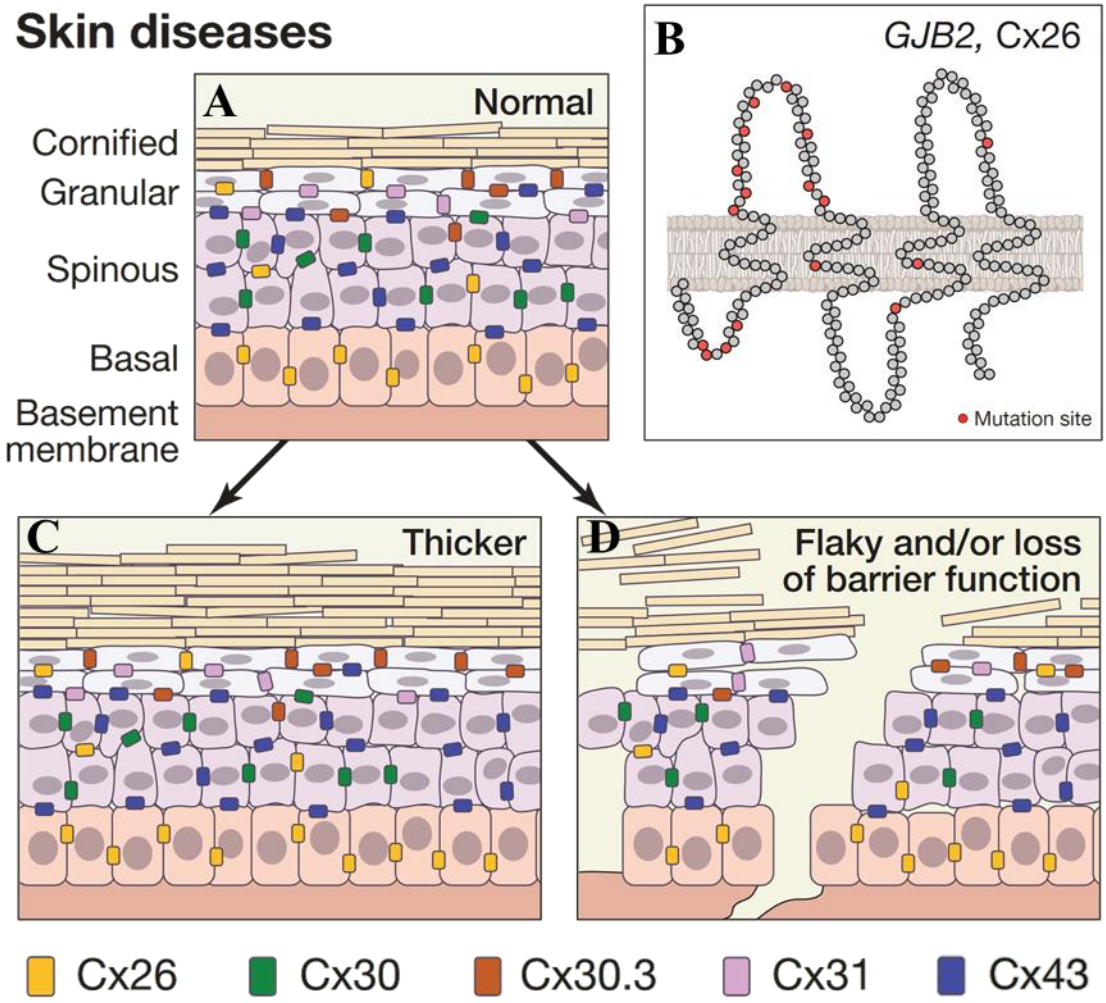

Figure 1.12. Mutations in keratinocyte gap junction channels cause skin disease. (A) Cx26, Cx30, Cx30.3, Cx31, and Cx43 maintain cell cohesion and homeostasis in the granular, spinous, and basal layers of the epidermis. GJC dysfunction results in either skin thickening (C) or flaky coherence between keratinocytes (D). Most skin disease mutations are on Cx26, which are labeled on the topology diagram in (B). Images have been modified from (56).

1.2.4. *Charcot-Marie-Tooth disease*

Charcot-Marie-Tooth disease (CMT) is a group of inherited peripheral neuropathy diseases affecting approximately 1 in 2,500 people worldwide and characterized by degeneration of peripheral nerves (60, 61). Affected patients have progressive muscle weakness, atrophy, sensory loss, and decreased tendon reflexes of muscles in the hand, feet, and legs (60, 62). CMT is classified into two categories depending on whether the defect is in the myelin sheaths (CMT1) or axon (CMT2). Schwann cells express Cx32, which forms GJCs between myelin sheaths layers allowing for cytoplasmic continuity that decreases the diffusion pathway of intracellular components up to 300-fold (60, 63) (**Figure 1.13**). Over 400 Cx32 mutations (**Figure 1.14**) lead to X-linked CMT1, the second most common form of CMT, likely due to partial or complete loss of function in Schwann cells. Effects of these various mutants include decreased expression, defective membrane trafficking, decreased pore diameter, increased sensitivity to acidification-induced closure, stabilization of the closed state, and reduced junctional coupling (63, 64). The structure of Cx32 is unknown and often inferred from Cx26 (1, 18, 65, 66), which shares 50% sequence identity with Cx32. Having an accurate atomic model of Cx32 would provide a starting model for structural studies such as molecular dynamics simulations, electron paramagnetic spectroscopy, X-ray crystallography, and cryoEM to identify structural changes associated with functional CMT mutations. In **Chapter 4**, I will discuss our studies regarding expression, purification, and stabilization of the Cx32 gap junction channel for structure determination via cryoEM.

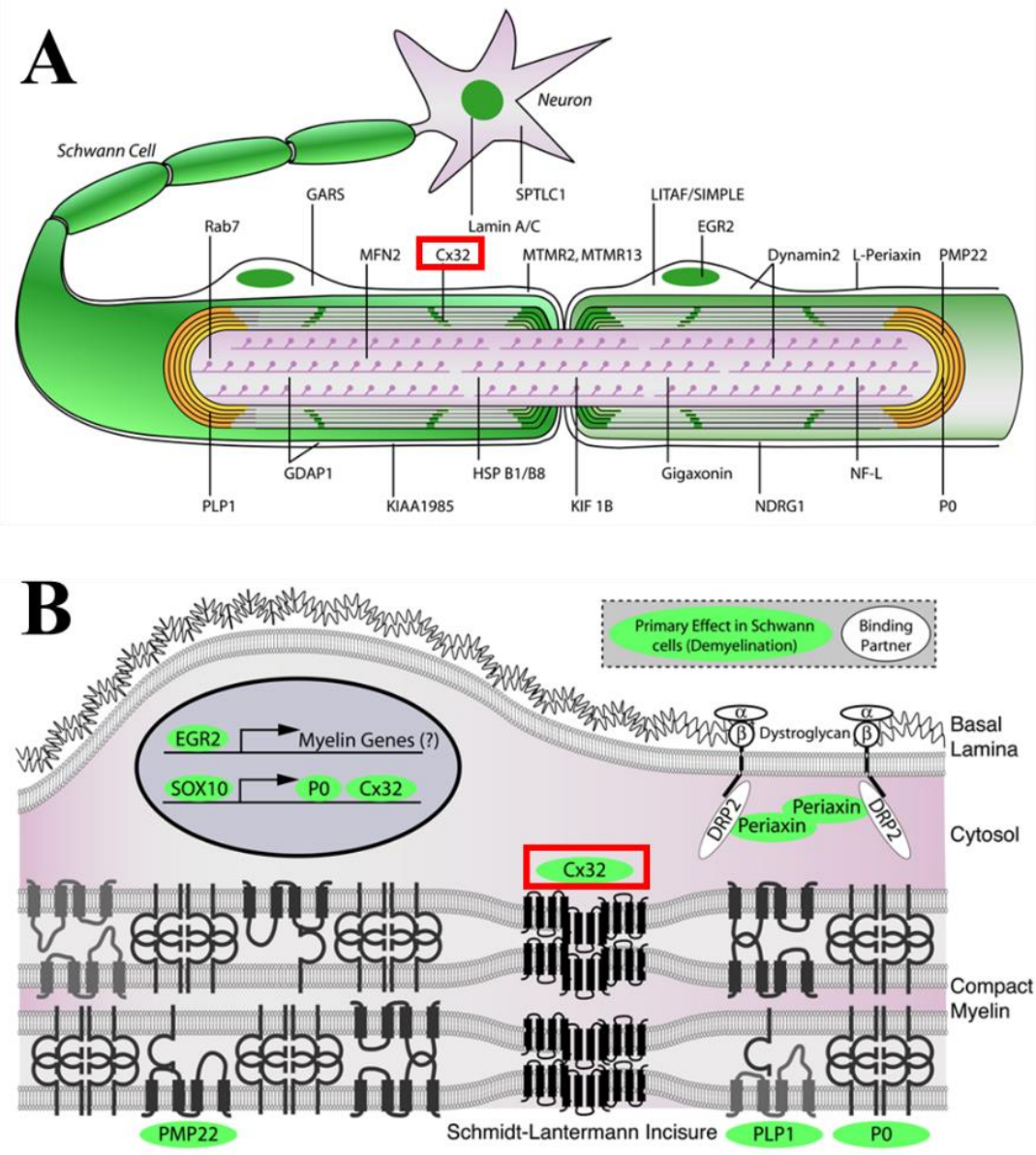

Figure 1.13. Cx32 facilitates cytoplasmic continuity within Schwann cells. Cx32 form GJCs between myelin sheets of Schwann cells in neurons (**A**) allowing for cytoplasmic continuity (**B**). Images adapted from (67).

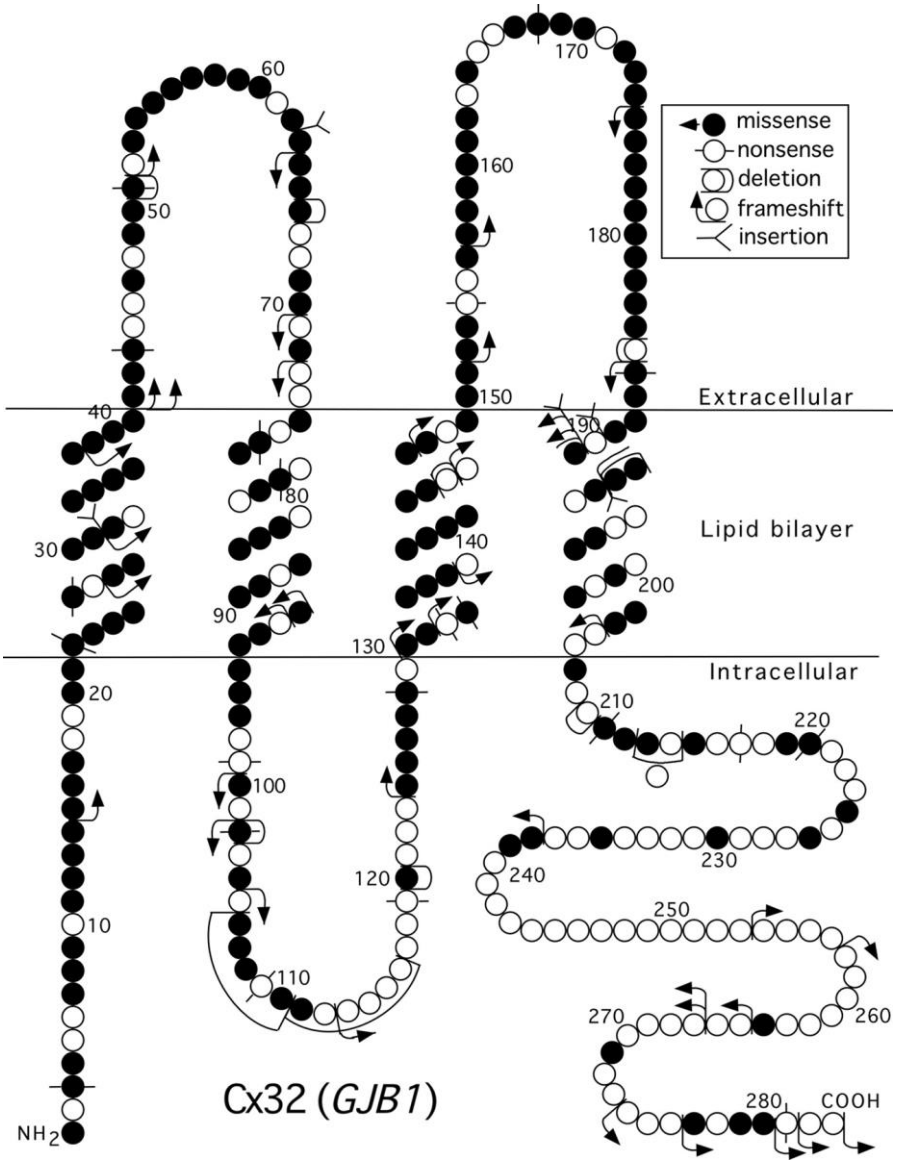

Figure 1.14. Cx32 CMTX1 mutations. Labeled on a topology model of Cx32 are over 400 mutations leading to X-linked CMT. These mutations span all regions of the protein. Image is from (63).

Chapter 2
pH-gating of gap junction channels: visualization of a “ball-and-chain” by cryoEM

Ali K. Khan[1,*], Maciej Jagielnicki[1,*], William E. McIntire[1], Michael D. Purdy[1], Venkat Dharmarajan[5], Patrick R. Griffin[5] and Mark Yeager[1,2,3,4,]

[1] Department of Molecular Physiology and Biological Physics, University of Virginia School of Medicine, Charlottesville, VA 22908 USA. [2] Center for Membrane Biology, University of Virginia School of Medicine, Charlottesville, Virginia 22908, USA. [3] Cardiovascular Research Center, University of Virginia School of Medicine, Charlottesville, Virginia 22908, USA. [4] Department of Medicine, Division of Cardiovascular Medicine, University of Virginia School of Medicine, Charlottesville, Virginia 22908, USA. [5] Department of Molecular Medicine, The Scripps Research Institute, Scripps Florida, Jupiter, FL 33458, USA. [*] These authors contributed equally to this work.

In the context of tissue injury as occurs in myocardial infarction, the cytoplasmic Ca^{2+} concentration increases, and pH decreases. Both conditions lead to inhibition of GJC s (3). In this chapter, we elucidate the structural mechanism of GJC pH gating using cryoEM and mass spectrometry.

2.1. Acidic pH stabilizes a conformation of the Cx26 GJC with a pore occlusion

Using single-particle cryoEM (**Extended Data Table 2.1**) we reconstructed the Cx26 channel reconstituted in amphipol 8-35 at physiological pH level of 7.5 with D6

symmetry applied (**Figure 2.1 a, b**). The channel recapitulated the authentic Cx43 channel from native lipid bilayers (14, 16) and previous Cx26 X-ray structures (**Extended Data Figures 2.8, 2.9**) (1, 18). While the resolution was calculated to 4 Å using the gold-standard Fourier Shell Correlation (FSC), local resolution calculation with Resmap revealed that the map resolution was quite heterogeneous (**Extended Data Figure 2.3g, e, and f**, respectively). Within the transmembrane and extracellular domains, the map resolution was ~3.5 Å, whereas the cytoplasmic loop and cytoplasmic tail were not resolved, likely due to conformational flexibility.

We then proceeded to image the channel in acidic conditions (pH 6.4), which is below what was reported to be required for a pH-induced Cx26 channel closure (30, 68). Using negative stain EM, we discovered a persistent density inside the pore of each hemichannel (**Extended Data Figure 2.2**) in a similar position in the channel as observed in a previous study (23). Three-dimensional classification of cryoEM images recorded from particles at pH 6.4 yielded both open and closed states, in equally populated conformations (**Extended Data Figure 2.5**). The open conformation refined to 4.2 Å resolution (**Extended Data Figure 2.4c, e, and h**), and resembled the physiological pH structure (**Figure 2.1c, d**), but with a less pronounced ring of density in the pore. The closed conformation refined to a resolution of 7.6 Å (**Extended Data Figure 2.4d, f, and h**), but revealed a larger occluding density in the pore of both hemichannels with a connecting density to the M1 helix of each Cx26 protomer (**Figure 2.1e, f**).

Our models display a good fit into their corresponding densities in the regions covering helices M1 through M4 and extracellular loops E1 and E2. These regions are the best resolved in all three maps (**Figure 2.2**). In the case of unoccluded physiological pH

and low pH structures, some bulky side chains were resolved (**Figure 2.2a–d, e–h**), whereas the occluded low pH structure building was limited to an assignment of Cα through the whole model (**Figure 2.2i–l**). The resolution of the maps drops towards the cytoplasmic ends of the gap-junction channel, with the last few residues of M1-M4 helices in that regions largely missing side chain densities, regardless of the overall resolution of the maps. The densities are missing for both CL and CT domains, and the densities for NT domains are incomplete and of lowest resolution in the unoccluded maps.

As noted, we observe a discontinuous ring of density in the unoccluded state of the channel at both physiological (**Figure 2.3a, d**) and acidic pH (**Figure 2.3b, e**) with roughly the same diameter and in the same location as the terminal end of the pore occluding density seen in pH 6.4 closed map. It is unlikely that this occlusion represents an experimental artifact. At a contour level of 4σ, the occlusion and six connecting densities have a volume of ~8.4 x 10^3 $Å^3$, which is too high to represent the amphipol membrane mimetic (9 kDa) or any buffer components. It is also unlikely that this obstruction is an artifact of the applied D6 symmetry. Using the same particle set, we refined the occluded structure using no symmetry and C6, D2, and D3 symmetry. The no-symmetry refinement yielded an uninterpretable map (>10-Å resolution). Refinement with C6 symmetry, in which the two-fold symmetry axis parallel to the membrane is removed, revealed occlusion in both connexons indicating that the pore is blocked on both sides (**Extended Data Figure 2.6a**). Though at lower resolution than the D6 map, the D2- and D3-symmetric reconstructions each revealed six connecting densities to each hemichannel occlusion (**Extended Data Figure 2.6b, c, respectively**), demonstrating that the occluding density is not an artifact of applying 6-fold symmetry and suggesting a model in which all promoters of each

hemichannel contribute to the occluding density. We believe that the ring of density at physiological pH is a result of the NT equilibrating between unoccluding and occluding conformations. This hypothesis is supported by EX1 kinetics observed in the NT during HDX experiments at physiological pH (**Figure 2.4b**) as opposed to pH 6, which displayed no EX1 kinetics.

We ascribe the occluding density to the NT domain. While the resolution of the occluded model (7.6 Å) prohibits unambiguous assignment of amino acid residues, it is sufficient to exclude both the cytoplasmic loop and tail. The cytoplasmic tail with poly-histidine tag in our Cx26 construct is too short to occupy the connecting density and gating particle. In addition, we anticipate that the poly-histidine tag would repulse other C-tails, preventing association to form the occlusion. The cytoplasmic loop is long enough to accommodate the occlusion, but in such a scenario we would anticipate to observe twelve connecting densities, while our model only shows six that are too slim to accommodate more than one polypeptide chain (**Extended Data Figure 2.6d**). Another possibility is that only 3 CLs participate in gating, but the application of D6 symmetry to the map would weaken the signal from the "chain" rather than strengthen them as we observe. The occluding and connecting density in the closed state is thus most likely composed of the amino terminus. The acetylated N-termini can extend and conform to the complete volume of the occluding and connecting densities. Furthermore, the predicted volume corresponding to all six acetylated N-termini (residue 1-14) is ~10.9 x 10^3 $Å^3$, which closely matches the measured volume of the occlusion and six connecting densities (~8.4 x 10^3 $Å^3$) at a contour level of 4σ.

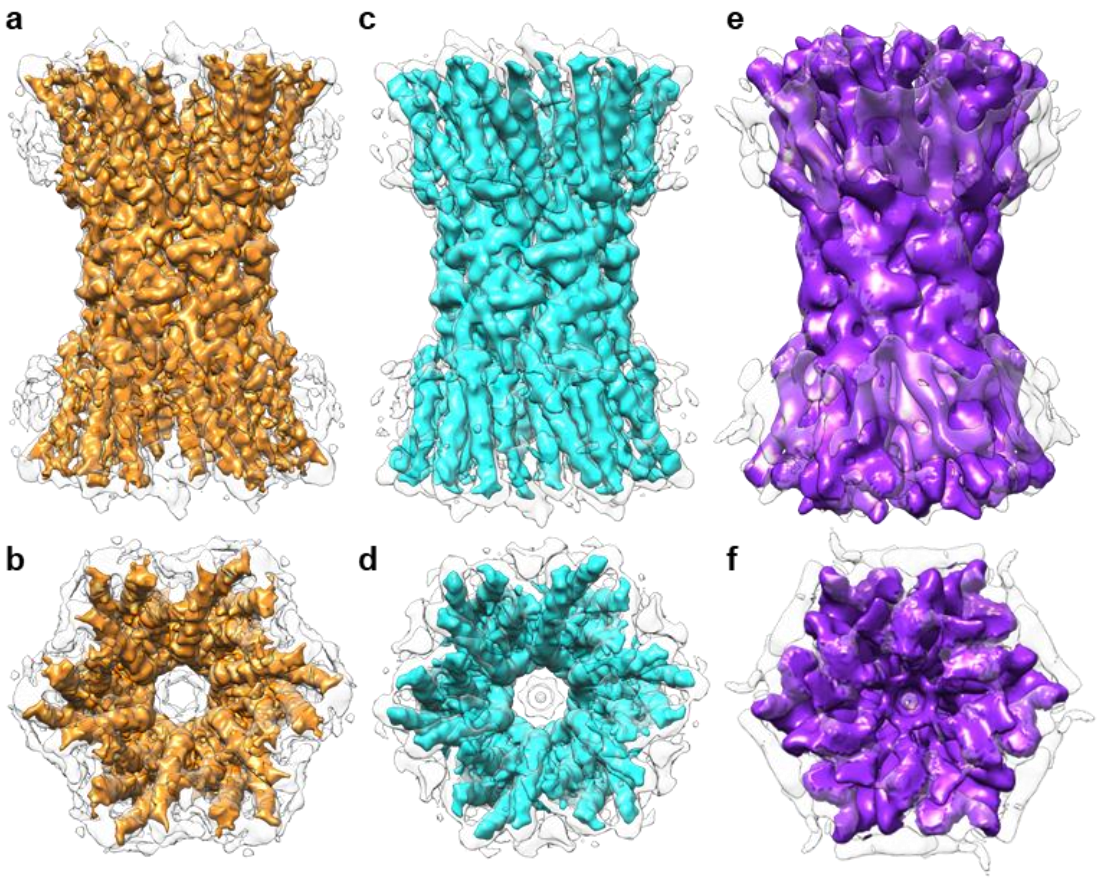

Figure 2.1. CryoEM structures of the human recombinant Cx26 GJC in amphipol A8-35. Side view (parallel to the membrane) and cytoplasmic view of the open physiologic pH (**a** and **b**), open acidic pH (**c** and **d**), and occluded acidic pH (**e** and **f**) Cx26 cryoEM maps. Colored maps (**a** – **d**) represent sharpened densities while colored maps (**e** and **f**) were not subjected to sharpening. Amphipol densities were removed from all colored maps.

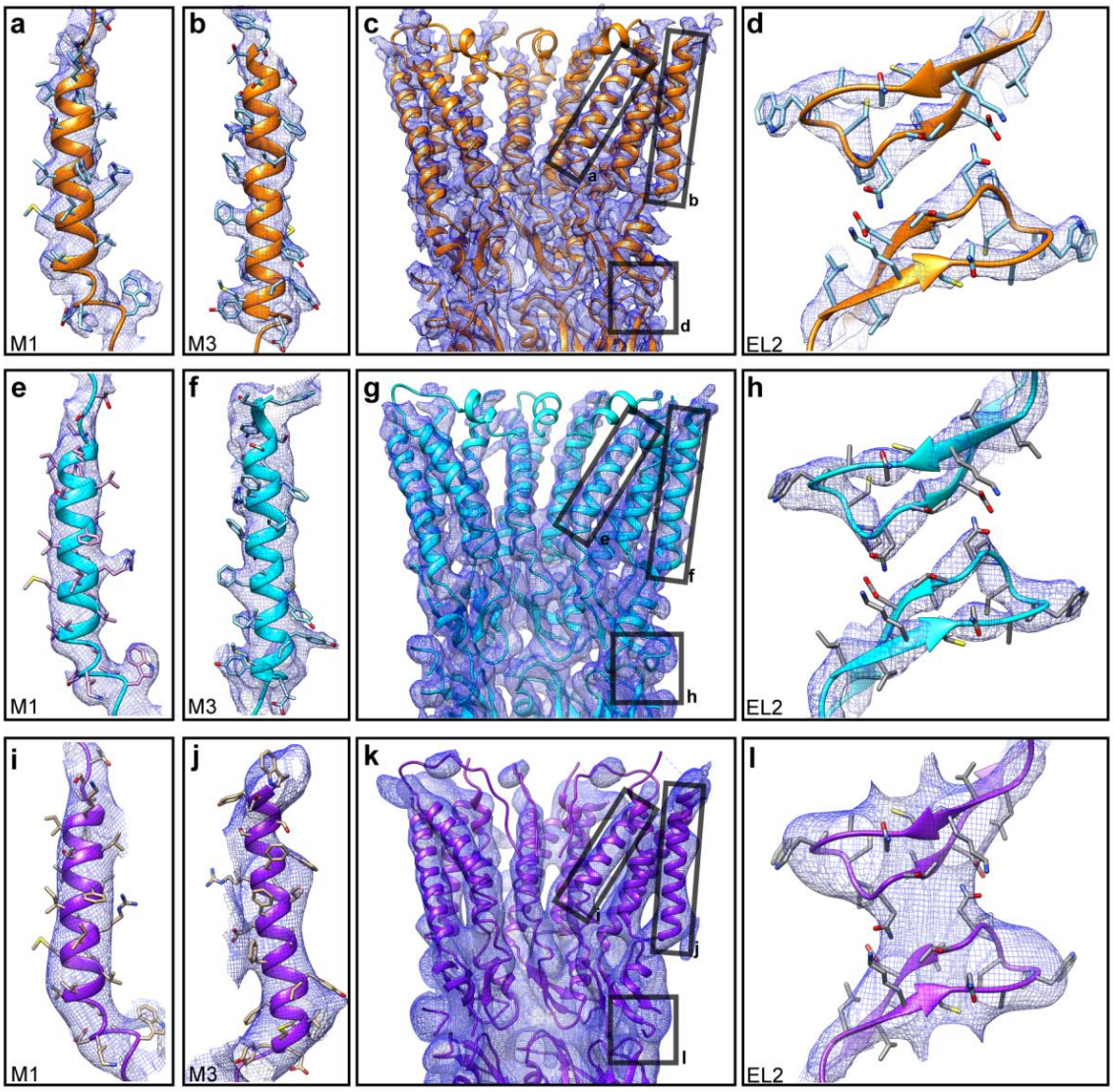

Figure 2.2. Analysis of Cx26 cryoEM maps and atomic models at neutral and acidic pH. (**a**-**d**) Analysis of neutral pH open GJC structure at 4 Å resolution. Cross-sectional view (**c**); a subsection of the extracellular gap region, showing E2 domains from two monomers from two opposed hemichannels (**d**); a close-up of M1 helix (**a**) and M3 helix (**b**). (**e**-**h**) An analogous analysis of low pH open GJC structure at 4.2 Å resolution and (**i**-**l**) low pH closed GJC structure at 7.6 Å resolution. Contour levels adjusted individually on a per-image basis. Masking and sharpening procedures were applied to neutral pH and low pH open maps. *Atomic modelling by Maciej Jagielnicki and Michael Purdy.*

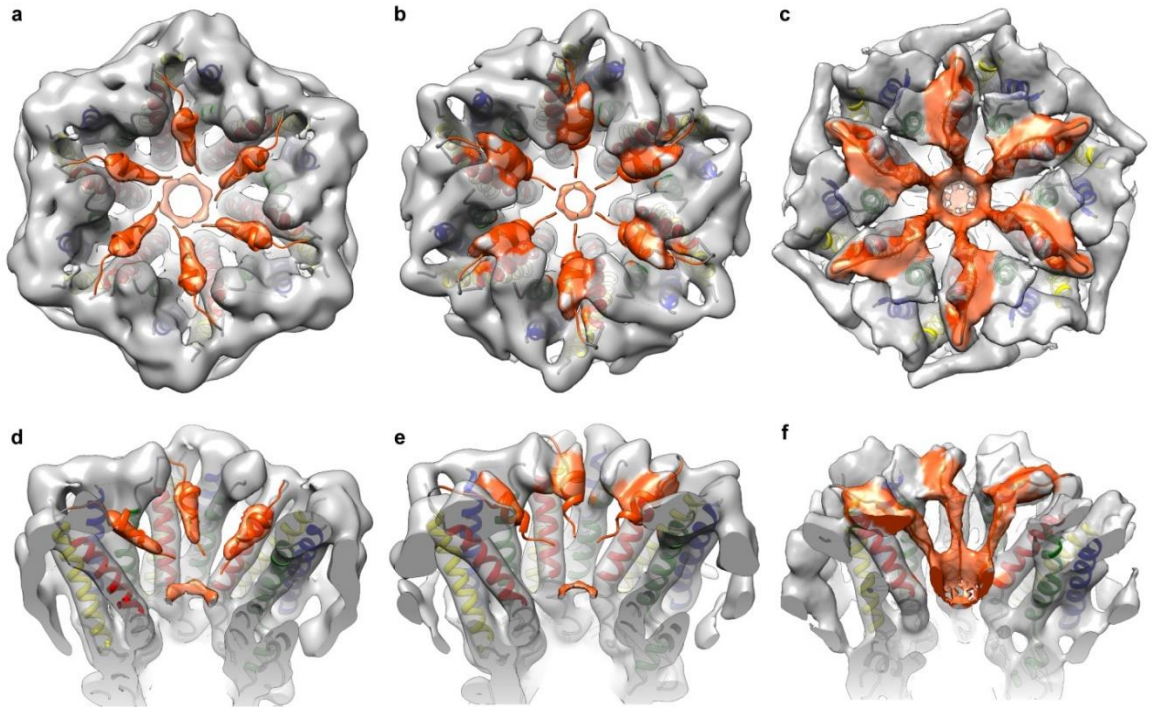

Figure 2.3. Analysis of cryoEM maps and models showing pH-gating in Cx26 mediated by NT domains. End-on views of Cx26 hemichannel from the cytoplasmic side extending to the end of transmembrane helices at the extracellular gap; pH 7.5 structure (**a**), pH 6.4 structure (**b**) and pH 6.4 'plug' structure (**c**). Tilted cross-sectional views of Cx26 hemichannel showing the organization of three monomers; pH 7.5 structure (**d**), pH 6.4 structure (**e**) and pH 6.4 'plug' structure (**f**). M1 helix (red), M2 helix (green), M3 helix (blue), M4 helix (yellow), NT domain 1-15 aa (orange), cryoEM densities (transparent light grey) and NT densities (transparent orange). Helices M1 and M4 of the central monomer in panel (**f**) were not colored (white). All the maps shown are at a resolution of 7.6 Å and displayed at 4.1 sigma (σ) contour level. No masking or sharpening procedures were applied.

2.2. Hydrogen deuterium exchange reveals dynamic N-terminus at physiological pH

Hydrogen deuterium exchange (HDX) coupled with mass spectrometry was used to evaluate solvent accessibility. Several regions of Cx26 exhibited decreased deuterium exchange at lower pH: the M1/E1 (residues 37-50), the M3/CL region (residues 121-132) and the NT domain (residues 7-28) (**Figure 2.4a**). Kinetics of HDX, in particular EX1 kinetics, also revealed the dynamic nature of the NT domain. EX1 kinetics, which are indicative of transient conformational transitions, were observed at the NT at physiological pH, but not at acidic pH (**Figure 2.4b**) suggesting that the NT may exist at more static lower energy states at acidic pH. These results indicate that the NT takes multiple conformations at physiological pH, but at acidic pH, the interconversion between states has become slower than the timescale of the HDX experiment. Taken in conjunction with the cryoEM results, we believe at physiological pH the NT is freely able to adopt multiple conformations, including the putative NT helix (18, 69) that may form transiently. At acidic pH, the equilibrium shifts towards NT extension and association to form the occluding pore density.

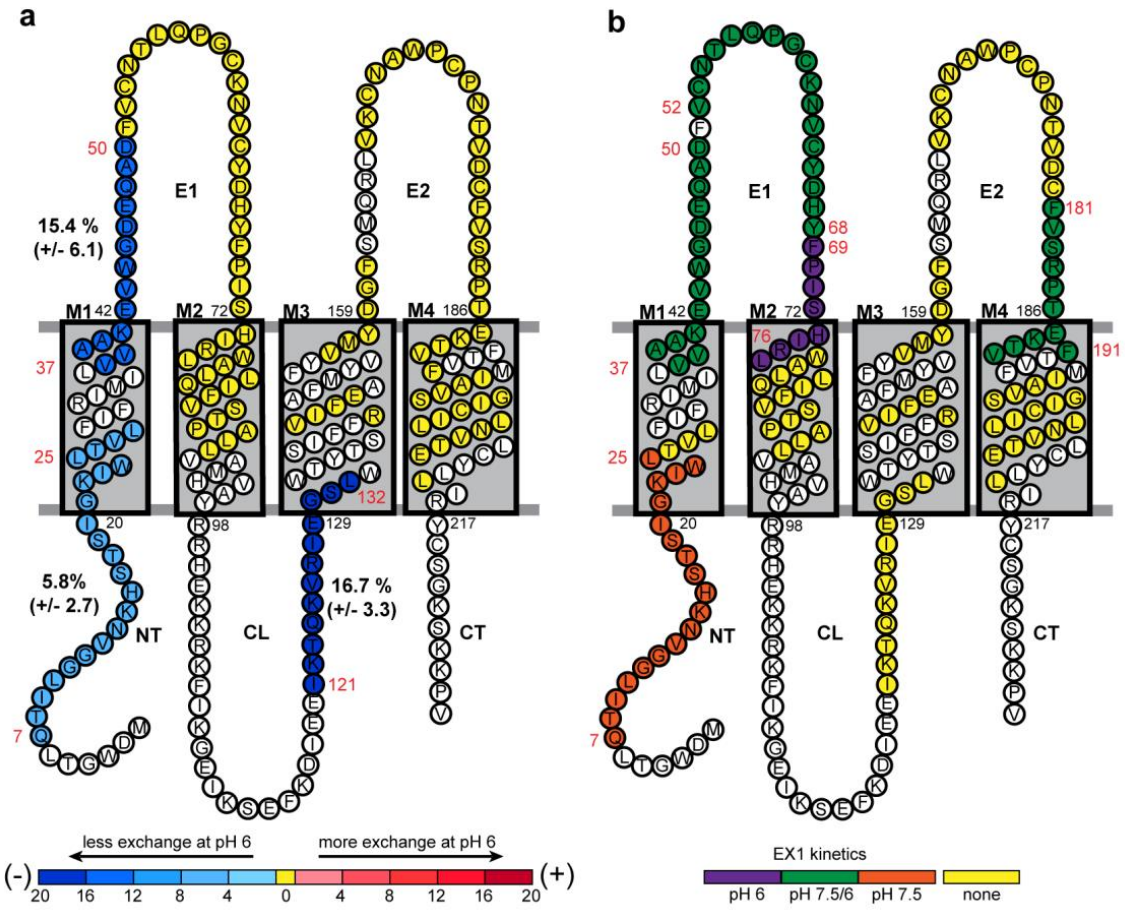

Figure 2.4. Comparison of the dynamics of Cx26 GJC between pH 7.5 and 6.0 using HDX mass spectrometry. (**a**) Change in deuterium uptake at pH 6.0 compared to pH 7.5 The topology model shows the localization of three regions with reduced deuterium uptake at pH 6.0. The numbers next to each of these peptides show % deuterium uptake change, along with their associated SD. (**b**) A topology model illustrating detected EX1 kinetics of deuterium exchange, which arise from transient, large-scale unfolding events, interpreted as multiple conformational states of a given peptide. *Experiments by Maciej Jagielnicki, William McIntire, Venkat Dharmarajan, and Patrick R. Griffin*.

2.3. Acidic pH induces movement of M2 helix

We observe no additional pore constriction due to the positioning of M1-M4 helices in our low pH closed structure, which argues against the 'camera-iris'-type of mechanism for low pH gating (12). Upon acidification, the M2 helix does, however, translocate towards the M1 helix within the same subunit. In the occluded structure, the movement of the A92 Cα atom on M2 helix by ~5 Å toward the Cα atom of K22 on M1 (**Figure 2.5**). This movement of the helix is also reflected in the unoccluded cryoEM maps, where the density of the cytoplasmic end of M2 is weakest of all 4 TM domains, indicating that this portion is likely more flexible than the others. This translocation ultimately positions the M2 residue to interact with M1 within protomer, as well as, NT in the adjacent Cx26 subunit. This movement is further complemented with a prominent low-resolution density in the occluded cryoEM map connecting the M2 helix with the NT (**Figure 2.3c, f**) of the adjacent protomer, indicating cooperativity between Cx26 subunits within the same hemichannel.

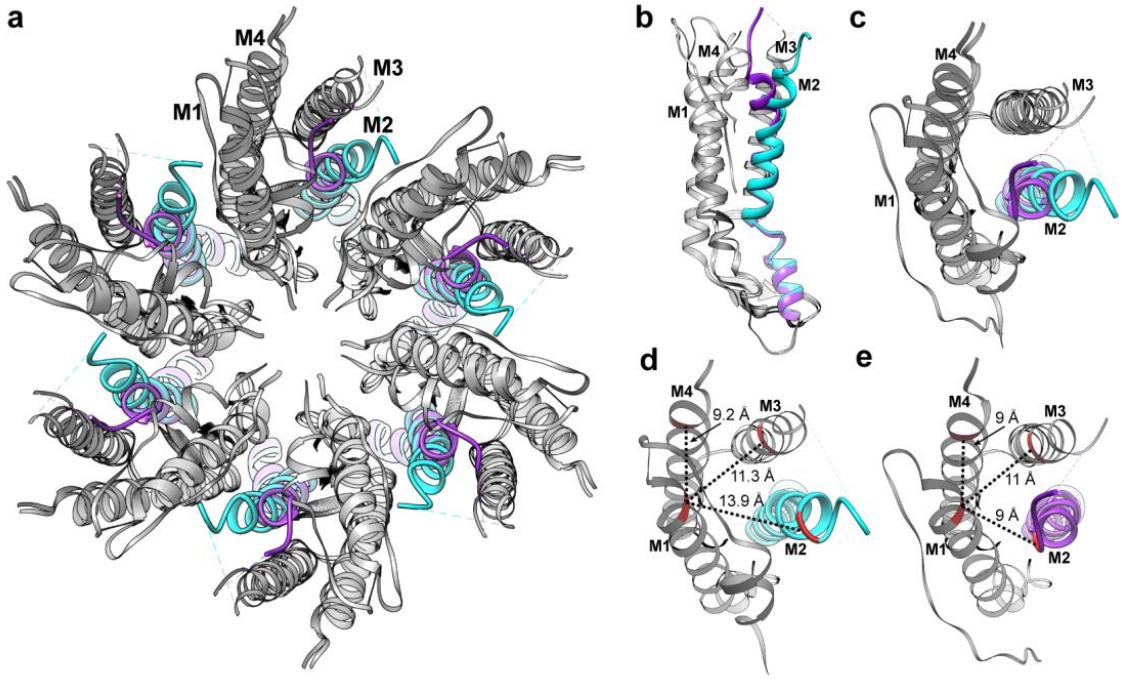

Figure 2.5. Visualization of M2 helix movement during pH-induced gating. (**a**) A top view of a Cx26 GJCs from pH 6.4 open and closed structures. (**b**) A side view of superposed Cx26 monomers from pH 6.4 open and closed structures. (**c**) An end-on view of superposed Cx26 monomers from pH 6.4 open and closed structures. (**d**) An end-on view of a Cx26 monomer from the cytoplasmic side showing distances between Cα atoms of Lys22 (M1) and Ala92 (M2), Ile140 (M3) and Glu209 (M4) in the pH 6.4 open structure. (**e**) The same view of a Cx26 monomer but shown for the pH 6.4 closed structure. Ribbon coloring: pH 6.4 open structure (cyan), pH 6.4 closed structure (violet).

2.4. Increased NT-CL association at acidic pH

The CL and CT domains were not visualized in our cryoEM experiments at either pH. In order to elucidate the conformational relationships between cytoplasmic domains, we generated lysine crosslinks of Cx26 using the bis(sulfosuccinimidyl)suberate (BS3) amine-to-amine crosslinker, with a flexible spacer arm 11.4 Å in length (**Extended Data Figure 2.11**) and characterized each crosslink using tandem mass spectrometry (**Extended Data Table 2.5)** (70-73). This approach takes advantage of the abundant lysine residues in the NT, CL and CT (2, 8, and 3 residues, respectively), but has the disadvantage of not being able to distinguish between intermolecular versus intramolecular crosslinks.

The most populated group crosslinks were between the CT (217-235 aa) and CL (98-129 aa) domains with K221, K223 and K224 crosslinked with every lysine in the CL (**Figure 2.6e**). While the CT is too short to form the gating particle, CT-CL interactions have been previously reported to be pH-dependent (30). The observed pH-dependent changes concern only K224, which forms unique crosslinks with K102 and K105 at pH 7.5 and with K112 at pH 6. The remainder of the K224 crosslinks were detected in both pH conditions. Given the proximity of K223 and K221 to K224 and their unchanged crosslinking pattern, the subtle changes in K224 crosslinking do not allow for a clear interpretation of the pH effect on CL-CT interaction.

The second most numerous group of crosslinks consists of those located within the CL domain (98-129 aa), which is not surprising given the proximity of M2 and M3 helices in Cx26 structure restricting the spread of CL lysines (**Figure 2.6d**). Almost every lysine in this lysine-rich domain (8 residues out of 15 in total in Cx26) was crosslinked with every other lysine in that region. No difference was detected between samples from pH 7.5 and

pH 6 though. There is no evidence that the CL domain participates in pH-gating in Cx26. It was, however, shown to be dynamic (36), which could help explain the abundance of crosslinks in CL. This notion was further fortified by the lack of CL densities in existing structural X-ray and cryoEM data.

The largest changes in crosslinking between the two pH values occur in the NT-CL and M1-CL crosslinks. Under acidic conditions, K22 in the M1 helix uniquely crosslinked with K102 and K105, and K15 in the NT crosslinks with K105, K108, and K112. The only unique crosslink in physiological pH was K15 to K103. Previous studies have shown that pH-mediated block on Cx26 requires an electrostatic interaction between residues N14 and H100, which can be abolished by substituting a positively charged amino acid in position 14 and rescued by mutating residue 100 to one without charge (49). Our observations from cryoEM and crosslinking experiments are consistent with this previous work because we see crosslinking of nearby residues and a shift of M2 towards NT of the adjacent protomer. which would bring these residues closer together in the occluded structure (**Figure 2.5a**).

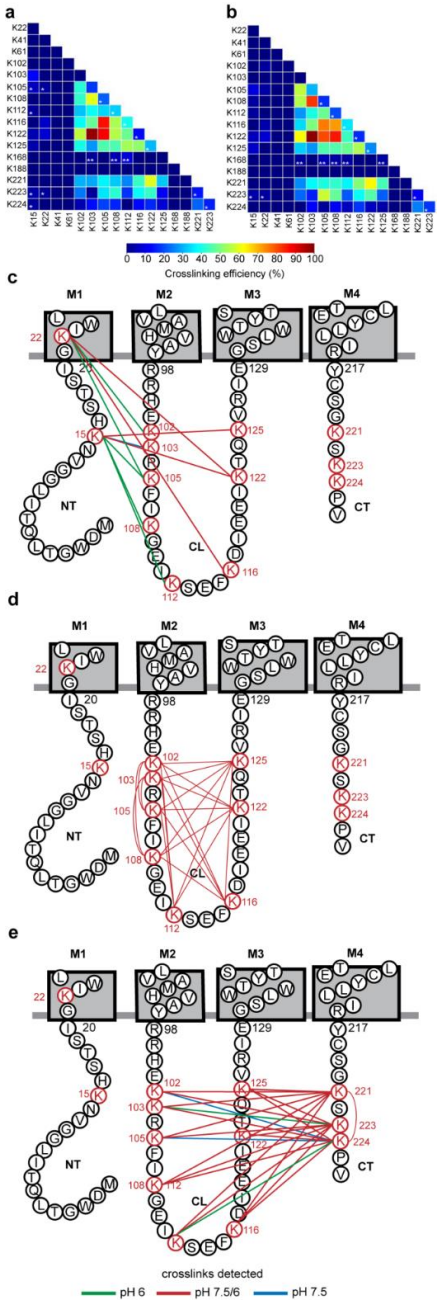

Figure 2.6. Mapping of lysine-lysine crosslinks. The heat maps showing crosslinks detected at pH 7.5 (**a**) and pH 6.0 (**b**). The square color represents crosslinking efficiency (color code on the bottom). Squares denoted with (*) are low-confidence crosslinks, not included in the analysis. Squares denoted with (**) are low-scored crosslinks with lysine 168 and are not analyzed. (**c**) Crosslinks between NT and CL domains. (**d**) Crosslinks within CL domain. (**e**) Crosslinks between CL and CT domains. *Experiments by Maciej Jagielnicki, William McIntire, Venkat Dharmarajan, and Patrick R. Griffin*.

2.5. Concluding Remarks

GJCs are believed follow a "ball-and-chain" mechanism of closure similar to that of the voltage-gating of sodium and potassium channels (74, 75). This hypothesis was first established in studies of Cx43 where acidification-induced uncoupling was abolished with a C-terminal truncation at residue 257 (76) and could be restored if the truncated CT portion was co-expressed as a separate peptide (77). While most connexins show pH gating in this manner, truncation of the CT does not affect pH gating of Cx26 (46). Evidence of the particle receptor model of pH closure in Cx26 first came from 2D crystallographic studies, where a low-resolution model of Cx26 M34A at pH 5.8 with several other GJC inhibitors (calcium, magnesium, carbenoxolone, and aminosulfonates) displayed an occluding density in the channel pore (23). The identity of the occluding particle was unclear from these studies since the resolution was too low for unambiguous assignment and since there was no visible density connecting the occlusion to the rest of the channel. Follow-on studies with an NT deletion (residue 2 - 7) revealed a less prominent occluding density (24), supporting the notion of the NT domain playing the role of a physical plug. Mutations in the NT domain have also been shown to either remove or diminish the effect of low pH on Cx26 hemichannels (49).

Our observations support the hypothesis that pH-mediated gating of Cx26 is achieved by a "ball-and-chain" mechanism (**Figure 2.7**). We conclude that acidic pH shifts the equilibrium of a highly flexible NT towards an extended state, which then associates with other NTs to form the gating particle or "ball". This association is accompanied by translocation of M2 towards M1, and increased proximity of CL with NT. Formation of

the “ball” appears to be required for inhibition. The pore diameter with the connecting densities or “chains” alone is measured to be roughly ~16 Å in the pH 6.4 closed structure, which would allow passage of a potassium ion with at least 2 shells of hydration (12 Å in diameter). The movement of the M2 helix may be correlated to an interaction between residues N14 and H100, which previous studies have shown to be essential for pH regulation (49), but the resolution of the closed structure and incomplete visualization of the cytoplasmic domains precludes analysis of these amino acids. Future structures with N-terminal deletion mutants would certainly help validate the identity of the gating particle, but attempts to delete N-terminal residues, thus far, have resulted in constructs with severe expression defects.

Our occluded cryoEM structure clearly shows block in both hemichannel pores, and we were not able to individually classify any 3D classes with ball-and-chains formation on only a single hemichannel. However, it should be noted that the protein preparations for both cryoEM and mass spectrometry studies lack any chemical gradient across the junction. In the presence of a pH gradient, it is plausible that the channel can be gated on only one side. Our structure also shows the “ball” made up of six “chains” forming in a cooperative manner. Image processing did not reveal any intermediate occluding conformations formed by fewer than six “chains,” and lower-resolution density in the occluded cryoEM map reveals that residues in the M2/CL boundary interact with the NT in the adjacent Cx26 subunit. Previous studies on closely related concatemer pannexin channel have revealed that C-terminal gating does not require participation from all protomers (78). It is easy to envision a similar phenomenon in Cx26, where the “ball” can be formed by fewer NTs, which would still successfully halt or greatly dampen conductance. Indeed, traces of

asymmetry in the "ball" closing the channel in pH-gating can be found in electron crystallographic studies of Cx26 M34A mutant (24).

To our knowledge, this is the first instance in which a complete, oligomeric "ball-and-chain" has been visualized. While not exactly like fast inactivation of sodium and potassium channels, we observe several properties consistent with these "ball-and-chain" mechanisms. First, in shaker K^+ channels, the ball-and-chain are formed by the terminal end of the N-terminus. On the basis of the X-ray crystal structures of KcsA K^+ channel in the presence of tetrabutylammonium (TBA) and tetrabutylantimony (TBSb), Zhou *et al.* proposed that gating requires extending of the N-terminus so that it can enter and block the pore (79). Our structure is consistent with this finding because the N-terminus appears to be fully extended all the way to the acylated cap of NT to fit the ball-and-chain density. Second, sodium and potassium channels only receive the "ball-and-chain" in the open state. The occluding particle of Cx26 also blocks an open pore conformation, which could easily accommodate hydrated potassium ions. This characteristic makes the "ball-and-chain" mechanism complementary to the electrostatic block induced by Ca^{2+} binding, which maintains an open channel structure (1) (**Figure 2.8**). Indeed, in the context of tissue injury arising from pathological conditions such as myocardial infarction, the cell is simultaneously in a state of calcium overload and decreased intracellular pH (80, 81). While calcium block is limited to positively charged ions and metabolites, pH occlusion would additionally inhibit the passage of neutral and negatively charges species. The electropositive surface induced by Ca^{2+} binding may also explain why the GJC "ball-and-chain" is formed by acylated NT rather than a positively charged amino-terminus because the latter would likely be repelled in the case of simultaneous Ca^{2+} inhibition. Lastly, ball-

and-chains are believed to be inherently disordered structures, which has precluded their complete visualization thus far. At physiological pH, both HDX EX1 kinetic measurement and cryoEM reveal inherent conformational heterogeneity in the gating particle (NT), and our occluded structure is significantly lower resolution than the open state, though the imaging conditions are identical to the ungated acidic pH map. This moderate resolution may be a result of the heterogeneity that arises from this relatively disordered state. Fortunately, the ability of single-particle cryoEM to resolve heterogenous particle states and refine moderate resolution structures has given us the ability to visualize the pH induced “ball-and chain.”

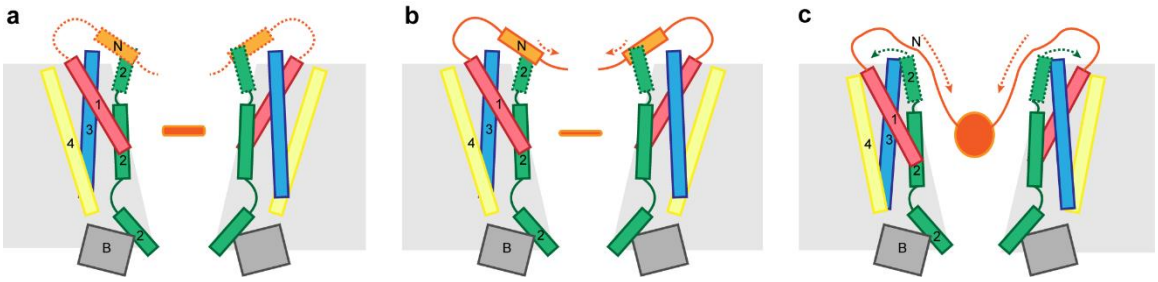

Figure 2.7. Low pH – induced gating model. At neutral pH (**a**), the GJC is open, and the NT are in a conformational heterogenous state. Upon acidification of the channel (**b, c**), the NT will extend (**b**) and form the occluding gating particle (**c**). M1 helix (red), M2 helix (green), M3 helix (blue), M4 helix (yellow), NT domain 1-15 aa (orange), β-sheet EL1 and EL2 domains (dark grey).

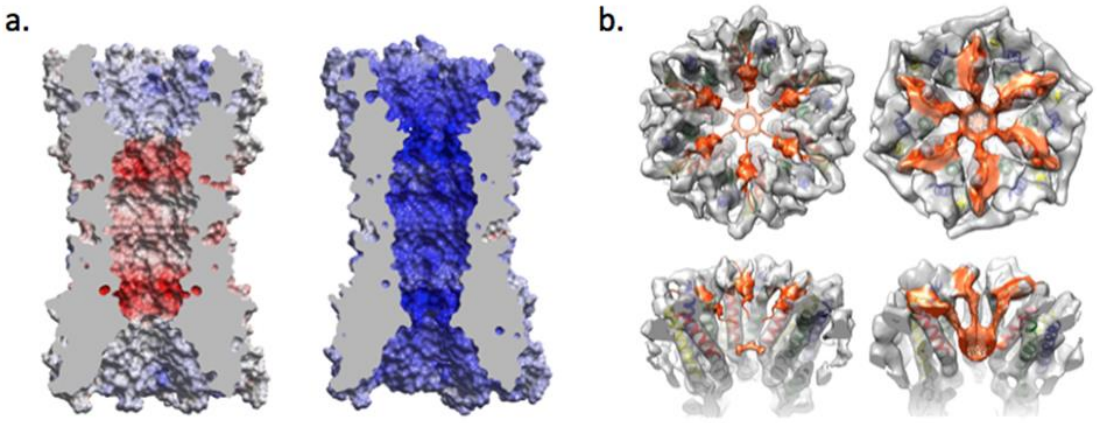

Figure 2.8. Gap junction channel block in tissue injury. Calcium overload (**a**) makes the channel pore electropositive resulting in an electrostatic block of positively charges species. Simultaneously, acidic pH (**b**) results in steric block of the channel pore via a "ball-and-chain" mechanism.

2.6. Methods

Protein expression and purification.

Protein expression and purification were performed as described in (1). For MS/MS and HDX experiments, Cx26 was exchanged into buffer containing 50 mM HEPES pH 7.5, 500 mM NaCl, 0.025 % n-dodecyl-β-D-maltopyranoside (DDM; Anatrace). Samples for EM experiments and the thermal stability assay were exchanged into a buffer containing 50 mM HEPES pH 7.5, 1 M NaCl, 2.5 % glycerol (v/v), 0.025% DDM. The final eluate from the desalting column was concentrated to 4 – 5.5 mg/ml (150 – 210 uM) using a 0.5 ml or 4 ml concentrator (100 kDa MWCO; Millipore).

In order to increase protein stability (**Extended Data Figure 2.1**) and particle contrast (**Extended Data Figures 2.3a and 2.4a**) for cryoEM, detergent was exchanged to amphipathic surfactant Amphipol A8-35. Protein sample at 5 mg/ml was mixed with amphipol (10 mg/ml stock in 50 mM HEPES pH 7.5, 1 M NaCl, 2.5 % glycerol (v/v), 0.025% DDM buffer) at a ratio of 1:3 (w/w), diluting protein to ~2 mg/ml. The sample was incubated for 4 h at 4 ^{o}C with gentle mixing. Detergent was removed by addition of Bio-Beads SM-2 (BioRad) to 30mg/ml and overnight incubation at 4 ^{o}C with gentle mixing. Bio-beads were removed by flowing solution through a fritted 0.5 ml disposable column. Insoluble components were removed by centrifugation of the sample solution for 10 min (16,000 x g) at 4 ^{o}C, and protein was further purified on a Superdex 200 10/300 column, eluting in buffer composed of 50 mM HEPES pH 7.5, 1 M NaCl. The peak corresponding to dodecameric Cx26 channels was collected and concentrated to 2 mg/ml in 4 ml concentrator (100 kDa MWCO; Millipore).

Negative stain EM analysis.

For EM of negatively stained samples, a 3.0 µl drop of protein sample at 0.01 mg/ml was incubated on a glow-discharged, carbon-coated copper grid for 60 s. The grid was washed with three drops of deionized water followed by staining with a drop of 2% uranyl acetate pH 4.5 for 60 s. Between sample application, washing, and staining steps, the grid were blotted with filter paper to remove excess solution. EM data acquisition was performed using a Tecnai G2 F20 electron microscope (FEI, Hillsboro, OR) equipped with a field-emission electron source, operating at 120 keV. Low electron dose images (~15 $e^-/Å^2$) were recorded on a 4K x 4K pixel CCD camera (Gatan, Pleasanton, CA) at 62,000 x magnification (1.8 Å pixel size) with a 1 sec exposure time at a defocus value of approximately -1.5 µm. Image processing was performed using EMAN v2.05 software(82). To facilitate particle visualization, micrographs were subjected to high- and low-pass Gaussian filtering at 100 and 10 Å, respectively. A total of ~3,400 particles were picked manually and extracted with a box size of 230 $Å^2$. Corrections to the contrast transfer function (CTF) were performed using e2ctf.py program. All picked particles were then screened visually, and nonsensical particles were removed interactively, leaving ~3,100 particles. Particles were sorted into 23 class averages using reference-free two-dimensional (2D) class averaging, and particles belonging to minimally occupied or outlier classes were removed, resulting in a dataset of ~3,000 particles. A set of 12 initial three-dimensional maps was derived using e2initialmodel.py over 10 iterations with D6 symmetry imposed. The best map, as judged by the presence of continuous density and measured volume corresponding to a Cx26 GJC, was subsequently refined with D6 symmetry.

CryoEM Sample Preparation.

Purified Cx26 (~2 mg/mL in 50 mM HEPES pH 7.5, 1 M NaCl, amphipol (A8-35)) was diluted to 0.4 mg/mL with a final buffer composition of 50 mM HEPES pH 7.5, 200 mM NaCl. 3.5 µL of sample was then immediately applied to a C-flat holey carbon grid (copper, 2 µM/2 µM hole size/hole space) glow-discharged in an atmosphere of amylamine, manually blotted with Whatman no. 1 filter paper for 3-5 s, and plunge-frozen in liquid ethane cooled by liquid nitrogen. For the low pH sample, purified Cx26 (2.5 mg/mL) was diluted 1:3 (v/v) with a 50 mM MES pH 6 solution to make a 0.63 mg/mL Cx26 protein solution in a 12.5 mM HEPES, 37.5 mM MES pH 6.4, 125 mM NaCl buffer. After a brief incubation (2 – 5 minutes) on ice, 3 uL of sample was applied to a glow-discharged C-flat holey carbon grid, blotted with Whatman no. 1 filterpaper using a Vitrobot (FEI company) (4 s blotting time, blot force of 3, and 100% humidity at 22 ^{o}C), and plunge-frozen in liquid ethane cooled by liquid nitrogen.

CryoEM Data Acquisition.

Data sets were collected at the Electron Bio-Imaging Centre (eBIC) at the Diamond Light Source (Didcot, United Kingdom) on a Titan Krios cryo-electron microscope, operated at 300 kV, equipped with GIF Quantum Energy Filter operated in zero-energy-loss mode with a slit-width of 20 eV and a K2 Summit direct electron detector (Gatan, Inc.). Images were collected using the automated procedure in EPU (FEI) at a 130,000 X nominal magnification corresponding to a 1.06 Å physical pixel size. Images for pH 7.5 sample were recorded in counting mode as a 20-frame movie with an exposure time of 8 s and dose rate of 5.625 $e^{-}/Å^{2}/s$ (total dose 45 $e^{-}/Å^{2}$). Low pH images were recorded in super

resolution mode (0.53 Å super resolution pixel size) as a 25-frame movie with an exposure time and dose rate of 10 s and 4.5 $e^-/Å^2/s$ (total dose 45 $e^-/Å^2$), respectively.

CryoEM Data Processing.

For physiological pH, all movie frames were motion-corrected and integrated using MOTIONCORR (83) while applying a B-factor of 150 $pixel^2$ and frame offset of 5. On the first 94 images collected from the microscope, the contrast transfer function (CTF) was estimated on each integrated image using CTFFIND4 (84). In RELION (85-87), 2D class averages calculated from 745 manually picked particles were used as an input for template-based auto picking. 2D class averages of the auto-picked particles were calculated and used to generate a *de novo* D6 symmetric initial model in EMAN2 (82). On the full dataset, the CTF of each integrated micrograph was estimated using Gctf (88). 2D class averages generated from the previous auto-picked particles were used as templates for automated picking on the full dataset using Kai Zhang's Gautomatch software. By using the resolution limit value output by Gctf, all micrographs lower than 3.3 Å resolution were discarded, and the remainder of the processing was performed in RELION v2. 2D class averages were calculated, and particles from class averages containing helical features (**Extended Data Figure 2.3b**) were subjected to 3D classification (with D6 symmetry) using the EMAN2-generated initial model. All initial models used in 3D class averaging and refinement mentioned herein were lowpass filtered to 50 Å resolution. Approximately 60% of the particles were assigned to a 3D class containing apparent secondary structure and were used for subsequent 3D auto-refinement (with D6 symmetry), that resulted in a gold-standard FSC resolution of 4.5 Å. Beam-induced motion correction and radiation-damage

weighting implemented in the RELION particle polishing procedure were used to improve the signal-to-noise ratio of individual particles (89). Refinement with the "polished" particles improved the resolution to 4.4 Å (**Extended Data Figure 2.3c, d, and g**). In the RELION post-processing procedure, applying a soft mask that excluded the low-resolution signal from the amphipol and cytoplasmic domains and performing automated B-factor sharpening (90) improved the resolution to 4.0 Å (**Extended Data Figure 2.3e-g**).

For acidic pH, all super-resolution movie frames were motion-corrected and integrated using MOTIONCORR while applying a B-factor of 150 pixel^2 and frame offset of 6. CTF estimation was performed with Gctf, and summed micrographs with a resolution limit worse than 3.75 Å were discarded. To generate an initial model, in RELION, 2D class averages generated from 1008 manually picked particles were used as templates for auto-picking on all micrographs. α-helical containing 2D class averages calculated from 2x down-scaled particles from 234 micrographs were used to sort particles from all the micrographs based on the difference between the particle and its aligned reference. The top ~50% of particles were subjected to two consecutive rounds of 2D classification, selecting particles in 2D class averages displaying α-helices after each round. In EMAN2, 2D class averages of the remaining particles were then calculated and used to generate a *de novo* D6-symmetric initial model. Particles were then subjected to two rounds of 3D class averaging with C1 symmetry and one round of 3D class averaging with D6 symmetry to remove bad particles and further improve the initial model. Between each round of 3D class averaging, particles and density from a secondary structure containing 3D class was chosen as inputs for the next round. After generation of the initial model generation, we performed image processing on summed micrographs with a resolution limit higher than

3.75 Å. 2D class averaging was performed on 4x down-scaled particles, and particles in secondary structure containing class averages were subject to two rounds of 3D class averaging with C1 symmetry. Particles were then used to generate a *de novo* D6 symmetric initial model in cryoSPARC and subjected to a round of 3D classification with D6 symmetry. Particles from the best 3D class average were re-extracted from the micrographs, down-scaled 2x, and subjected to another round of 3D classification with D6 symmetry. Subsequent 3D auto-refinement with D6 symmetry resulted in a 6.1 Å model, which improved to 4.7 Å (gold-standard FSC) with particle polishing (**Extended Data Figure 2.5a**). 3D classification was then performed on the "polished" particles increasing the angular sampling incrementally from 7.5º to 0.9º. From the resulting three 3D classes (**Extended Data Figure 2.5b-d**), particles in two of the classes were subjected to 3D refinement, resulting in a 7.5 -Å map of the Cx26 GJC in the occluded state (**Extended Data Figure 2.5e**). Refinement of the remaining class resulted in a 4.5-Å map of the Cx26 GJC open state, that improved to 4.2 Å resolution (**Extended Data Figure 2.4h**) with post-processing (**Extended Data Figure 2.5f**).

Model Building.

Both pH 7.5 and pH 6.4 open models were built following the same procedure. The X-ray structure of Cx26 (PDB code: 5ERA (1)) was used as a starting model. The model was rigid-body fit into the cryoEM density map using UCSF Chimera (91), and the new coordinates for the model were saved with respect to the map. The real space refinement tool in Phenix (92) was used to refine the model to the B-factor sharpened cryoEM map with secondary structure restraints, reference model restraints, and electron scattering table

options selected (93). WinCoot (94) was used to perform local real-space refinement on selected fragments of the structure, as well as, to improve the fit of bulky side chains to the density. Amino acid assignment was confirmed based on the clearly defined side chains densities of bulky residues Phe, Tyr, Trp, Arg, Lys, and Met. Residues 214 and 215 were deleted from the cytoplasmic end of the M4 helix due to insufficient density, and amino acids 17 and 134 were added to the cytoplasmic ends of M1 and M3 based on additional density in these regions. The lower-resolution cytoplasmic interface, containing the ends of M1-M4 helices, required contouring at decreased sigma levels compared to the majority of M1-M4 helical regions. Amino acids 85 – 96 in the M2 helix had the most incomplete density coverage. As was the case with the X-ray structure, the cytoplasmic domains CL (residues 97 – 133) and CT (residues 214 – 235) were missing from the cryoEM maps. The highest-resolution extracellular gap region retained its structural organization from the starting X-ray structure and allowed for an unambiguous assignment of most side chains. The unsharpened map was used in assigning the N-terminal domain from another Cx26 X-ray structure (PDB code: 2ZW3 (18)) into a stretch of density lining the channel pore, proximal to the M1 helix. The NT fragment corresponding to amino acids 2 – 15 was extracted from the reference structure in WinCoot and manually docked into the unsharpened map. Residues M1 and H16 were added, and the NT fragment was connected to the M1 helix. The loop connecting the M1 helix to the helical part of NT, consisting of residues 12 – 18, as well as the end of NT with residues 1 – 4, were refined using the real space refine and regularize zone tools in WinCoot. The helical part of the NT domain, residues 5 – 11, was left unmodified. The models were analyzed for rotamer outliers and clashes using the validation tools in WinCoot, and residual conformational clashes were

manually corrected. Changes made to one chain of the model were applied using non-crystallographic symmetry (NCS) to all 12 chains of the Cx26 gap junction channel. The models were subjected to two cycles of refinement in Phenix and manual adjustment in WinCoot. The structures were validated using MolProbity (95) as a part of Phenix and EMRinger (96). The final models exhibit good geometry as indicated by the Ramachandran plot (neutral pH: favored, 88.37%; allowed, 11.05%; outliers, 0.58% and acidic pH: favored, 84.30%; allowed, 15.70%; outliers, 0.00%).

The acidic pH occluded model was based on the same starting structure as the other two models. After real-space refinement in Phenix, the backbone of M1-M4 helices was adjusted in WinCoot. Structural manipulations were limited to the Cα and main chain atoms, as the resolution did not allow for assignment of amino acid side chains. N-terminal resides 1 – 17 were added, rigid docked into the density, and refined to improve the fit. The refinement resulted in loss of helical structure for the residue 5 – 11 segment as the N-terminal fragment extended into occluding density in the channel pore. The models were validated as described above. Ramachandran plot indicated good geometry for the full model with NT domains (favored, 84.30%; allowed, 15.70%; outliers, 0.00%).

Fluorescent Thermal Stability Assay.

Thermal stability of Cx26 in DDM and in amphipol A8-35 was measured by the fluorescence of the cysteine-reactive dye 7-diethylamino-3-(4'-maleimidylphenyl)-4-methylcoumarin (CPM) over a temperature gradient. The Cx26 construct used for cryoEM (1) has only one free cysteine at position 202, in the middle of M4. Upon increasing the temperature, Cx26 unfolds, and the dye binds to the C202 thiol and emits fluorescence at

463 nm. For experiments on Cx26 in DDM at pH 7.5, the buffer consisted of 50 mM Hepes pH 7.5, 500 mM NaCl, 2.5 % glycerol (v/v), 0.025% DDM. Experiments at lower pH were performed in MES-based buffer at pH of 6.5 or 6.0. For Cx26 samples in amphipol A8-35, no detergent was added to the buffers. An aliquot of CPM dye (Invitrogen) at 10 mM in dimethylformamide was diluted 1:150 into either a sample of protein at ~300 μg/ml or a buffer-only control. Following a 15-min incubation on ice, the sample was transferred into a 1.5 mm path-length quartz spectrofluorometer cuvette (Hellma Analytics, Müllheim, Germany), which was inserted into a FluoroMax-3 spectrofluorometer (Horiba Jobin-Yvon, Edison, NJ). The excitation and emission wavelengths were set to 387 nm and 463 nm, respectively. The sample was heated from 6 – 96 ^{o}C at a rate of 2 ^{o}C/min, and the fluorescence was recorded every 1 min. The fluorescence versus temperature profile was analyzed as described in (97).

Hydrogen Deuterium Exchange and Data Analysis.

Protein sample in HDX buffer (50 mM Hepes pH 7.5, 500 mM NaCl, 0.025% DDM) was concentrated to ~5.2 mg/ml (200 uM), frozen in liquid nitrogen, and stored at -80^{o}C. Initially, tandem mass spectrometry (MS/MS) was used to optimize protein concentration, protease digestion times, and quench conditions for maximum protein sequence coverage with recovered peptides. MS/MS data were acquired separately from HDX data, in experiments with a 60 min gradient column. Data-dependent MS/MS was performed in the absence of exposure to deuterium. The amino acid sequence of each peptide used in the HDX peptide set were confirmed if they had a MASCOT score of 20 or greater and had no ambiguous hits using a decoy (reverse) database. A post-translational

modification (PTM) of the methionine 1 residue with an acetyl cap (Ac-Met) of the 1 – 7 peptide was included in MASCOT search. The best condition identified yielded a 74 % peptide recovery. Shortly before HDX experiments, the sample was thawed on ice and diluted 1:3 (v/v) to ~50 uM protein in either HDX buffer pH 7.5 (50 mM Hepes pH 7.5, 500 mM NaCl, 0.025% DDM) or pH 6 (50 mM MES pH 6, 500 mM NaCl, 0.025% DDM). Solution-phase amide HDX was carried out with a fully automated system as described previously(98) with slight modifications. The automation system (CTC HTS PAL, LEAP Technologies, Carrboro, NC, USA) was housed inside a chromatography cabinet held at 4 °C. For each HDX reaction, 5 μL of 50 μM Cx26 at pH 7.5 or 6 was diluted to 25 μL with D_2O-containing HDX buffer (either pH 7.5 or pH 6) and incubated at 4 °C for 10, 30, 60, 900, or 3600 s. Following exchange, unwanted forward or back exchange was minimized, and the protein was denatured by dilution to 50 μL with 0.1 % (vol/vol) TFA in 3 M urea and 20 mM TCEP, 0.025 % DDM. Samples were then passed over an immobilized pepsin column (prepared in house(99)) at 50 μL/min (0.1 % vol/vol TFA, 15 °C); the resulting peptides were trapped on a C8 trap cartridge (Hypersil Gold, Thermo Fisher). Peptides were then gradient-eluted (4 % (w/v) CH_3CN to 40 % (w/v) CH_3CN, 0.3 % (wt/vol) formic acid over 5 min, at 4 °C) across a 1 mm × 50 mm C18 HPLC column with an 8 min gradient (Hypersil Gold, Thermo Fisher) and subjected to electrospray ionization directly coupled to a high-resolution (60,000) Orbitrap mass spectrometer (LTQ Orbitrap XL with ETD, Thermo Fisher). For on-exchange experiments, the intensity-weighted average m/z value (centroid) of each peptide's isotopic envelope was calculated using software developed in-house (100). For back exchange correction, full deuterium control was run as reported previously (101), and 59% peptide recovery was calculated. The temperature was constant

at 4 °C in all HDX experiments. To measure the difference in exchange rates between experiments conducted at pH 7.5 and 6, we calculated the average percent deuterium uptake for peptides from both samples following 10, 30, 60, 900, and 3600 s of on-exchange. Intrinsic exchange rate (K_{ch}) at pH 6.0 was converted to pH 7.5 using an equation describing the temperature and pH dependence of amide hydrogen exchange rate (102). After normalization, a time point of ~10 and ~30 seconds was used to calculate the average percent HD exchange in Cx26 at pH 7.5 and pH 6.0.

Protein crosslinking and MS/MS analysis.

We performed lysine proximity crosslinking with bis(sulfosuccinimidyl)suberate (BS3) at either pH 7.5 or 6 and confirmed the presence of crosslinks by SDS-PAGE gel analysis (**Extended Data Figure 2.10**), in which BS3-crosslinked Cx26 migrated as a hexamer. The conditions sufficient for efficient crosslinking were 1mM BS3 (diluted from freshly made 100mM stock in ddH_2O) and incubation with protein for 1 h at 4 ^oC. In order to ensure proper pH for crosslinking, protein samples were diluted three-fold to ~1.2mg/ml with either pH 7.5 or 6.0 buffer. The compositions of these buffers were 50 mM HEPES pH 7.5, 500 mM NaCl, 0.025 % DDM and 50 mM MES pH 6.0, 500 mM NaCl, 0.025 % DDM, respectively. At the end of the reaction time, excess BS3 reagent was quenched with 1M Tris pH 7.5 to a final concentration of 50mM. Protein samples were then exchanged into pH 7.5 buffer in preparation for trypsin digestion. A desalting column (GE Healthcare, G-25) was equilibrated with 4 x 1 ml of ice-cold pH 7.5 buffer, and sample volume was increased to 0.5 ml and loaded onto the column. Protein was eluted with 1 ml of ice-cold pH 7.5 buffer. The collected eluate from the desalting column was concentrated to ~2

mg/ml (~80 uM) using a 0.5 ml or 4 ml concentrator (100 kDa MWCO; Millipore) at a speed of ~1000 x g at 4 ^{o}C. Using mass spectrometry (MS), we confirmed the presence of the acetylated N-terminal peptide of Cx26 (residues 1 – 150) in the trypsin digest. The samples were flash-frozen in liquid N_2 and stored at -80 ^{o}C until digestion. Trypsin digestion was performed at 37 ^{o}C for 12 hrs. Tandem mass spectrometry (MS/MS) was used to separate resulting peptides and crosslinked peptide pairs. MS/MS analysis was performed as described in (72). MassMatrix software (103) was used to identify detected peptides. All detected lysine crosslinks were organized on separate heat maps for either pH 7.5 or pH 6 condition, with color intensity indicating crosslinking efficiency. The crosslinks were then evaluated based on their PP and PPtag scores (both statistical) and color tag number, which are indicative of the quality of a peptide match, with higher values determining higher confidence in the match. Low-confidence crosslinks were not analyzed further and neither were the low-scored crosslinks with lysine 168, which were interpreted as occurring in between different Cx26 GJC proteins. The remaining crosslinks could be assigned into three groups, based on where in the cytoplasmic domains the crosslinking reaction occurred: NT-CL, CL-CL and CL-CT.

2.7. Extended data figures and tables

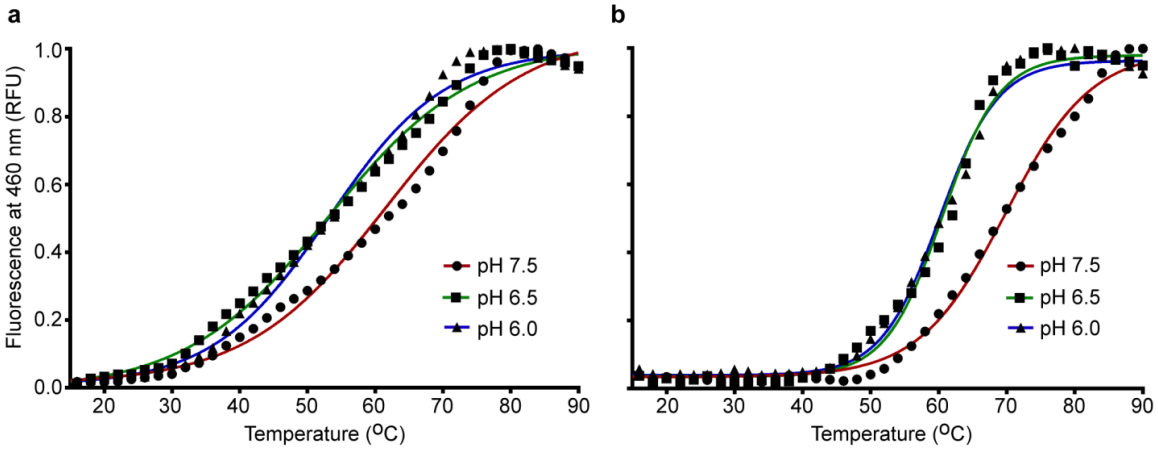

Extended Data Figure 2.1. Fluorescent thermal stability assay. Thermal stability of Cx26 in FA-3 as measured by the fluorescence of a cysteine-reactive, coumarin-based dye (CPM) over a temperature gradient (15 to 90ºC) The T_m was calculated from the Boltzmann fit of each curve. (**a**) Stability in DDM: T_m = 60ºC (pH 7.5), 52ºC (pH 6.5), 52ºC (pH 6.0). (**b**) Stability in amphipol A8-35: T_m = 69ºC (pH 7.5), 60ºC (pH 6.5), 59ºC (pH 6.0). *Experiment performed by Maciej Jagielnicki*.

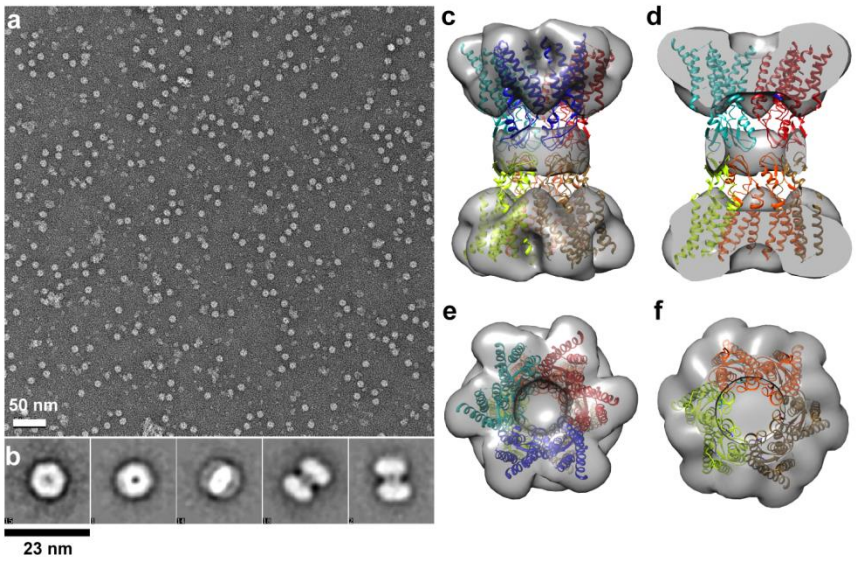

Extended Data Figure 2.2. Negative-stain EM and single-particle analysis. (**a**) A representative image of Cx26 GJC in amphipol, stained with uranyl acetate. (**b**) Select 2D class averages showing the particle top view, side view and in-between tilted view. A side view (**c**) and a top view (**e**) of the EM density map calculated at 29 Å resolution with Cx26 GJC X-ray structure (pdb: 5ERA) rigid-docked. (**d**) and (**f**) are the cutaways of the views shown in (**c**) and (**e**), respectively. Map volume adjusted based on Cx26 partial specific volume (for 0.74 cm^3/g). *Negative stain EM performed by Maciej Jagielnicki*.

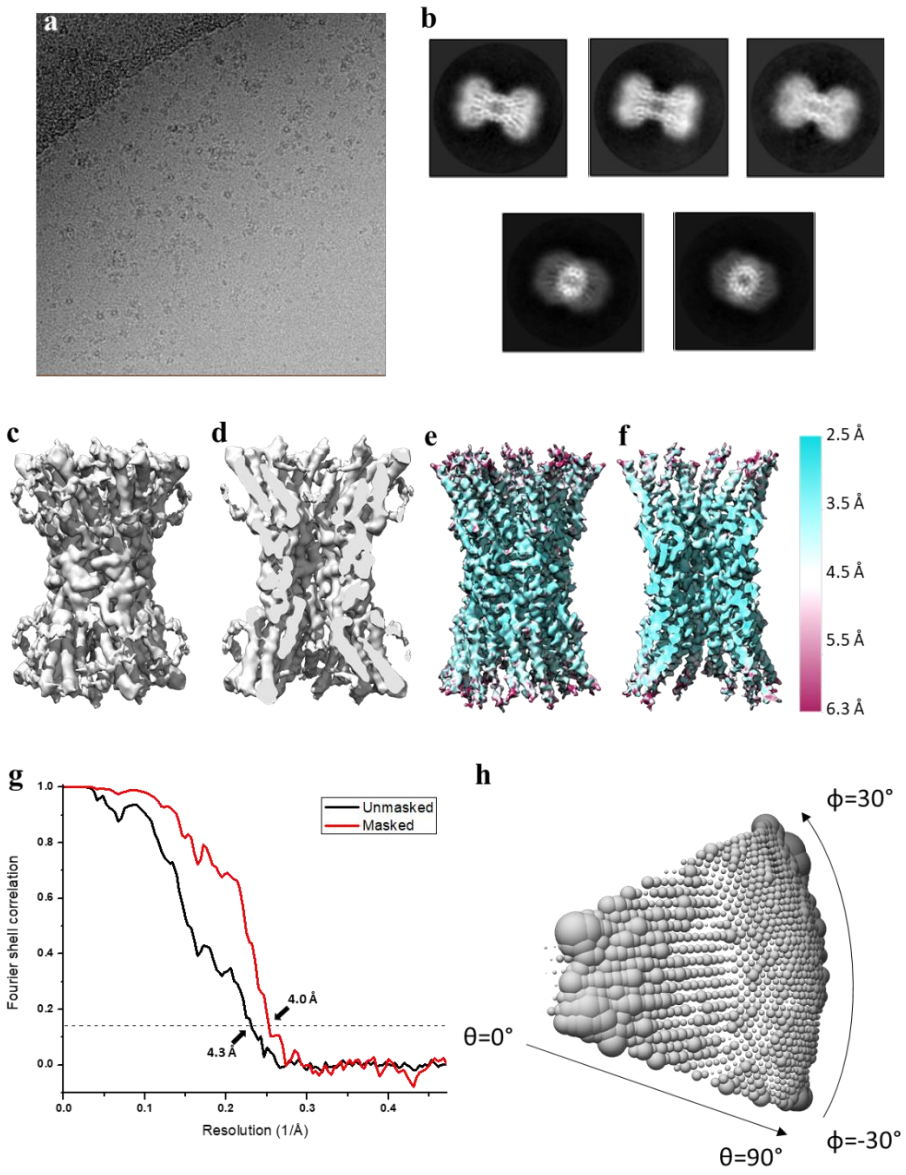

Extended Data Figure 2.3. Single-particle image processing of the Cx26 GJC at physiological pH. (**a**) Representative raw micrograph and (**b**) 2D class averages. (**c**) Density after refinement is shown with cropped-view (**d**) to display the interior of the pore. (**e-f**) Post-processed map colored by local resolution calculation by Resmap reveals that resolution is highest in the transmembrane and extracellular domains and lowest in the cytoplasmic domains. (**g**) Gold-standard Fourier Shell Correlation (FSC) shows the global resolution of the map before and after masking performed in post-processing to be 4.3 Å and 4.0 Å, respectively. (**h**) Euler angle distribution of particles depicted as relative size of grey spheres.

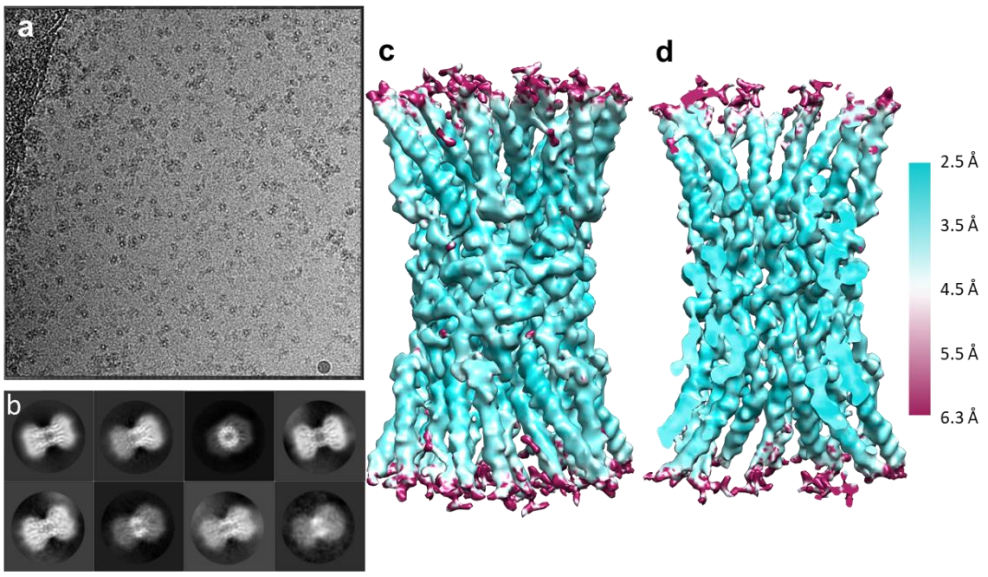

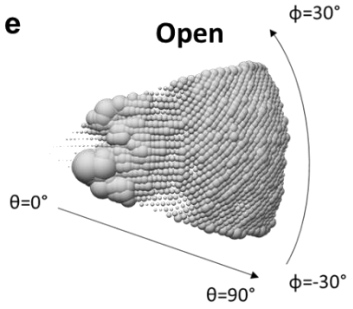

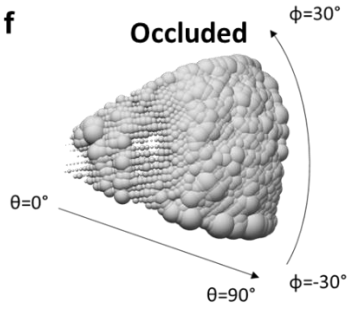

g

	Open	Occluded
Number of Micrographs	1,503 / 1,503	1,503 / 1,503
Defocus Mean	2.2 µm	2.1 µm
Defocus Median	2.3 µm	2.1 µm
Defocus Standard Deviation	0.8 µm	0.8 µm

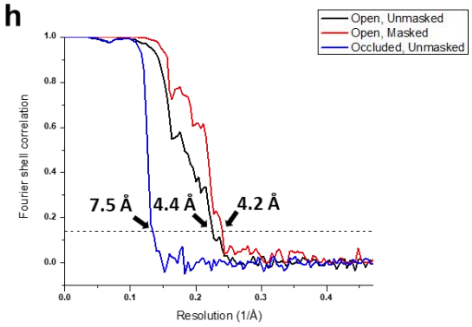

Extended Data Figure 2.4. Single-particle image processing of the Cx26 GJC at pH 6.4. (**a**) Representative raw micrograph and (**b**) 2D class averages. (**c**) Post-processed map of open structure is shown with cropped-view **(d)** colored by local resolution calculation by Resmap. Euler angle distribution of open state (**e**) and occluded state (**f**) particles depicted as relative size of grey spheres. (**g**) Both open and occluded maps were calculated from the same final 1503 micrographs and have similar defocus values. (**h**) Gold-standard Fourier Shell Correlation (FSC) shows the global resolution of the map before and after masking performed in post-processing to be 4.4 Å and 4.2 Å, respectively. The resolution for the unmasked occluded structure is 7.5 Å.

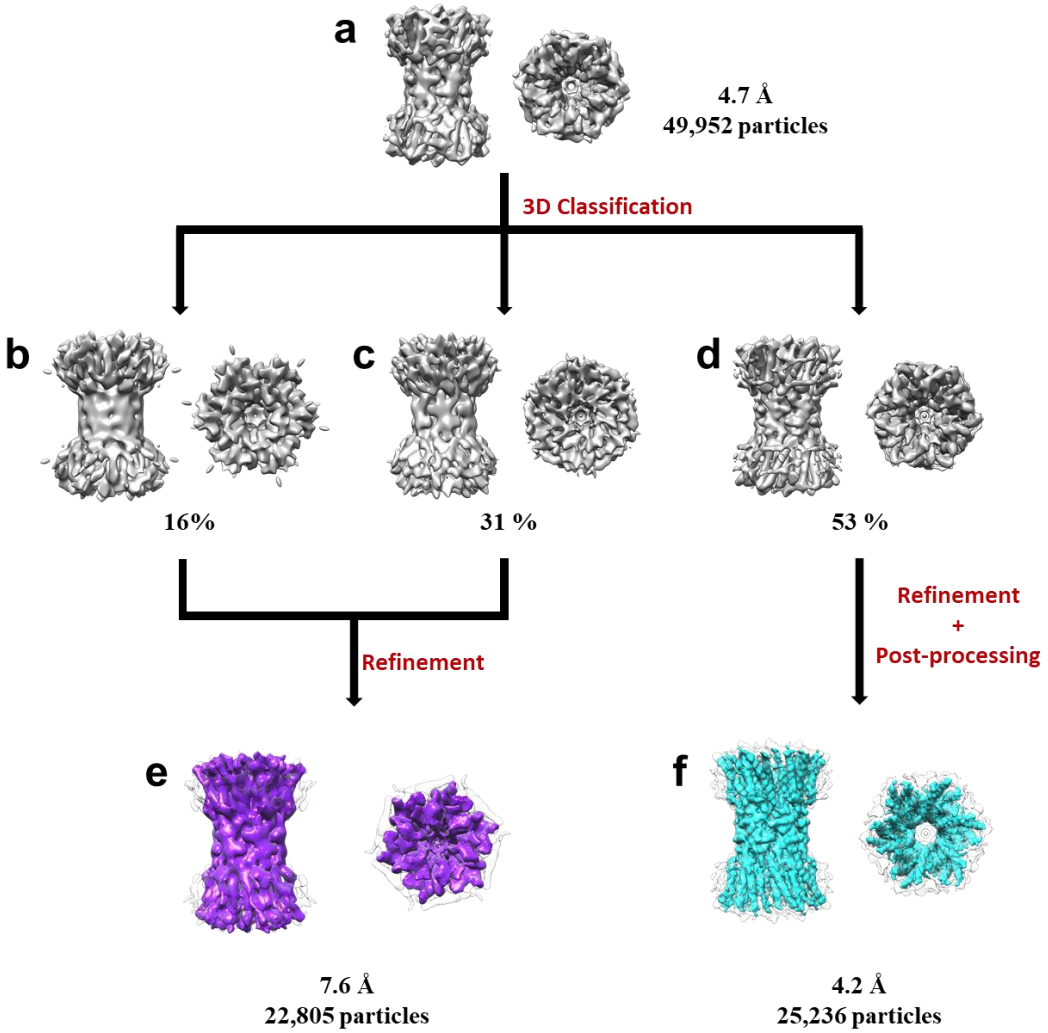

Extended Data Figure 2.5. 3D Classification and refinement of the Cx26 GJC at acidic pH. Initial refinement and particle polishing resulted in a 4.7 Å resolution model (**a**), which was subjected to 3D classification while increasing the angular sampling incrementally from 7.5º to 0.9º. From the resulting three classes (**b-d** shown with relative particle distribution), particles in two classes underwent 3D refinement to create the channel in the occluded state at 7.6 Å (purple) (**e**) shown with amphipol density in white. Refinement of the remaining class reconstructed the open state of the channel at 4.5 Å resolution (white) and improved to 4.2 Å resolution with post-processing (cyan). All maps are contoured at 4 sigma (σ) with the exception of **f**, which is contoured at 4.5 sigma (σ).

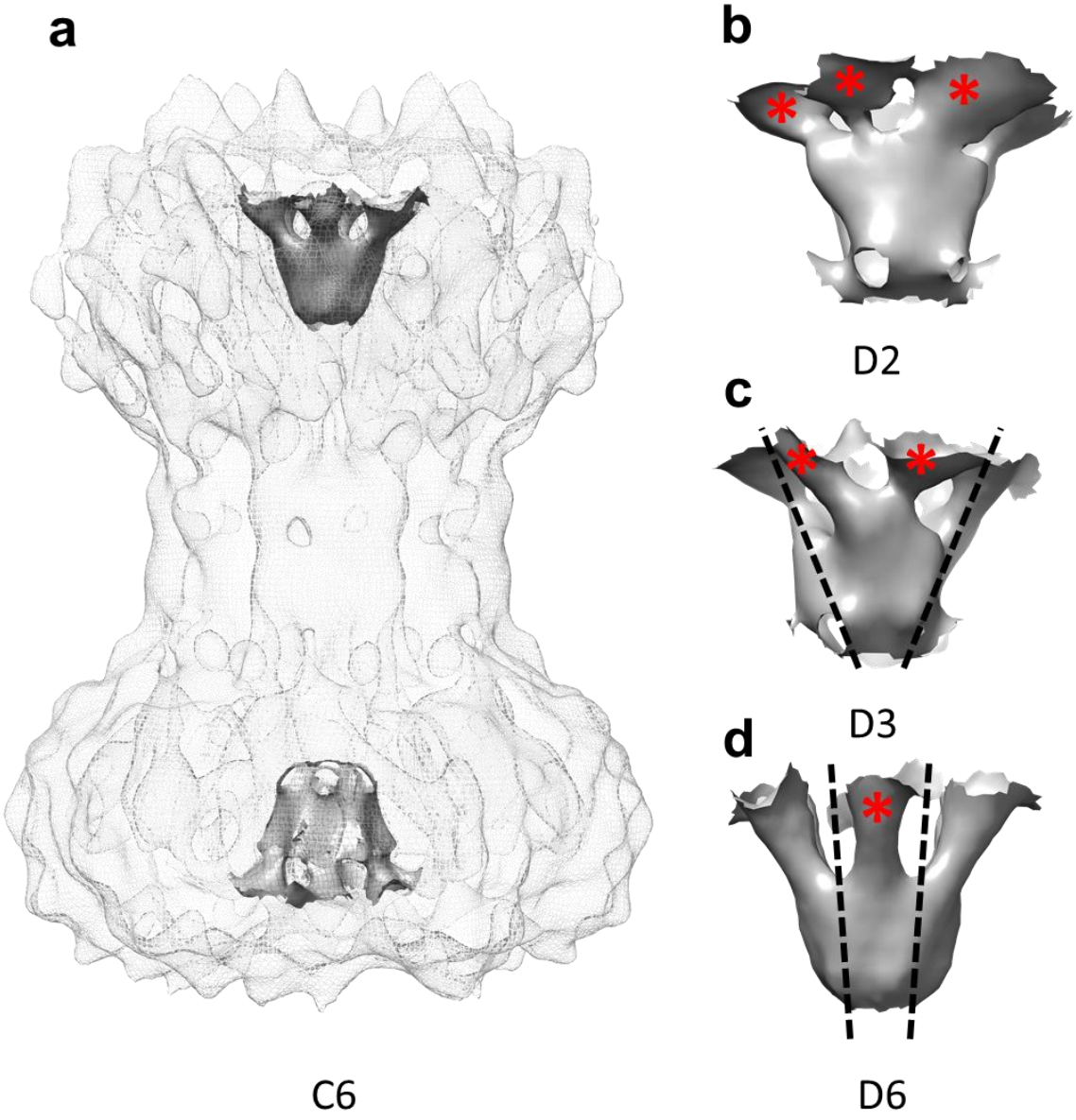

Extended Data Figure 2.6. "Ball" and "chains" are conserved when cryoEM density is refined at lower symmetry values. (**a**) C6 symmetry refinement shows the "ball-and-chain" densities (grey) in both hemichannels. D2 (**b**), D3 (**c**), and D6 (**d**) refinements show six chains attached to the ball. Dotted lines roughly demarcate the symmetry axis and the red asterisk (*) specify each chain density within a single asymmetric unit of the plug. The D2 symmetry axis is parallel with the page.

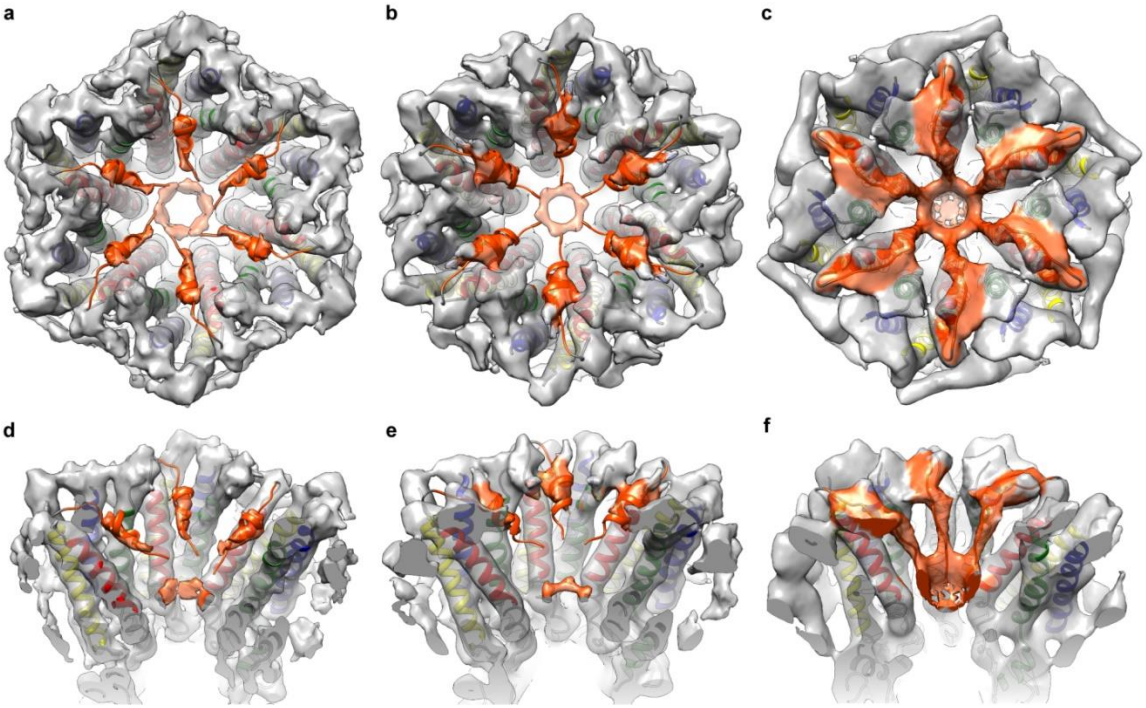

Extended Data Figure 2.7. Analysis of cryoEM maps and models showing pH-gating in Cx26 mediated by NT domains. End-on views of Cx26 hemichannel from the cytoplasmic side extending to the end of transmembrane helices at the extracellular gap; pH 7.5 structure (**a**), pH 6.4 structure (**b**) and pH 6.4 'plug' structure (**c**). Tilted cross-sectional views of Cx26 hemichannel showing the organization of three monomers; pH 7.5 structure (**d**), pH 6.4 structure (**e**) and pH 6.4 'plug' structure (**f**). M1 helix (red), M2 helix (green), M3 helix (blue), M4 helix (yellow), NT domain 1-15 aa (orange), cryoEM densities (transparent light grey) and NT densities (transparent orange). To aid in interpretation, helices M1 and M4 of the central monomer in panel (**f**) were not colored (white). Maps displayed at 4 sigma (σ). Maps shown are without masking or sharpening procedures applied, at a resolution of 4.4 Å (pH 7.5), 4.5 Å (pH 6.4) and 7.6 Å (pH 6.4 closed).

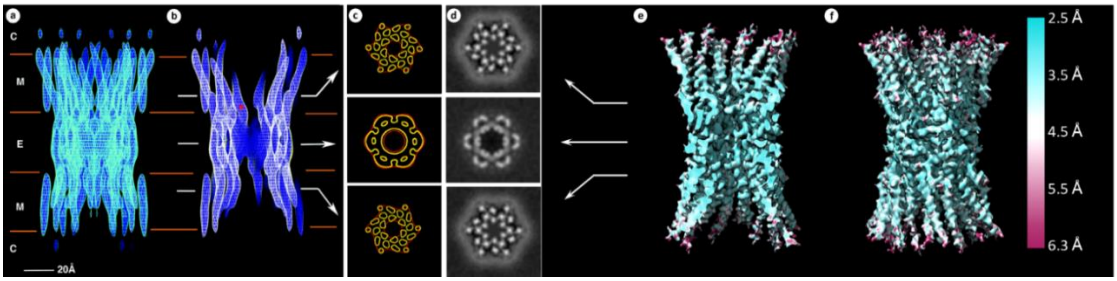

Extended Data Figure 2.8. Comparison of Cx43 electron crystallography structure with Cx26 single-particle cryoEM structure. (**a**) Side view, (**b**) side view with cropped density to show channel interior, and (**c**) cross sections parallel to membrane bilayer of recombinant Cx43 channel solved to 7.5 Å in the membrane plane and 21 Å in the vertical direction. The approximate boundaries for membrane bilayer (M), extracellular gap (**E**), and cytoplasmic side (**C**) are indicated. Images (**a**), (**b**), and (**c**) are from (14). (**d**) Slice views of 3D density map of Cx26 single-particle cryoEM structure shown as side view (**f**) and side view with cropped density (**e**). (**e**) and (**f**) are colored by local resolution calculated by ResMap (104) with color bar shown.

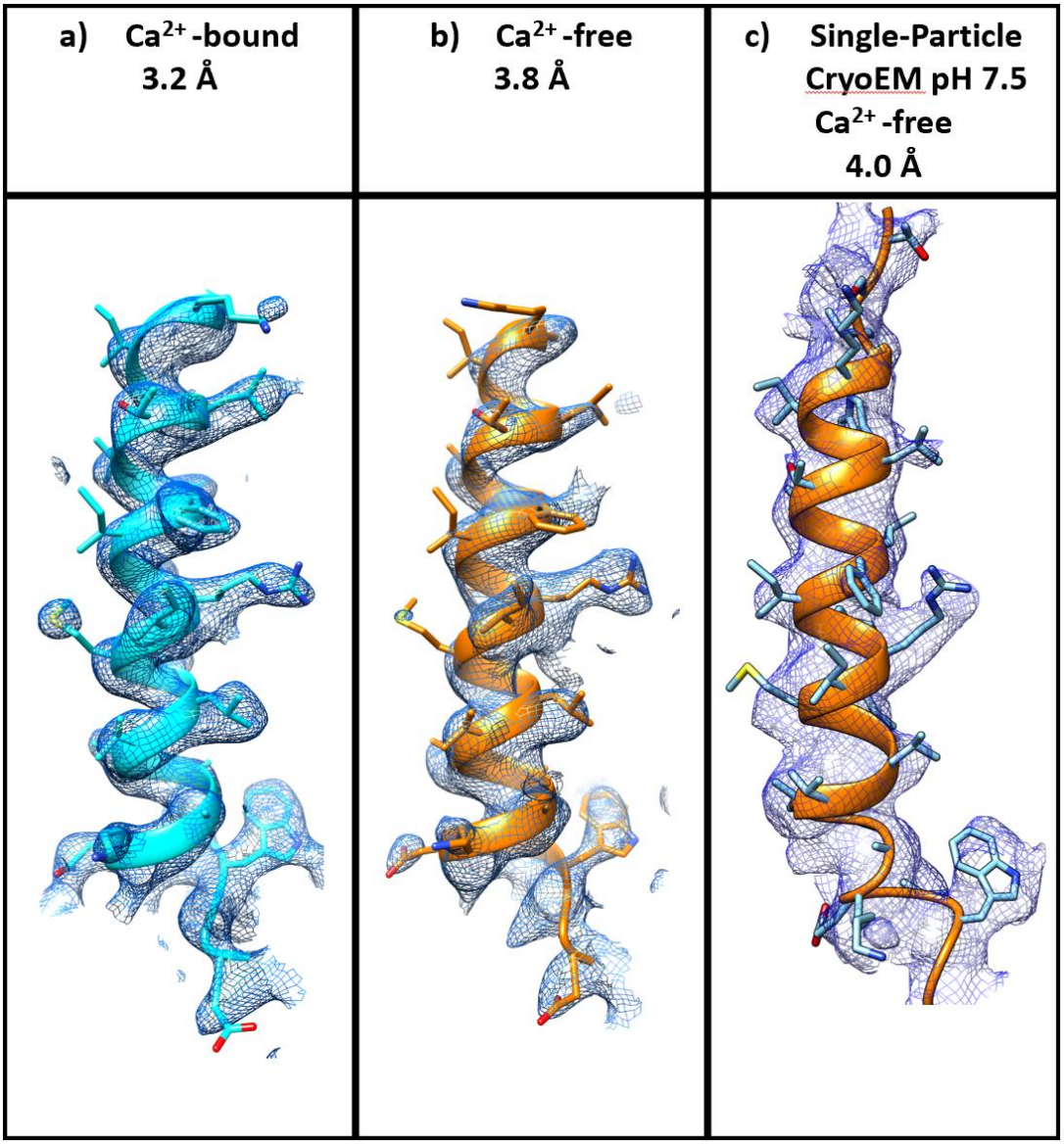

Extended Data Figure 2.9. Cx26 M1 Helix (residues 17-46). Comparison between the M1 helix calculated by X-ray crystallography with calcium (**a**), without calcium (**b**), and by single-particle cryoEM at pH 7.5(**c**).

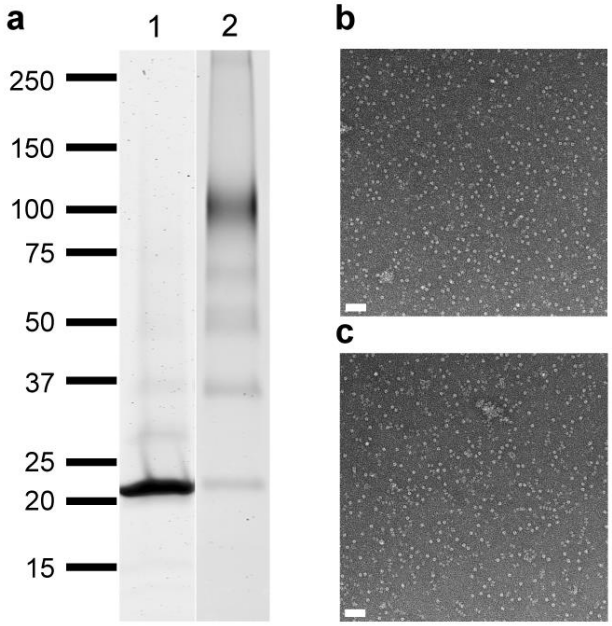

Extended Data Figure 2.10. Lysine crosslinking with BS3 and DST. (**a**) SDS-PAGE shown as a Coomassie stained gel; lane 1: Cx26, lane 2: Cx26 treated with BS3 at 1mM for 1h at 4^{o}C. (**b**-**c**) Negative-stain EM electron micrograph of Cx26 (**b**) and of Cx26 treated with BS3 (**c**). White bars on the EM micrographs denote 50 nm. *Experiment by Maciej Jagielnicki and William McIntire.*

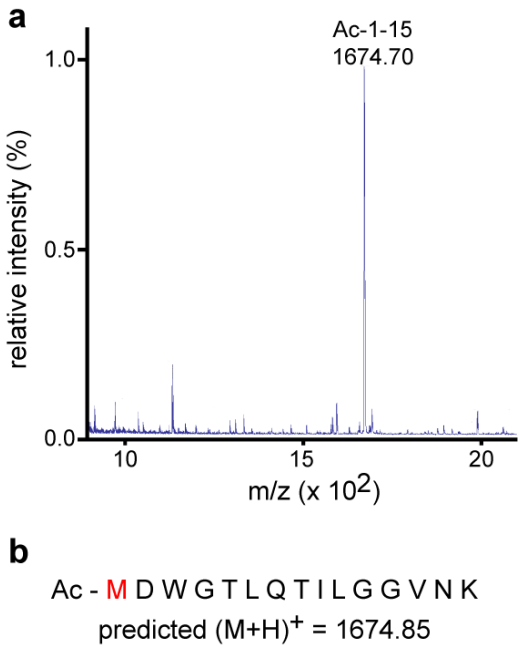

Extended Data Figure 2.11. Mass spectrometry analysis of trypsin-digested Cx26 GJC reveals a mass corresponding to an acetylated NT. *Experiments by Maciej Jagielnicki, William McIntire, Venkat Dharmarajan, and Patrick R. Griffin .*

Summary of CryoEM Data Collection and Processing			
	pH 7.5	**pH 6.4 (Open)**	**pH 6.4 (Closed)**
Voltage (kV)	300	300	300
Magnification	130,000	130,000	130,000
Camera	Gatan K2 Summit	Gatan K2 Summit	Gatan K2 Summit
Camera Mode	Counting	Super-resolution	Super-resolution
GIF quantum energry filter slit-width (eV)	20	20	20
Defocus	-2.0 to -3.5	-1.2 to -3.5	-1.2 to -3.5
Pixel size (Å)	1.06	0.53	0.53
Total electron dose ($e^-/Å^2$)	45	45	45
Exposure time (s)	8	10	10
Initial number of images	2,401*	1,547**	1,547**
Number of frames per image	20	25	25
Initial particle number	64,087	449,556	449,556
Final particle number	10,345	25,236	22,805
Resolution (unmaksed, Å)	4.4	4.5	7.5
Resolution (maksed, Å)	4.0	4.2	

*After removal of micrographs with estimated resolution limits worse than 3.3 Å

**After removal of micrographs with estimated resolution limits worse than 3.75 Å

Extended Data Table 2.1. Summary of CryoEM Data Collection and Processing.

Refinement and Validation						
	pH 7.5		pH 6.4 (Open)		pH 6.4 (Closed)	
	NTs	no NTs	NTs	no NTs	NTs	no NTs
Starting model RMSD (Å)	1.2	1.2	1.3	1.3	2.2	2.2
Ramachandran						
Favored (%)	88.4	91.0	84.3	84.6	84.3	85.3
Allowed (%)	11.1	8.3	15.7	15.4	15.7	14.7
Outlier (%)	0.6	0.6	0.0	0.0	0.0	0.0
RMSD						
Bond length (Å)	0.010	0.010	0.008	0.009	0.008	0.008
Bond angles (°)	1.190	1.176	1.137	1.155	1.283	1.319
EMRinger score	2.71	2.83	1.55	1.57	< 0	< 0
Map cross correlation	0.75	0.77	0.74	0.75	0.78	0.76

Extended Data Table 2.2. Statistics of atomic model refinement. Start model RMSD was calculated in Chimera between a model built to cryoEM density and starting X-ray structure (pdb: 5ERA). Map cross correlation (CC) was obtained in real-space refinement tool in Phenix. The remaining parameters were calculated in either EMRinger (EMRinger score) or MolProbity, both distributed with Phenix package.

RMSD (Cα)				
Region	Residue range	pH 7.5 vs pH 6.4 open	pH 7.5 vs pH 6.4 closed	pH 6.4 vs pH 6.4 closed
M1 helix	20 - 38	0.2	0.3	0.3
M2 helix	73 - 92	0.3	1.5	1.5
M3 helix	137 - 157	0.4	0.3	0.5
M4 helix	185 - 210	0.2	0.4	0.5
EL1 domain	158 - 184	0.5	0.6	0.8
EL2 domain	39 - 72	0.3	0.6	0.6

Extended Data Table 2.3. RMSD values for Cα atoms between neutral pH open, low pH open and low pH closed structures. RMSD calculations were performed in Chimera.

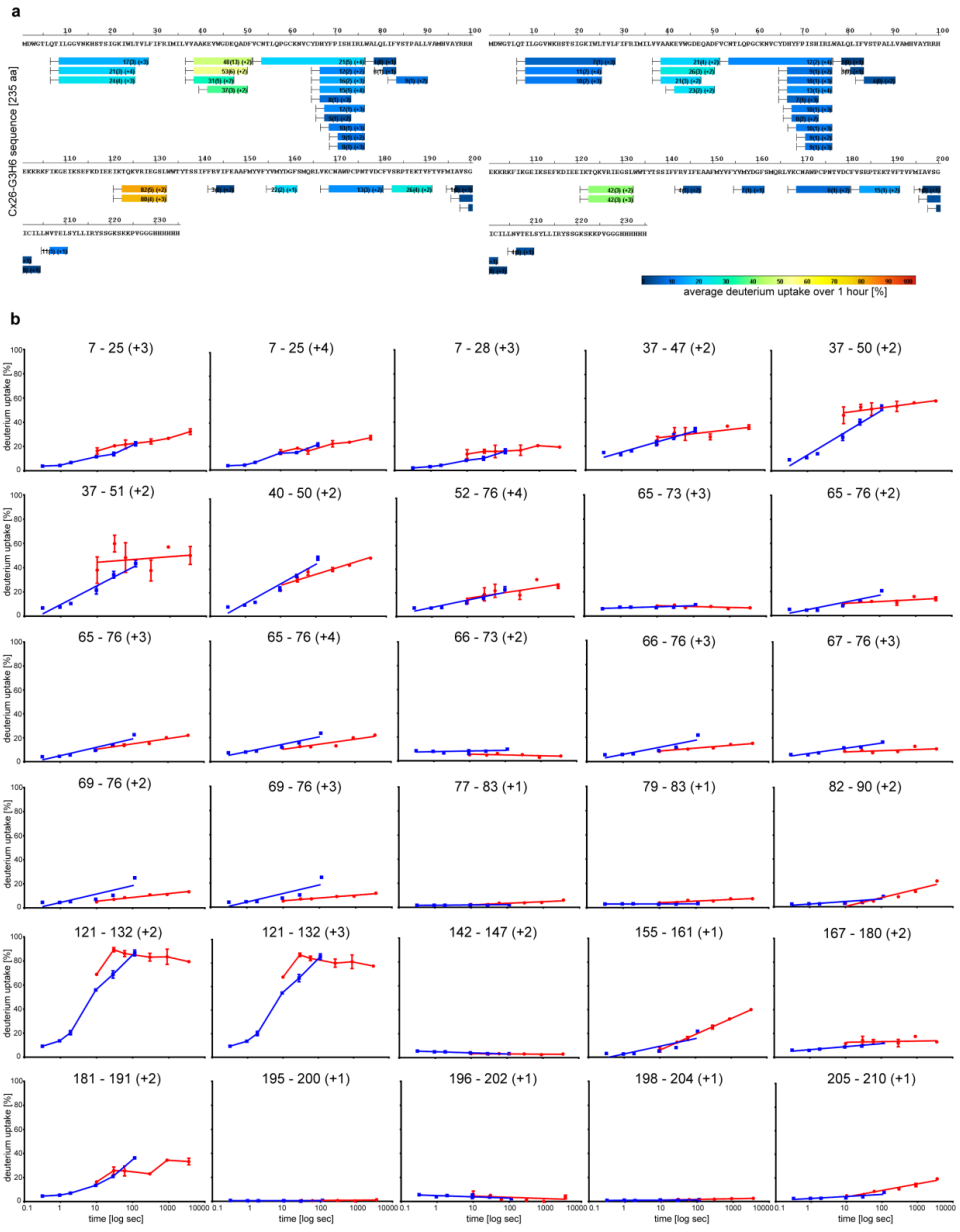

Extended Data Table 2.4. Dynamics of Cx26 GJC as revealed by hydrogen-deuterium exchange (HDX). (**a**) HDX results obtained at physiological pH 7.5 (left) and acidic pH 6.0 (right), mapped onto Cx26 sequence. The bars below the sequence represent the peptide fragments resolved by mass spectrometry and the bar color represents the relative deuterium/hydrogen exchange (color code on the bottom). Number within each bar is the average % of deuterium incorporated over six time points (10, 30, 60, 300, 900, and 3600 s). (**b**) Deuterium build-up curves of all detected peptides. Curves for pH 7.5 peptides (red) and pH 6.0 peptides (blue). The pH 6.0 curves were translated in time due to slower exchange rate of amide hydrogen. *Experiments by Maciej Jagielnicki, William McIntire, Venkat Dharmarajan, and Patrick R. Griffin.*

Crosslinks pH 7.5								
crosslink	region 1	peptide 1	region 2	peptide 2	Crosslink score	PP score	PP2 score	PPtag score
N-terminal crosslinks								
15-103	1:22	MDWGTLQTILGGVNK($1)HSTSIGK	103:105	K($1)RK	30.25	10.4	6.4	2.9
15-122	2:22	DWGTLQTILGGVNK($1)HSTSIGK	117:125	DIEEIK($1)TQK	11.86	8.9	6.7	1.4
15-125	2:22	DWGTLQTILGGVNK($1)HSTSIGK	123:127	TQK($1)VR	10.28	7.4	4.2	2.1
22-116	16:32	HSTSIGK($1)IWLTVLFIFR	113:122	SEFK($1)DIEEIK	16.72	8.0	9.1	1.7
22-122	16:32	HSTSIGK($1)IWLTVLFIFR	117:127	DIEEIK($1)TQKVR	19.56	6.6	8.9	2.1
C-loop crosslinks								
102-105	100:103	HEK($1)K	105:108	K($1)FIK	99.58	20.7	15.8	8.2
105-103	105:108	K($1)FIK	103:104	K($1)R	42.30	6.0	9.5	3.6
108-102	106:112	FIK($1)GEIK	100:103	HEK($1)K	101.94	10.1	6.7	11.4
108-103	106:112	FIK($1)GEIK	103:104	K($1)R	144.58	21.4	7.3	11.2
108-125	106:112	FIK($1)GEIK	123:127	TQK($1)VR	108.84	22.0	6.6	14.9
112-102	109:116	GEIK($1)SEFK	100:103	HEK($1)K	75.52	22.0	9.7	9.9
112-103	109:116	GEIK($1)SEFK	103:104	K($1)R	92.74	12.0	6.6	11.6
112-105	109:116	GEIK($1)SEFK	105:108	K($1)FIK	80.93	15.6	7.9	13.9
112-125	109:116	GEIK($1)SEFK	123:127	TQK($1)VR	128.98	27.7	6.3	13.6
116-102	113:122	SEFK($1)DIEEIK	100:103	HEK($1)K	91.12	28.1	9.1	16.0
116-103	113:122	SEFK($1)DIEEIK	103:104	K($1)R	114.00	21.6	7.0	15.2
116-105	113:122	SEFK($1)DIEEIK	105:108	K($1)FIK	206.92	18.9	8.3	20.3
116-108	113:122	SEFK($1)DIEEIK	106:112	FIK($1)GEIK	130.42	21.4	5.8	18.6
116-125	113:122	SEFK($1)DIEEIK	123:127	TQK($1)VR	124.38	26.3	6.2	16.4
122-102	117:125	DIEEIK($1)TQK	100:103	HEK($1)K	135.41	27.3	9.7	14.2
122-103	117:125	DIEEIK($1)TQK	103:104	K($1)R	235.09	25.1	7.6	18.3
122-105	117:125	DIEEIK($1)TQK	105:108	K($1)FIK	211.04	26.6	9.1	20.2
122-108	117:125	DIEEIK($1)TQK	105:112	KFIK($1)GEIK	132.58	15.1	8.4	8.3
122-112	117:125	DIEEIK($1)TQK	109:116	GEIK($1)SEFK	115.47	22.5	6.0	15.8
125-102	123:127	TQK($1)VR	100:103	HEK($1)K	94.90	24.1	9.3	11.0
125-103	123:127	TQK($1)VR	103:104	K($1)R	65.46	13.9	6.8	5.2
125-105	123:127	TQK($1)VR	105:108	K($1)FIK	108.56	19.7	8.0	7.8
C-terminal crosslinks								
105-223	105:108	K($1)FIK	222:224	SK($1)K	84.47	6.1	6.1	3.8
108-221	106:112	FIK($1)GEIK	217:223	YSSGK($1)SK	77.71	17.2	6.6	11.9
108-223	106:112	FIK($1)GEIK	222:224	SK($1)K	100.40	14.6	9.0	7.8
112-221	109:116	GEIK($1)SEFK	217:223	YSSGK($1)SK	61.70	12.0	6.6	11.6
112-223	106:116	FIKGEIK($1)SEFK	222:224	SK($1)K	42.02	7.0	4.8	3.1
116-221	113:122	SEFK($1)DIEEIK	217:223	YSSGK($1)SK	103.22	27.2	7.0	17.0
116-223	113:122	SEFK($1)DIEEIK	222:224	SK($1)K	91.40	17.5	4.9	11.9
116-224	109:122	GEIKSEFK($1)DIEEIK	222:235	SKK($1)PVGGGHHHHHH	31.17	7.2	6.6	3.0
122-221	117:125	DIEEIK($1)TQK	217:223	YSSGK($1)SK	143.25	12.2	8.5	5.3
122-223	117:125	DIEEIK($1)TQK	222:224	SK($1)K	103.09	22.9	9.4	15.8
221-102	217:223	YSSGK($1)SK	100:103	HEK($1)K	71.88	18.5	8.5	5.8
221-103	217:223	YSSGK($1)SK	103:104	K($1)R	69.58	13.2	11.4	6.1
221-105	217:223	YSSGK($1)SK	105:108	K($1)FIK	88.20	19.0	8.9	11.2
221-125	217:223	YSSGK($1)SK	123:127	TQK($1)VR	77.61	12.1	11.0	5.1
223-102	217:224	YSSGKSK($1)K	99:103	RHEK($1)K	58.38	16.4	11.1	4.6
223-103	222:235	SK($1)KPVGGGHHHHHH	103:105	K($1)RK	5.65	2.1	5.2	2.0
223-125	217:224	YSSGKSK($1)K	123:127	TQK($1)VR	27.65	5.6	8.4	1.9
224-102	224:235	K($1)PVGGGHHHHHH	100:103	HEK($1)K	11.42	7.7	5.4	2.5
224-103	224:235	K($1)PVGGGHHHHHH	103:105	K($1)RK	32.41	10.9	7.2	2.8
224-105	224:235	K($1)PVGGGHHHHHH	105:108	K($1)FIK	45.39	13.7	8.9	4.3
224-108	222:235	SKK($1)PVGGGHHHHHH	106:112	FIK($1)GEIK	38.16	4.4	6.5	8.1
224-122	222:235	SKK($1)PVGGGHHHHHH	117:125	DIEEIK($1)TQK	39.18	6.3	4.6	2.5
224-125	222:235	SKK($1)PVGGGHHHHHH	123:127	TQK($1)VR	20.24	10.8	4.9	2.8
224-221	224:235	K($1)PVGGGHHHHHH	217:223	YSSGK($1)SK	53.83	7.3	7.7	1.4

Extended Data Table 2.5. Mass spectrometry analysis of BS3 crosslinking experiment at pH 7.5. High-confidence crosslinked peptide pairs selected based on the PP and PPtag scores as well as the number of color tags. Higher PP and PPtag scores indicate better peptide match quality. The cut-off criterion for 'real' matches was set to 2.4 for PP score and 1.3 for PPtag score. Color tags on protein sequence indicate an amino acid residue with a pair of consecutive y ions (green), a pair of consecutive b ions (blue) or with both pairs of consecutive b and y ions (red). Tags provide a direct visual indication of match quality and the higher the number of color tags of a peptide match the better the match. Crosslinked lysines are labeled with a ($1) symbol. For same crosslinks identified in multiple peptide pairs, only the best pair was included in the table. *Experiments by Maciej Jagielnicki, William McIntire, Venkat Dharmarajan, and Patrick R. Griffin.*

Crosslinks pH 6.0								
crosslink	region 1	peptide 1	region 2	peptide 2	Crosslink score	PP score	PP2 score	PPtag score
N-terminal crosslinks								
15-105	2:22	DWGTLQTILGGVNK($1)HSTSIGK	104:108	RK($1)FIK	19.65	5.1	2.4	3.2
15-108	2:22	DWGTLQTILGGVNK($1)HSTSIGK	105:112	KFIK($1)GEIK	7.20	5.1	4.5	2.4
15-112	1:22	MDWGTLQTILGGVNK($1)HSTSIG	106:116	FIKGEIK($1)SEFK	6.35	3.9	5.8	1.5
15-122	2:22	DWGTLQTILGGVNK($1)HSTSIGK	117:125	DIEEIK($1)TQK	13.11	8.5	5.6	1.9
15-125	2:22	DWGTLQTILGGVNK($1)HSTSIGK	123:127	TQK($1)VR	15.23	7.4	4.3	1.9
22-102	16:32	HSTSIGK($1)IWLTVLFIFR	100:103	HEK($1)K	6.75	5.3	4.4	1.9
22-105	16:32	HSTSIGK($1)IWLTVLFIFR	105:108	K($1)FIK	7.45	4.7	5.2	2.5
22-116	16:32	HSTSIGK($1)IWLTVLFIFR	113:122	SEFK($1)DIEEIK	9.34	4.5	6.7	1.8
22-122	16:32	HSTSIGK($1)IWLTVLFIFR	117:127	DIEEIK($1)TQKVR	17.53	6.6	4.2	2.4
C-loop crosslinks								
102-105	100:103	HEK($1)K	105:108	K($1)FIK	124.07	7.2	10.7	3.6
105-103	105:108	K($1)FIK	103:104	K($1)R	67.06	14.7	13	8.4
108-102	106:112	FIK($1)GEIK	100:103	HEK($1)K	121.25	17.5	9.8	10.8
108-103	105:112	KFIK($1)GEIK	103:104	K($1)R	181.01	11.8	8.0	7.5
108-125	106:112	FIK($1)GEIK	123:127	TQK($1)VR	100.19	19.3	6.4	15.3
112-102	109:116	GEIK($1)SEFK	100:103	HEK($1)K	60.15	19.8	9.7	8.9
112-103	109:116	GEIK($1)SEFK	103:104	K($1)R	87.97	12.0	5.8	11.6
112-105	109:116	GEIK($1)SEFK	105:108	K($1)FIK	105.79	20.0	8.0	16.7
112-125	109:116	GEIK($1)SEFK	123:127	TQK($1)VR	105.46	19.5	6.2	12.8
116-102	113:122	SEFK($1)DIEEIK	100:103	HEK($1)K	75.08	28.1	9.3	16.0
116-103	113:122	SEFK($1)DIEEIK	103:104	K($1)R	109.75	23.2	7.8	12.6
116-105	113:122	SEFK($1)DIEEIK	105:108	K($1)FIK	165.88	21.1	7.9	17.7
116-108	113:122	SEFK($1)DIEEIK	106:112	FIK($1)GEIK	158.92	20.6	7.4	19.9
116-125	113:122	SEFK($1)DIEEIK	123:127	TQK($1)VR	120.10	25.5	6.2	17.9
122-102	117:125	DIEEIK($1)TQK	100:103	HEK($1)K	138.15	29.9	9.4	14.2
122-103	117:125	DIEEIK($1)TQK	103:104	K($1)R	217.43	27.7	7.8	18.7
122-105	117:125	DIEEIK($1)TQK	105:108	K($1)FIK	176.43	22.4	8.6	16.3
122-108	117:125	DIEEIK($1)TQK	105:112	KFIK($1)GEIK	187.48	16.3	8.2	8.4
122-112	117:125	DIEEIK($1)TQK	109:116	GEIK($1)SEFK	95.38	17.6	7.0	11.3
125-102	123:127	TQK($1)VR	100:103	HEK($1)K	72.20	19.7	8.9	5.2
125-103	123:127	TQK($1)VR	103:105	K($1)RK	59.61	10.0	7.7	2.8
125-105	123:127	TQK($1)VR	105:108	K($1)FIK	99.57	15.0	7.5	7.0
C-terminal crosslinks								
102-223	100:103	HEK($1)K	222:224	SK($1)K	49.91	4.5	7.2	3.8
103-223	100:104	HEKK($1)R	222:224	SK($1)K	33.66	6.1	8.3	2.4
105-223	104:108	RK($1)FIK	222:224	SK($1)K	126.10	7.1	7.0	3.3
108-221	106:112	FIK($1)GEIK	217-223	YSSGK($1)SK	93.07	17.9	6.1	11.9
108-223	106:112	FIK($1)GEIK	222-224	SK($1)K	104.52	12.4	11.6	7.8
112-221	109:116	GEIK($1)SEFK	217:223	YSSGK($1)SK	81.15	26.5	7.0	16.1
112-223	106:116	FIKGEIK($1)SEFK	222:224	SK($1)K	46.72	4.4	7.3	2.4
116-221	109:122	GEIKSEFK($1)DIEEIK	217:223	YSSGK($1)SK	111.14	13.8	12.1	3.0
116-223	113:122	SEFK($1)DIEEIK	222:224	SK($1)K	84.33	11.5	7.1	10.7
116-224	109:122	GEIKSEFK($1)DIEEIK	222:235	SKK($1)PVGGGHHHHHH	38.72	4.9	5.3	3.9
122-221	117:125	DIEEIK($1)TQK	217:223	YSSGK($1)SK	138.51	27.4	6.1	16.1
122-223	117:125	DIEEIK($1)TQK	222:224	SK($1)K	100.99	29.0	9.6	18.0
125-223	123:127	TQK($1)VR	222:224	SK($1)K	47.77	11.3	8.2	1.9
221-102	217:224	YSSGK($1)SKK	99:103	RHEK($1)K	57.61	15.8	12.4	2
221-103	217:223	YSSGK($1)SK	103:104	K($1)R	82.04	13.2	7.4	6.5
221-105	217:223	YSSGK($1)SK	105:108	K($1)FIK	88.68	14.3	7.6	7.1
221-125	217:223	YSSGK($1)SK	123:127	TQK($1)VR	98.14	26.9	7.0	11.9
224-103	224:235	K($1)PVGGGHHHHHH	103:105	K($1)RK	27.56	13.1	8.2	2.5
224-108	224:235	K($1)PVGGGHHHHHH	106:112	FIK($1)GEIK	25.71	3.3	8.4	3.2
224-112	224:235	K($1)PVGGGHHHHHH	106:116	FIKGEIK($1)SEFK	13.60	5.6	5.3	1.9
224-122	224:235	K($1)PVGGGHHHHHH	117:127	DIEEIK($1)TQKVR	14.72	10.3	5.6	1.9
224-125	224:235	K($1)PVGGGHHHHHH	123-127	TQK($1)VR	8.33	1.5	5.1	2.4
224-221	224:235	K($1)PVGGGHHHHHH	217:223	YSSGK($1)SK	55.07	5.0	6.9	2.1

Extended Data Table 2.6. Mass spectrometry analysis of BS3 crosslinking experiment at pH 6. High-confidence crosslinked peptide pairs selected based on the PP and PPtag scores as well as the number of color tags. Higher PP and PPtag scores indicate better peptide match quality. The cut-off criterion for 'real' matches was set to 2.4 for PP score and 1.3 for PPtag score. Color tags on protein sequence indicate an amino acid residue with a pair of consecutive y ions (green), a pair of consecutive b ions (blue) or with both pairs of consecutive b and y ions (red). Tags provide a direct visual indication of match quality and the higher the number of color tags of a peptide match the better the match. Crosslinked lysines are labeled with a ($1) symbol. For same crosslinks identified in multiple peptide pairs, only the best pair was included in the table. *Experiments by Maciej Jagielnicki, William McIntire, Venkat Dharmarajan, and Patrick R. Griffin.*

Chapter 3
CryoEM structure of a connexin hemichannel

Ali K. Khan[1,*], Maciej Jagielnicki[1,*], Brad C. Bennett[1], and Mark Yeager[1,2,3,4,]

[1] Department of Molecular Physiology and Biological Physics, University of Virginia School of Medicine, Charlottesville, VA 22908 USA. [2] Center for Membrane Biology, University of Virginia School of Medicine, Charlottesville, Virginia 22908, USA. [3] Cardiovascular Research Center, University of Virginia School of Medicine, Charlottesville, Virginia 22908, USA. [4] Department of Medicine, Division of Cardiovascular Medicine, University of Virginia School of Medicine, Charlottesville, Virginia 22908, USA. [*] These authors contributed equally to this work.

Connexins can function as both hexameric hemichannels and dodecameric GJC (33, 34, 68). Hemichannels allow for communication between the cytoplasmic and extracellular space (3, 46) and play a major role in pathological conditions, such as skin disease (56, 59). Thus far, all high-resolution connexin structures have been of the dodecameric GJC, and it is still not well understood if the structural mechanisms of inhibition are conserved between the hemichannels and GJCs. We are particularly interest in how hemichannel maintain their closed state *in vivo*. In this chapter, we describe our

efforts towards reconstructing the first hemichannel structure using single-particle cryoEM.

3.1. Results

3.1.1. *Expression and Purification of Cx26 hemichannels*

The Cx26 X-ray crystal structures revealed that docking between hemichannels is achieved by hydrogen bonding between the extracellular loops of apposing connexons (1, 18). Homology modeling of the Cx32 channel with the Cx26 structure was then used to predict that a Cx32 N175Y mutation in the docking interface of the E2 domain of would disrupt homotypic hemichannel docking. Further patch clamping and dye uptake experiments confirmed that while the Cx32 N175Y mutant failed to show junctional coupling, it can still functional as a hemichannel (65, 66). By engineering the analogous mutation (N176Y) in Cx26, we successfully expressed and purified the hemichannel from *Sf9* insect cells (**Figure 3.1A)**. The SEC purification profile suggests that the Cx26 N176Y mutant has an apparent molecular weight roughly half that of the wild-type (WT) protein (**Figure 3.1B**). The hemichannel sample appeared monodisperse and homogenous on a negative stained electron microscopy (EM) grid (**Figure 3.1C**), making it a suitable candidate for cryoEM.

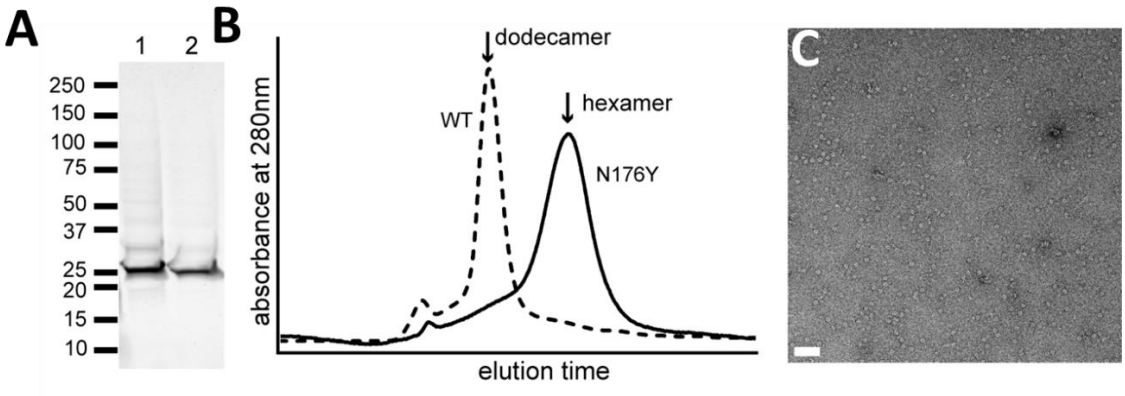

Figure 3.1. Expression and Purification of Cx26 176Y (A) Coomassie-stained SDS PAGE gel showing (1) IMAC-purified protein and (2) SEC-purified protein from a Superdex 200 10/300 column (fractions corresponding to the peak labeled hexamer in (B)). (B) SEC profiles comparing SEC-purified wild type, dodecameric Cx26 channels and N176Y hemichannels, which migrate at a position corresponding to a hexamer. (D) Electron micrograph of SEC-purified, negatively-stained Cx26 N176Y. Magnification = 62,000x. Scale bar denotes 50 nm. *Purification optimized by Maciej Jagielnicki and Brad Bennet*.

3.1.2. *Sample optimization for single-particle cryoEM*

As was performed on the Cx26 GJC (**Chapter 2**), we first exchanged Cx26 N176Y into amphipol A8-35 for EM studies. Negative stain EM micrographs displayed homogenous and monodisperse particles in primarily *en face* views (**Figure 3.2A, B**). 2D class averaging revealed that this construct recapitulated the six-fold symmetry of the Cx26 GJC (**Figure 3.2B**). Unfortunately, the cryoEM images of these particles **(Figure 3.2C)** yielded featureless 2D class averages (**Figure 3.2D**) and required us to further stabilize the protein.

We therefore pursued reconstitution of the hemichannel into nanodiscs. Membrane proteins often show improved activity and thermal stability in a lipid environment (105, 106), and single-particle cryoEM reconstructions of the TRPV1 ion channel displayed improved resolution in nanodiscs (107) compared to amphipol (108). Assuming that the hemichannel has roughly the same dimensions in the membrane plane as the Cx26 GJC, we chose to use the MSP2N2 nanodisc scaffold protein because it forms ~150 Å nanodiscs (106) that are large enough to accommodate the channel along with multiple shells of lipid molecules. For the lipid composition, we decided to use a soybean polar lipid extract because of previously reported success in single-particle cryoEM reconstruction of TRPV1 (107). We successfully reconstituted the hemichannel into nanodiscs (**Figure 3.3**); however, the narrow size difference between reconstituted protein and empty nanodisc resulted in a sample contaminated with empty nanodisc after SEC purification (**Figure 3.3A**). The hemichannel also could not be rebound to IMAC resin post reconstitution, preventing further affinity purification.

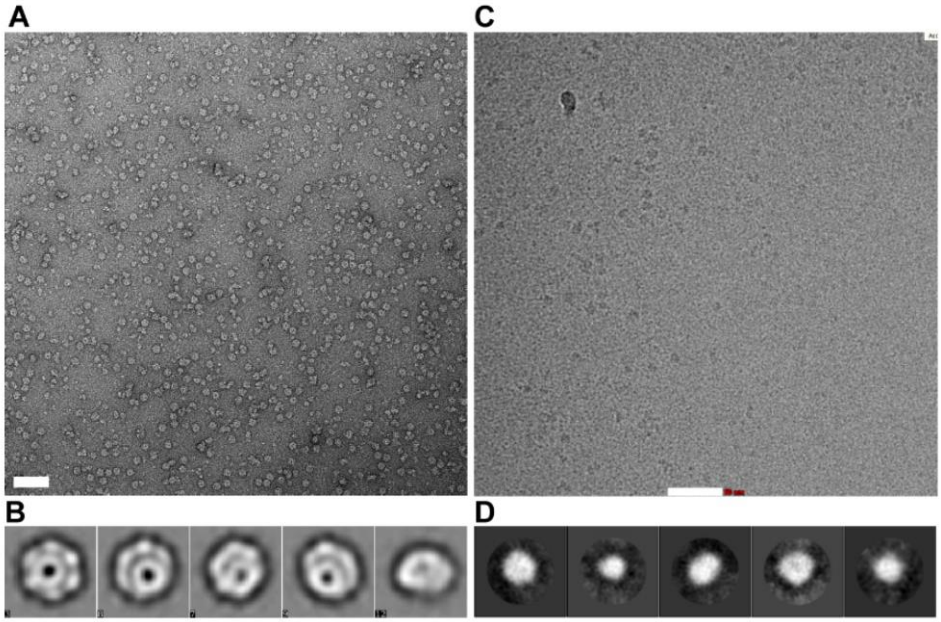

Figure 3.2. Electron microscopy of Cx26 N176Y hemichannel in amphipol A8-35. (A) Electron micrograph of negative stained Cx26 N176Y particles on a copper grid. (B) 2D class averages of *en face* and tilted views from particles shown in (A). (C) CryoEM micrographs of Cx26 N176Y particles recorded on Titan Krios with a Falcon 2 detector. (D) 2D class averages obtained from particles shown in (C). Scale bar denotes 50 nm. *Negative stain EM performed by Maciej Jagielnicki*.

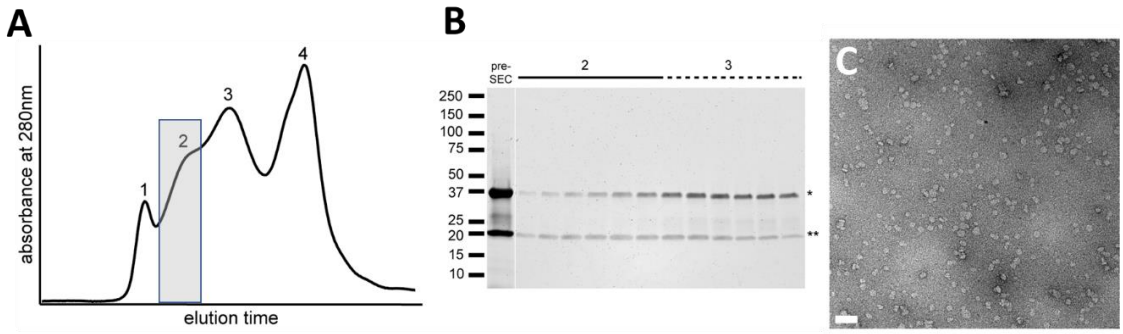

Figure 3.3. Reconstitution of Cx26 N176Y into nanodiscs. (A) SEC profile from the purification of MSP2N2 nanodiscs on Superdex 200 10/300 column. The labeled peaks are: (1) void, (2) nanodiscs with protein, (3) empty nanodiscs, and (4) scaffold protein. (B) Coomassie-stained SDS PAGE gel showing the contents of SEC peaks 1 and 2 showed on (A). The fractions corresponding to peak 2 (shaded in gray on (A)) were pooled and concentrated. Proteins on the gel are: (*) MSP2N2 43 kDa, and (**) Cx26 N176Y 26 kDa. (C) Electron micrograph of SEC-purified, negatively-stained Cx26 N176Y nanodiscs. Magnification = 62,000x. Scale bar denotes 50 nm. *Reconstitution and purification optimized by Maciej Jagielnicki*.

Negative stain EM micrographs of the reconstituted sample (**Figure 3.3C**) showed homogenous and monodisperse particles. We collected cryoEM images of vitrified sample on C-flat holey carbon grids using a 300 kV electron microscope equipped with Falcon II direct electron detector (**Figure 3.4A**). 2D class averages of particles (**Figure 3.4B**) revealed top views of a circular nanodisc with featureless hemichannel protein in the center. The lack of features in the protein is not unexpected. *Henderson et al.* showed that it is significantly more difficult to determine orientations of proteins having molecular weights less than 0.6 MDa during 3D reconstruction (90). Since determination of the particle Euler angles is primarily determined by the low-resolution frequencies in an image, it is crucial for small molecular weight particles such as the Cx26 hemichannel to use a direct electron detector that has a high detector quantum efficiency (DQE) in the low-resolution range. The Gatan K2 and FEI Falcon 3EC cameras are known to have a 50% or greater DQE than that of the Falcon II in the low-resolution frequency domain (109). This allows for better determination of particle orientation and may explain why the class averages lacked molecular features.

We imaged the hemichannel on a 300 kV electron microscope equipped with Gatan K2 direct electron detector (**Figure 3.4C**). Our class averages greatly improved, displaying α-helical features in the *en face* views that resembled the Cx26 GJC (**Extended Data Figure 2.9**). Unfortunately, nearly all the particles preferentially adopted an *en face* or slightly tilted orientation (**Figure 3.4D**), which prevented 3D reconstruction.

We screened a plethora of grid types, additives, and freezing times (**Table 3.1**) to determine conditions in which side views could be observed. The only grid type that

consistently yielded visible side views (**Figure 3.4E, F**) were UltrAuFoil holey gold film grids, which we chemically coated with linear thiol bearing polyethylene glycol (PEG) molecules (**Figure 3.5**). This grid modification was first described by *Subramaniam et al.* to drive partitioning of macromolecules into copper cryoEM grids coated with gold (110). Cx26 hemichannel vitrified on PEG modified of gold grids resulted in both a high monodispersed particle concentration and a broader set of orientations.

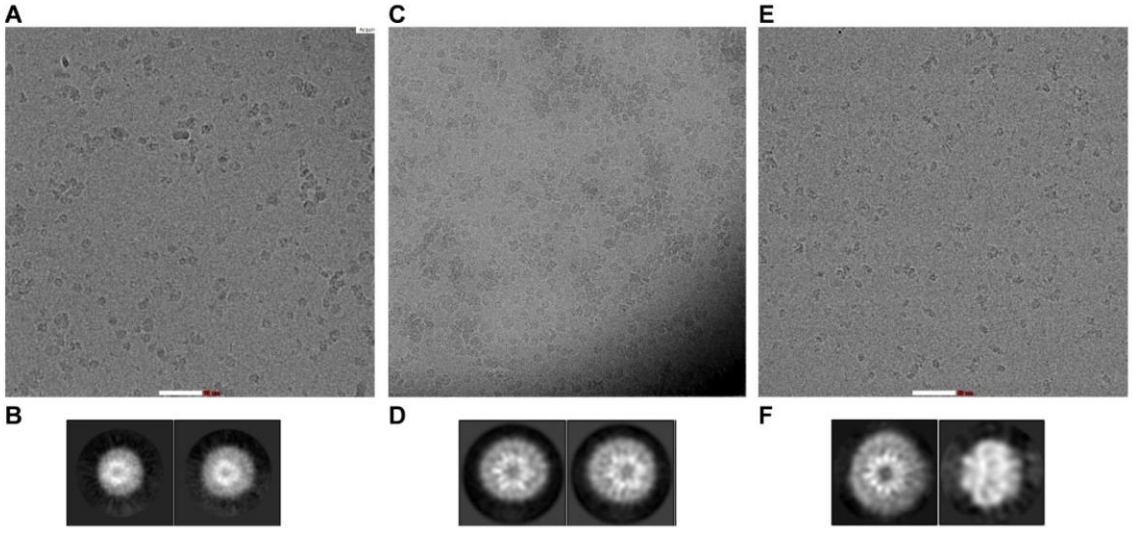

Figure 3.4. Electron microscopy of Cx26 N176Y hemichannel in nanodiscs. (A) Electron cryomicrograph of particles on C-flat holey carbon grids recorded on Titan Krios with a Falcon 2 detector. (B) 2D class averages obtained from particles shown in (A). (C) Electron cryomicrograph of particles on C-flat holey carbon grids recorded on JEOL3200FSC microscope with K2 detector. (D) 2D class averages obtained from particles shown in (C); α-helical secondary structure is evident in *en face* 2D class averages. (E) Electron cryomicrograph of particles on PEGylated UltrAuFoil holey gold grids recorded on Titan Krios with a Falcon 3EC detector. (F) 2D class averages obtained from particles shown in (E) show *en face* and side views displaying α-helical secondary structure. Scale bar denotes 50 nm.

Grid Type	Protein Concentration (mg/mL)	Blot Time (s)	Additive	Result
UltrAuFoil	0.22	7		No particles in the grid and thick ice
UltrAuFoil	0.22	10		Few low contrast particles accompanied with protein aggregation
Graphene Quantifoil 2/2	0.22	5		Densely packed low contrast, blurry particles
Graphene Quantifoil 2/2	0.22	6		Densely packed low contrast, blurry particles
Graphene Quantifoil 2/2	0.22	7		Densely packed low contrast, blurry particles
Graphene Quantifoil 2/2	0.22	8		Densely packed medium contrast particles
Graphene C-flat 2/2	0.22	7		Most of grid has thick black ice with a few particles in thinner ice regions
C-flat 2/2	0.22	6	0.2% OG	No particles in the holes.
C-flat 2/2	0.22	6	0.1 mg/mL SiO2 Beads	Grid is mostly dry holes with few particles in regions containing ice
C-flat 2/2	0.22	7	0.1 mg/mL SiO2 Beads	Grid is mostly dry holes with few particles in regions containing ice
C-flat 2/2	0.22	6	50 nm Viral Tubes	Dry Holes
C-flat 2/2	0.22	7	50 nm Viral Tubes	Dry Holes
C-flat 2/2	0.22	6	Gold Nanoparticles	Sparse low contrast particles and no gold nanoparticles visualized
C-flat 2/2	0.45	3		Holes are mostly dry or have very thick ice
C-flat 2/2	0.45	3		Thinner ice with particles present
C-flat 2/2	0.45	4		Particles with good contrast and mild protein aggregation
Graphene C-flat 1.2/1.3	0.45	3		All squares are broken
Graphene C-flat 1.2/1.3	0.45	3		Most squares are broken and holes have thick ice
C-flat 1.2/1.3	0.23	Manual 3-4	50 nm Viral Tubes	Thick ice with few low contrast particles
C-flat 2/2	0.23	Manual 3-4	50 nm Viral Tubes	All squares are dry or broken
C-flat 2/2	0.23	Manual 3-4	50 nm Viral Tubes	All squares are dry or broken
C-flat 1.2/1.3	0.23	Manual 3-4	0.2% OG	Thick ice with few low contrast particles
C-flat 1.2/1.3	0.23	Manual 3-4	0.1 mg/mL SiO2 Beads	Holes with thick ice containing SiO2 beads and low contrast particles
C-flat 1.2/1.3	0.23	Manual 3-4	0.1 mg/mL SiO2 Beads	Holes with thick ice containing SiO2 beads, low contrast particles, and ethane contamination
C-flat 2/2	0.23	Manual 3-4	0.1 mg/mL SiO2 Beads	Dry Holes
PEGylated UltrAuFoil	0.46	4		Thick ice
PEGylated UltrAuFoil	0.46	6		Low contrast particles with side views
PEGylated UltrAuFoil	0.46	8		Medium contrast particles with side views and strange looking ice
PEGylated UltrAuFoil	0.46	10		Grid is all black

Table 3.1. CryoEM grid screen to obtain Cx26 N176Y side view images. Unless denoted "Manual," grids were vitrified on a Vitrobot.

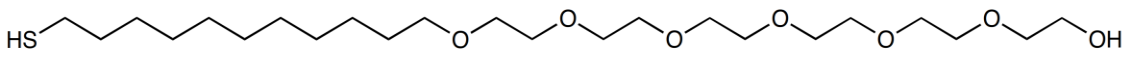

Figure 3.5. Structure of monothiolalkane(C11)PEG6-OH (11-mercaptoundecyl) hexaethyleneglycol used to chemically modify UltrAuFoil grids.

3.1.3. *Comparison of the Cx26 gap junction channel and hemichannel structures in a nanodisc*

We acquired ~2800 images of Cx26 N176Y on PEG UltrAuFoil grids using a 300 kV Titan Krios microscope equipped with a Gatan K2 direct electron detection and energy filter. The particle images yielded 2D class averages of several channel orientations with visible α-helical secondary structure (**Figure 3.6**). Using 37,510 particles, we reconstructed the hemichannel to 4.3 Å resolution (**Figure 3.7** and **Extended Data Figure 3.1**). Local resolution estimation revealed that the hemichannel was most resolved in the transmembrane domains and least resolved in the cytoplasmic and extracellular domains (**Figure 3.8**). This resolution profile deviates from the Cx26 GJC, which was the most resolved in the transmembrane domains and extracellular gap (**Extended Data Figure 2.3 e,f**). Building an atomic model into the density is currently underway; however, analysis of the cryoEM density reveals that we have an open conformation similar to that of the Cx26 GJC (**Figure 3.9**). The hemichannel α-helical transmembrane domain recapitulates the helical conformation of the Cx26 GJC (**Figure 3.9 a,b**). The largest structural differences from the GJC structure are in the extracellular region of the map (**Figure 3.9 c,d**), which appear to take a different conformation. The E2 region also appears to incomplete, missing density for approximately 10 amino acids.

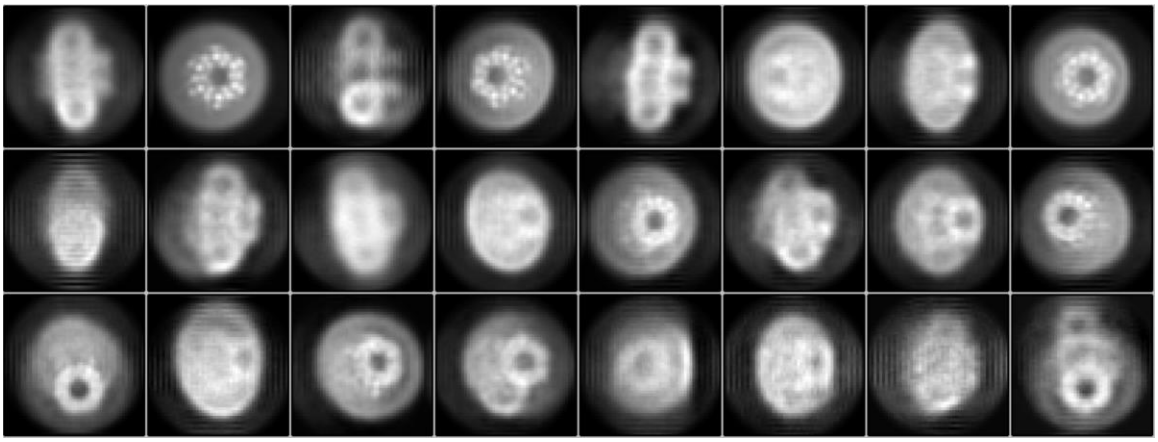

Figure 3.6. 2D class averages of Cx26 N176Y in nanodisc. Class averages are calculated using 3x binned particles (Nyquist limit: 6.4 Å resolution) and display a variety of particle orientations with visible secondary structure.

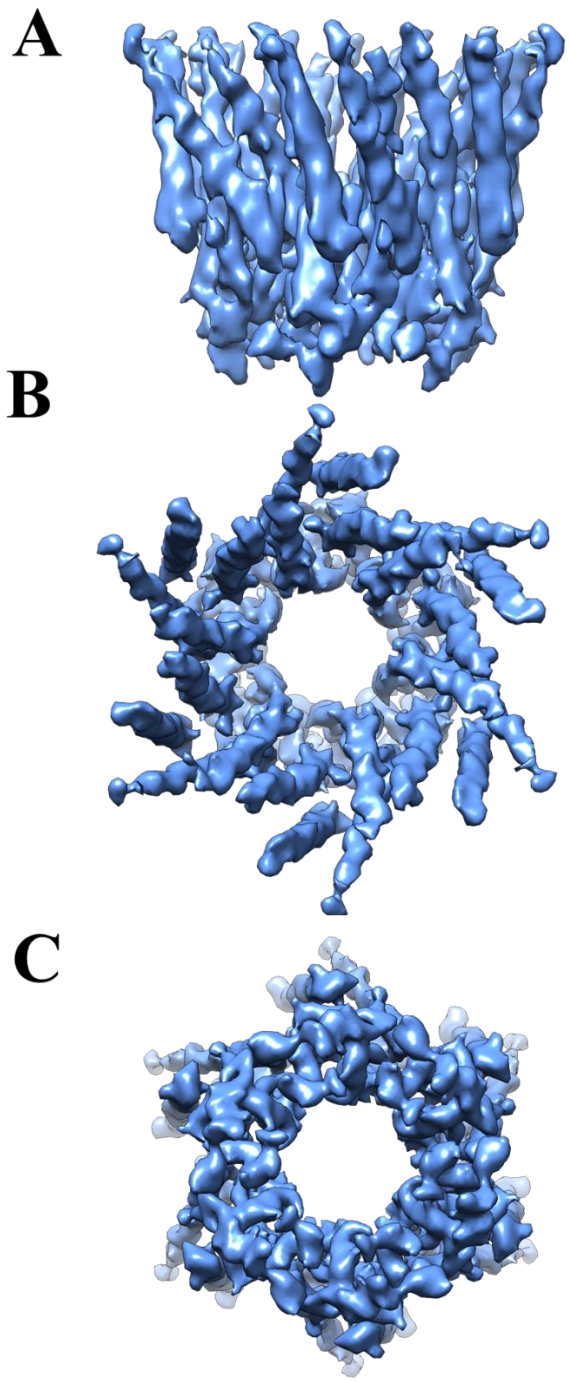

Figure 3.7. CryoEM reconstruction of Cx26 N176Y hemichannel at 4.3 Å resolution. (A) Side view of the hemichannel perpendicular to the membrane plane. (B) Cytoplasmic view of channel parallel to the membrane plane. (C) Extracellular view of channel parallel to the membrane plane. Map is contoured to 4σ.

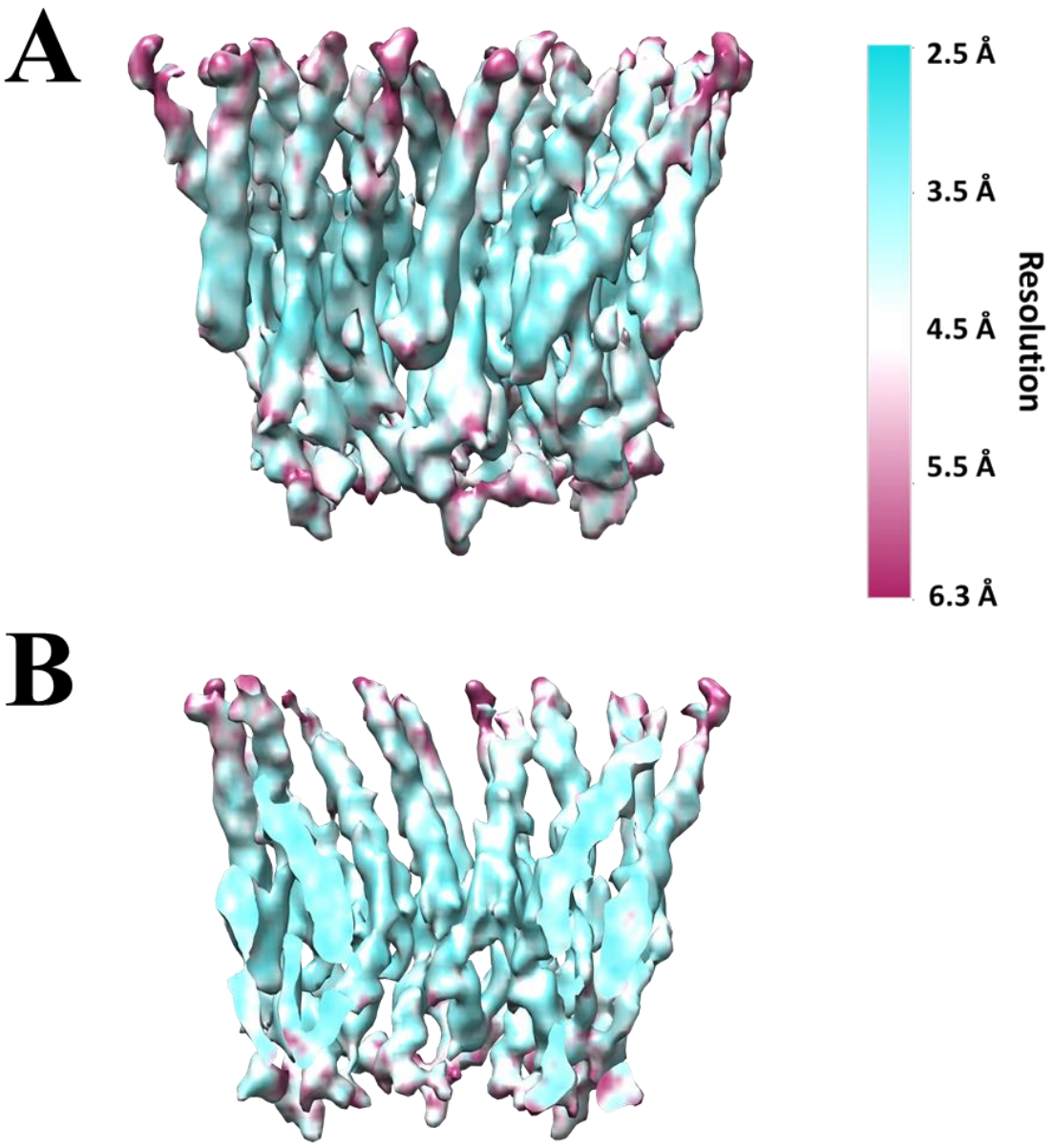

Figure 3.8. Single-particle image processing of the Cx26 GJC at pH 6.4. Map of hemichannel structure (**a**) is shown with a cropped-view (**b**) to display the interior of the channel pore. Map is colored by local resolution calculation by Resmap (104) as depicted by the color bar.

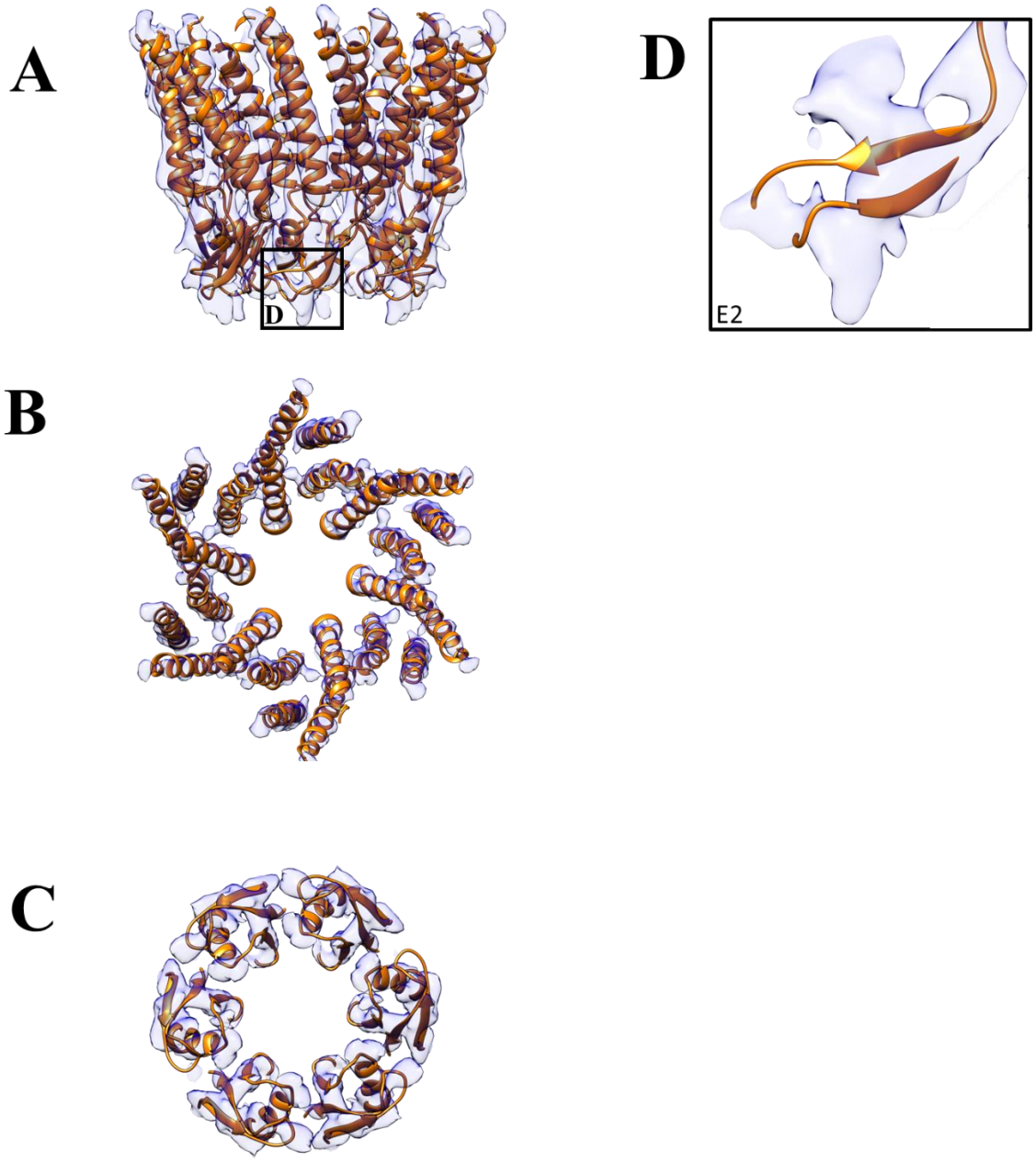

Figure 3.9. Cx26 N176Y resembles open gap junction conformation. Cx26 N176Y cryoEM density map (transparent blue) oriented as a side view (A), cytoplasmic view (B), and extracellular view is rigid body docked with the hemichannel of the Cx26 GJC crystal structure (PDB: 5ERA) (1) (orange). The E2 domain boxed in (A) is shown in (D). M1-M4 roughly adopt the same conformation as the open Cx26 GJC (B). Largest differences between the hemichannel and GJC structure occur in the extracellular domains (C and D). Map is contoured to 4σ.

For comparison, we reconstructed the Cx26 GJC in the same nanodisc composition to 6.5 Å resolution (**Figure 3.10**). This map recapitulated the previous cryoEM and X-ray crystallography structures of the Cx26 GJC at physiological pH (**Figure 3.11**). Unlike the previous cryoEM structure in amphipol, the potential NT helix was not visualized in nanodiscs. Comparing the GJC and hemichannel at their given resolutions, the only differences appears to be in the extracellular region, which is completely resolved in the GJC and not in the hemichannel. Regardless, the channel appears to be in an open conformation in both contexts (**Figure 3.12**).

3.1.3. *3D classification of hemichannel particles reveals variability in the extracellular domains*

Since the extracellular domains in the hemichannel cryoEM maps were incomplete and lower in resolution compared to the TMDs, we performed 3D class averaging on the particles from the hemichannel reconstruction to determine if there was conformational heterogeneity (**Figure 3.13**). To our surprise, 3D class averaging gave us two unique conformational states that refined to lower resolution (**Figure 3.13 B,C**). Though both 3D classes recapitulated the alpha helical conformation of the original cryoEM density, one class shows the extracellular domains in an open channel confirmation (**Figure 3.13 B**), while the other showed density in the extracellular domain blocking the pore (**Figure 3.13 C**). The resolution precludes identification of this extracellular pore density, but the density does connect to the extracellular portion of the channel suggesting that it is formed by the extracellular domains.

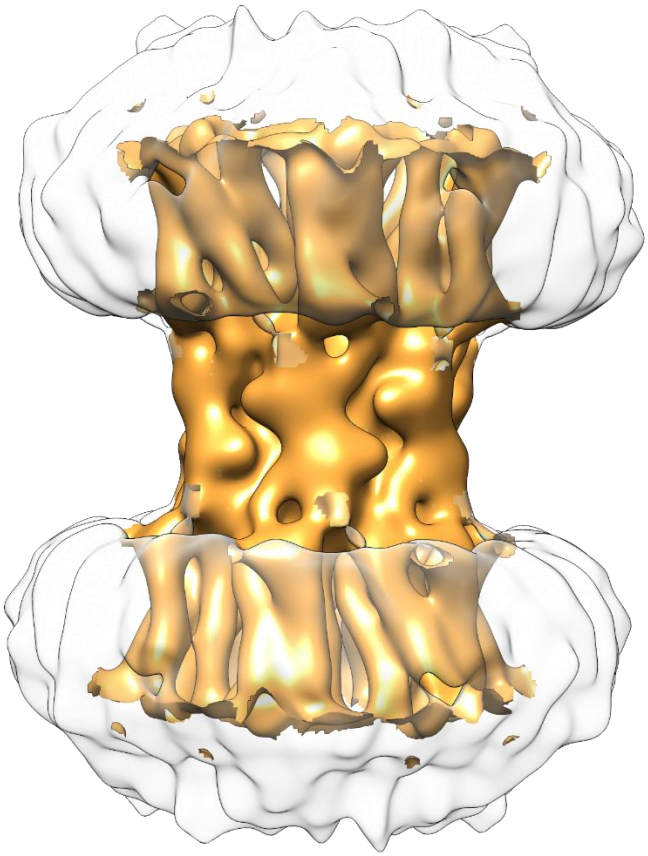

Figure 3.10. CryoEM structure of the human recombinant Cx26 GJC in nanodiscs at 6.5 Å resolution. Side view (parallel to the membrane) of Cx26 cryoEM maps. Nanodisc and unidentifiable low-resolution density is displayed in transparent white so that the GJC (orange) can be easily visualized. Map is contoured to 3σ.

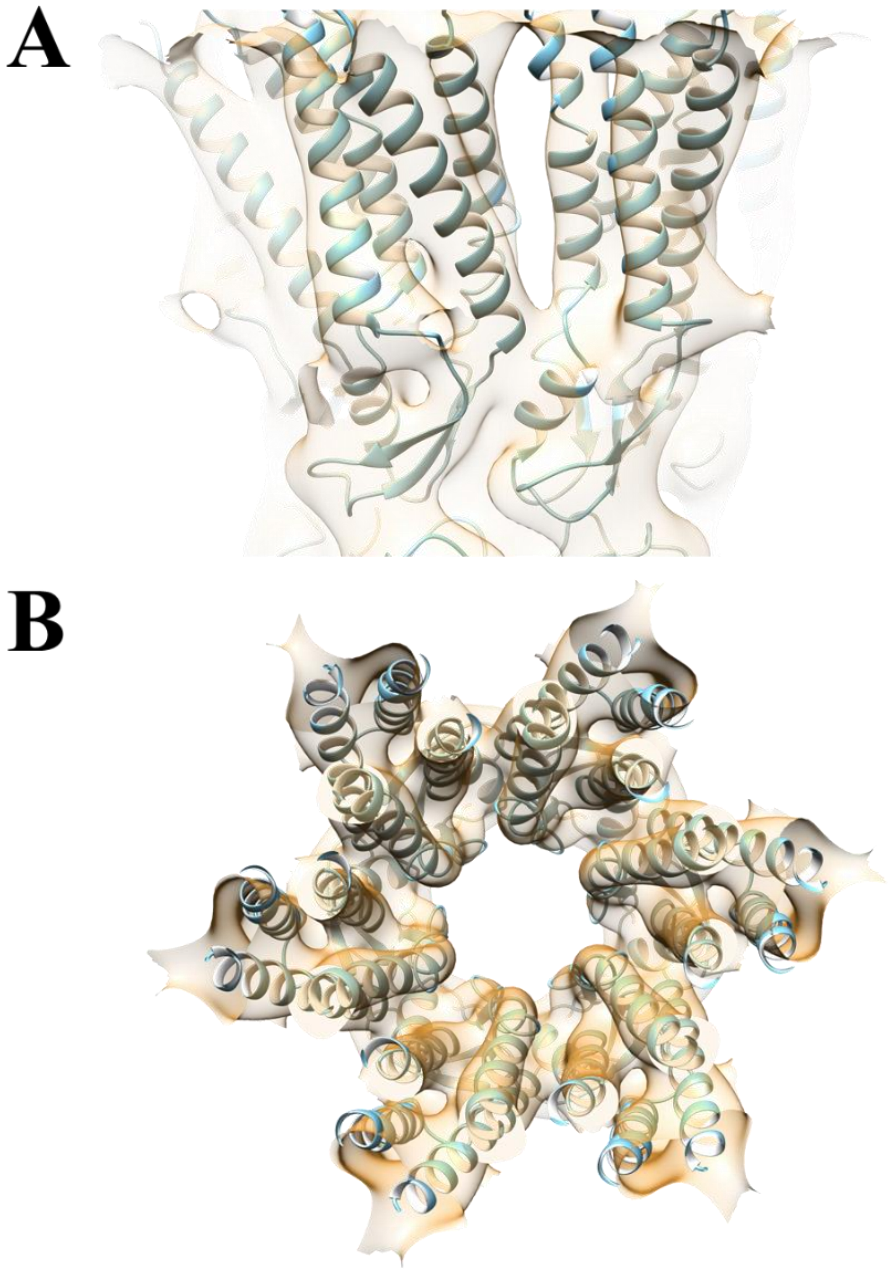

Figure 3.11. CryoEM structure of the Cx26 GJC in nanodisc recapitulates the physiological pH structure in amphipol. Side view (A) and cytoplasmic view (B) of Cx26 GJC in nanodiscs with the physiological pH cryoEM model from Figure 2.2a-d rigid body docked. All domains of the model dock into the density, with the exception of the NT, which could not be visualized in the nanodisc structure. Map is contoured to 3σ.

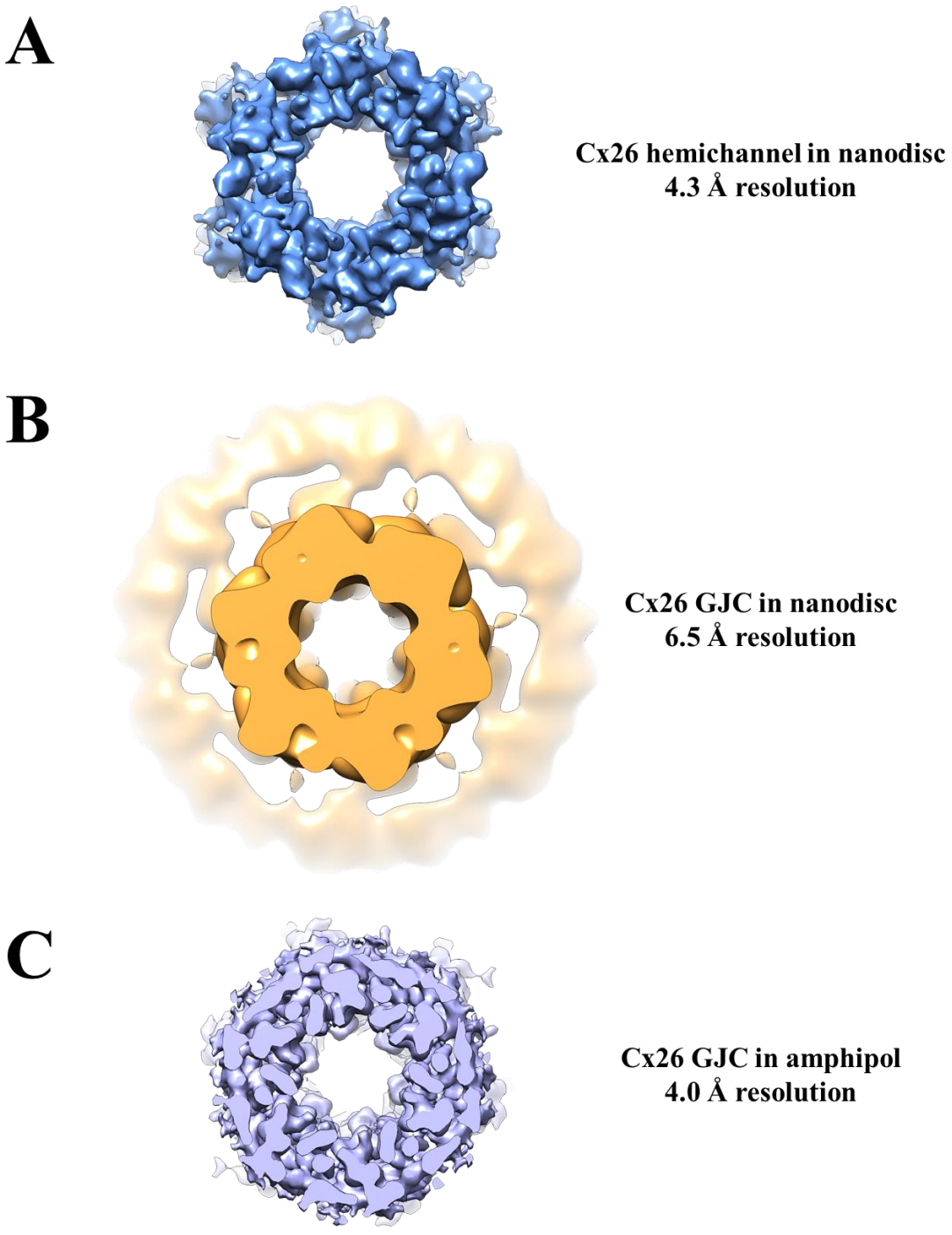

Figure 3.12. Cx26 is in an open conformation as a hemichannel and GJC. The cryoEM structures of the Cx26 N176Y in nanodisc (A), Cx26 GJC in nanodiscs (B), and Cx26 GJC in amphipol (C) are displayed as an end-on view from the extracellular side extending to the transmembrane helices. Like the GJC, Cx26 N176Y pore is in an open state. Maps are contoured to 3σ.

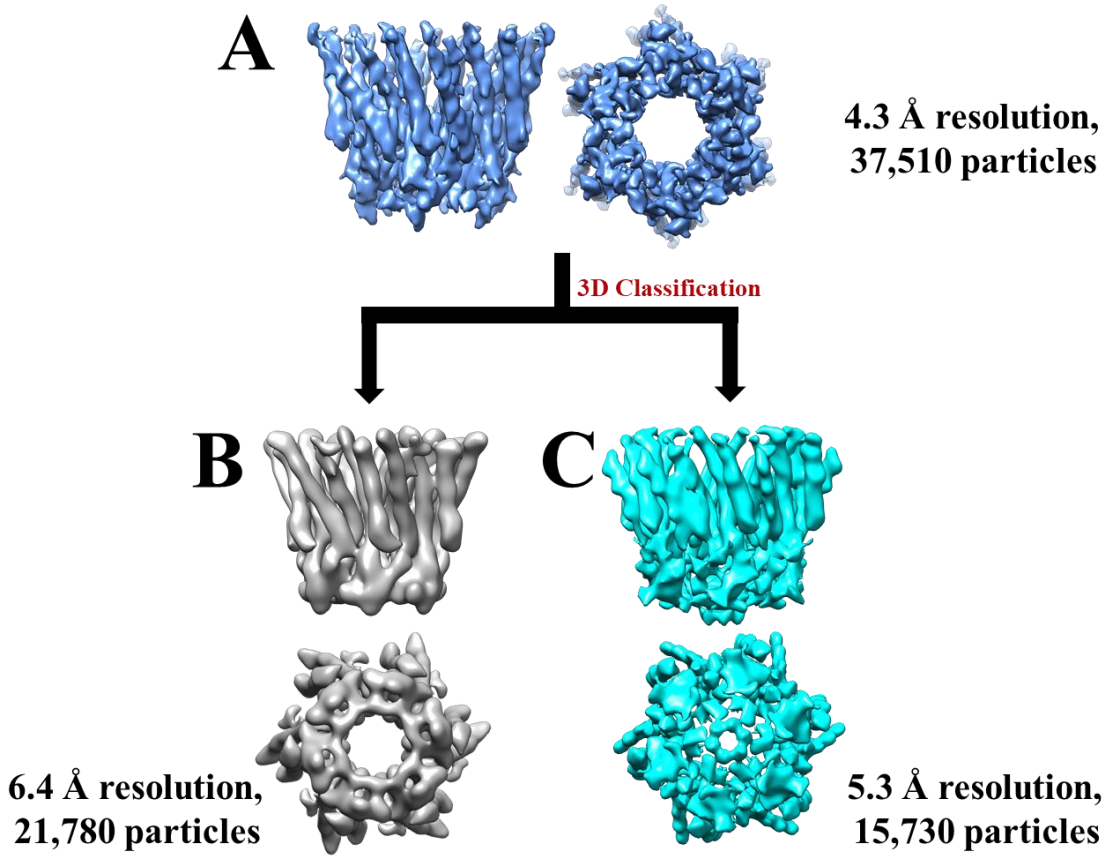

Figure 3.13. 3D Classification reveals variability in the hemichannel extracellular domain. Particles from the 4.3 Å resolution hemichannel map (**A**) where 3D classified revealing two conformations at 6.4 Å resolution (**B**) and 5.3 Å resolution (**C**), respectively. While both classes recapitulated the TMDs of the open hemichannel, one class (**B**) revealed an open channel state, while the other (**C**) had density in the extracellular region blocking the channel pore. Each map is shown as a side view, parallel to the membrane plane, and an extracellular view.

3.2. Discussion

Connexin proteins function both as dodecameric GJCs that allow for cell-to-cell communication and as hexameric hemichannels that allow for communication between the cytoplasm and the extracellular space. In the context of disease, various connexin point mutations are believed to induce a pathological phenotype by abrogating hemichannel activity (59). Thus far, all moderate to high-resolution structures of connexins have been limited to the dodecameric state (1, 13, 14, 16, 18), but hemichannels may be regulated by different structural mechanisms.

In this chapter, we present the first structure of a connexin hemichannel at 4.3 Å resolution. Like previous open GJC structure, the Cx26 N176Y hemichannel is in an open conformation. Rigid body docking of the Cx26 X-ray crystal structure (1) reveals that position of the M1-M4 helices are conserved (**Figure 3.8 A,B**). While the largest deviations from the GJC are in the extracellular domains (**Figure 3.8 C,D**), the pore shape and diameter remain largely unaffected. 3D classification of the particles (**Figure 3.13**) revealed that this open structure likely to have flexible extracellular domains, which can adopt multiple conformations.

Unlike GJCs, hemichannels are believed to be constitutively closed to prevent dysregulation of cellular cytoplasmic contents. Previous AFM studies of Cx26 hemichannels have suggested that this closure is steric, but requires the presence of extracellular Ca^{2+} (36). Our hemichannel structure is consistent with this study. Our hemichannel purification is devoid of Ca^{2+} in all buffers, yet the hemichannel appears to be in an open state. *In vivo*, it is unlikely that the hemichannel defaults to an open state. A

constitutively open hemichannel would preclude the cell from maintaining cytoplasmic homeostasis. In addition, an open hemichannel would lead to leakage of contents from the endoplasmic reticulum and Golgi into the cytoplasmic space during connexin synthesis and membrane trafficking (**Figure 3.14**). Since our results show that the apo-hemichannel maintains an open conformation, an inhibitory signal must be closing the hemichannel *in vivo*. The likely candidate is Ca^{2+} because it is the only gap junction inhibitor present in the endoplasmic reticulum (111), Golgi (112), and extracellular space. The presence of calcium in all of these compartments would allow the hemichannel to main its closed state during membrane trafficking and insertion till it forms the full dodecameric GJC. Upon GJC formation, we hypothesize that the seal formed by GJC extracellular gap would prevent Ca^{2+} in the extracellular space from entering the channel pore, hence resulting in constitutively open junctional channels.

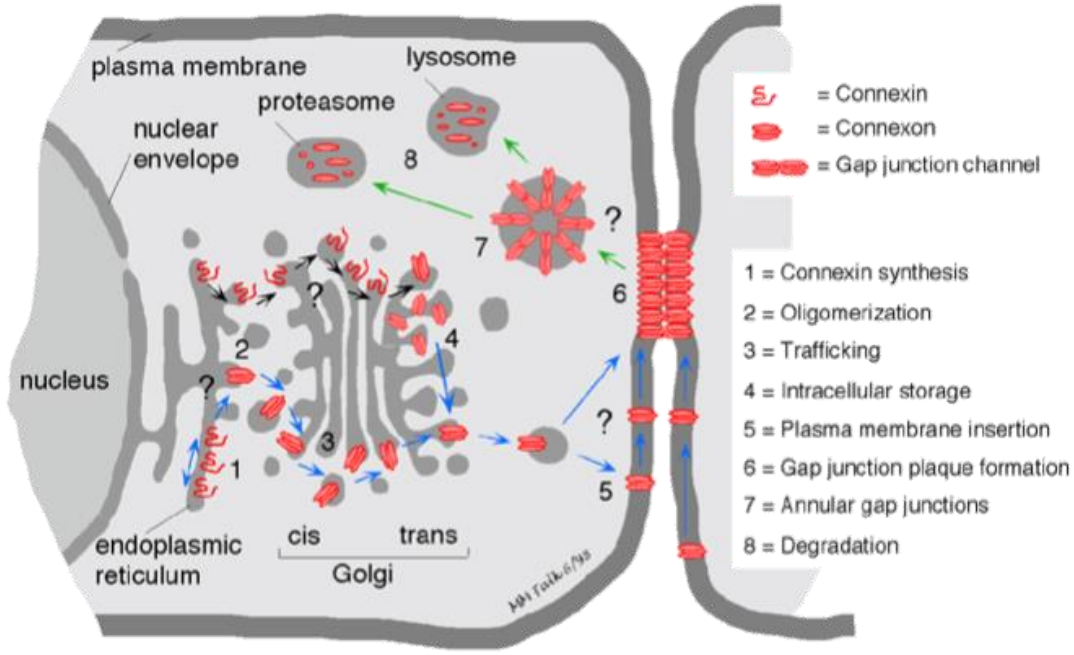

Figure 3.14. Synthesis, assembly, and degradation of gap junction channels. Schematic displays synthesis of monomeric connexin in the endoplasmic reticulum (**1**), oligomerization of connexins into hemichannels (**2**), trafficking of hemichannels to the plasma membrane (**3-5**), formation of gap junction channels (**6**), and internalization (**7**) followed by degradation of junctional channels (**8**). Figure is from (32).

3.3 Methods

Expression and Purification of Cx26 N176Y

Protein expression and purification were performed as described in (1). Samples for EM experiments were eluted from the IMAC column using buffer with 25 mM Tris pH 7.5, 500 mM NaCl, 2.5 % glycerol (v/v), 0.025% façade-EM (FA-3). The final eluate from the SEC column was concentrated to 2 – 4 mg/ml using a 0.5 ml or 4 ml concentrator (100 kDa MWCO; Millipore). If protein was not used for experiments shortly after the purification, it was aliquoted into 0.6 ml tubes, flash-frozen and stored at -80 ^{o}C.

Cx26 N176Y amphipol exchange

Protein sample at 4 mg/ml was mixed with amphipol A8-35 (10 mg/ml stock in 25 mM Tris pH 7.5, 500 mM NaCl, 0.025% façade-EM (FA-3)) at a ratio of 1:3 (w/w), diluting protein to ~1.8 mg/ml. The sample was incubated for 4 h at 4 ^{o}C with gentle mixing. Detergent was removed with Bio-Beads SM-2 (BioRad) by addition of beads to 30mg/ml to protein/detergent/amphipol mixture and overnight incubation at 4 ^{o}C with gentle mixing. Bio-beads were then removed by passing solution through a 0.5 ml disposable fritted column, and eluent was centrifuged for 10 min at 16, 000 x g at 4^{o}C to remove aggregated protein.

Purification of MSP2N2

The plasmid for the membrane scaffold protein construct was obtained from Addgene, Cambridge, MA. E. coli strain BL21(DE3) competent cells were transformed with the MSP2N2 plasmid and protein expressed and purified as described in (113). Since

the protein was only found in the soluble fraction after cell lysis (no inclusion bodies have formed), only the part of the purification protocol describing purification of soluble protein was followed. At the end of the purification, TEV-cleaved (protease purified in-house) MSP2N2 protein was concentrated to ~ 2 mg/ml, aliquoted into 100 µl portions in 0.6 ml tubes, flash frozen in liquid N2 and stored at –80 ^{o}C.

Reconstitution of Cx26 N176Y into Nanodiscs

Lipid stock at 7.5 mg/ml (~10 mM) was prepared (Soybean polar lipids, Avanti, Miami, FL). An aliquot of lipid at 25 mg/ml in CHCl3 was transferred into a brown glass vial, dried under argon gas and solubilized in buffer (25 mM Tris pH 7.5, 150 mM NaCl, 2% n-Octyl-β-D-Glucopyranoside (OG) (w/v)) by vigorous mixing. Purified Cx26 GJC or Cx26 N176Y hemichannel was mixed with nanodisc scaffold protein MSP2N2 and soybean polar lipid extract at a 1:1.5:112 ratio of Cx26 monomer, MSP2N2, and lipid, respectively. Solution was incubated at 4 ^{o}C for 1 h on a nutator or rocker. Bio-beads SM-2 (BioRad) were added to the solution to a concentration of 10 mg/mL, and solution was incubated at 4 ^{o}C for 1 h on a nutator or rocker. A second batch of Bio-Beads SM-2 was added to make a final concentration of 30 mg/mL, and solution was incubated overnight at 4 ^{o}C. Bio-beads were then removed by passing the solution through a 0.5 ml fritted column, eluent spun down for 10min at 16, 000 x g at 4^{o}C and purified further on a Superdex 200 10/300 column in buffer composed of 25 mM Tris pH 7.5, 150 mM NaCl. The peak corresponding to the Cx26 (**Figure 3.3A**) was collected and concentrated in a 100 kDa molecular weight cut-off centrifugal concentrator till the absorbance of the solution at 280 nm reached 0.4 – 0.6.

Negative stain EM analysis

For EM of negatively stained samples, a protein sample was applied on a glow-discharged, carbon-coated copper grid, which was next stained with 2 % uranyl acetate. EM was performed using a Tecnai G2 F20 electron microscope (FEI, Hillsboro, OR) equipped with a field-emission electron source, operating at 120 keV. Low electron dose images (~15 $e^-/Å^2$) were recorded on a 4K x 4K pixel CCD camera (Gatan, Pleasanton, CA) at 62,000 x magnification (corresponding to 1.8 Å / pixel) with a 1 sec exposure time at an underfocus value of ~1.5 µm. Image processing was performed using EMAN v2.05 software (82).

Preparation of Pegylated UltrAuFoil Grids

UltrAuFoil grids (Quantifoil Micro Tools) were glow discharged at 20 mA for 60 s. Each grid was placed in individual 600 µL eppendorf tubes containing 100µL of 5 mM 11-mercaptoundecyl hexaethyleneglycol (SPT-0011P6, SensoPath Technologies) in 200 proof ethanol (EtOH) (110). Reagent and grid mixing was performed in a large styrofoam box with a steady stream of argon gas blowing over it. Each tube is then flushed with argon and sealed with parafilm. Eppendorf tubes were place in a 50 mL conical tube, which was then flushed with argon, capped, and sealed with parafilm. Grids were incubated at room temperature for 24 h protected from light. After incubation, grids were removed from eppendorf tubes. Each grid was dunked three times in a 2 mL eppendorf tube containing EtOH and blotted from the side with filter paper after each dunk to remove the EtOH. Grids were air dried for 1-2 minutes and stored in a desiccator till we were ready to freeze our sample. Sample was vitrified on the grids within the same day.

CryoEM Sample Preparation of Cx26 N176Y in Amphipol

For protein samples in amphipol, purified Cx26 N176Y (~2 mg/mL in 25 mM Tris pH 7.5, 500 mM NaCl, amphipol (A8-35)) was diluted to 0.4 mg/mL with a final buffer concentration of 25 mM Tris pH 7.5, 200 mM NaCl. 3.5 µL of sample was then immediately applied to a glow-discharged (with amylamine) C-flat holey carbon grid (1.2 µM/1.3 µM or 2 µM/2 µM hole size/hole space), blotted with Whatman no. 1 filter paper using a Vitrobot (FEI company) using 4 s blotting time, blot force of 3, and 100 % humidity at 22^{o}C, and then plunge-frozen in liquid ethane cooled by liquid nitrogen.

CryoEM Sample Preparation of the Cx26 N176Y Hemichannel in Nanodisc.

3.5 µL of purified Cx26 N176Y reconstituted into nanodiscs was applied to applied to a glow-discharged (with amylamine) C-flat holey carbon grid (1.2 µM/1.3 µM or 2 µM/2 µM hole size/hole space) or a pegylated UltrAuFoil grids (1.2 µM/1.3 µM hole size/hole space). For C-flat grids, sample was blotted with Whatman no. 1 filter paper using a Vitrobot (FEI company) (4 s blotting time, blot force of 3, and 100 % humidity at 22^{o}C) and then plunge-frozen in liquid ethane cooled by liquid nitrogen. Samples on pegylated gold grids were blotted with Vitrobot filter paper (Electron Microscopy Sciences) using a Vitrobot (7 s – 8 s blotting time, blot force of 5, and 100 % humidity at 4 ^{o}C), and then plunge-frozen in liquid ethane cooled by liquid nitrogen.

CryoEM Sample Preparation of the Cx26 GJC in Nanodisc

3.5 µL of purified Cx26 GJC reconstituted into nanodiscs was applied to applied to a glow-discharged (with amylamine) C-flat holey carbon grid (1.2 µM/1.3 µM hole size/hole space) Sample was blotted with Whatman no. 1 filter paper using a Vitrobot (FEI company) using 4 s blotting time, blot force of 3, and 100 % humidity at 22^{o}C, and then plunge-frozen in liquid ethane cooled by liquid nitrogen.

CryoEM Data Acquisition of the Cx26 N176Y Hemichannel in Nanodisc

Images of the Cx26 N176Y hemichannel frozen on C-flat grids were collected were collected at the National Center for Macromolecular Imaging (NCMI) at the Baylor College of Medicine (Houston, Texas) on a JEOL3200FSC cryo-electron microscope, operated at 300 kV, equipped with GIF Quantum Energy Filter operated in zero-energy-loss mode with a slit-width of 30 eV and a K2 Summit direct electron detector (Gatan, Inc.). Images were collected using an automated procedure in Serial EM (114) at a magnification corresponding to a 1.23 Å physical pixel size. Images were recorded in super resolution mode (0.615 Å super resolution pixel size) as a 50-frame movie with an exposure time and dose rate of 10 s and 5.0 e Å^{-1} s^{-1} (total dose 50 e Å^{-1}), respectively.

For grid screening, images were collected were collected at the UVa Molecular Electron Microscopy Core (MEMC) (Charlottesville, Virginia) on a Titan Krios cryo-electron microscope, operated at 300 kV, equipped with a Falcon 3ec direct electron detector (Thermo Fisher Scientific).

Images of the Cx26 N176Y hemichannel frozen on PEG UltrAuFoil grids were collected at the European Synchrotron Radiation Facility (ESRF) (Grenoble, France) on a

Titan Krios cryo-electron microscope, operated at 300 kV, equipped with GIF Quantum Energy Filter operated in zero-energy-loss mode with a slit-width of 20 eV and a K2 Summit direct electron detector (Gatan, Inc.). Images were collected using an automated procedure in EPU (Thermo Fisher Scientific) at a magnification corresponding to a 1.067 Å physical pixel size. Images were recorded in electron counting mode as a 40-frame movie with an exposure time and dose rate of 8 s and 5.25 e $Å^{-2}$ s^{-1} (total dose 42 e $Å^{-2}$), respectively. Defocus range set in EPU was -1.3 μm to - 2.5 μm in 300 nm increments.

CryoEM Data Acquisition of the Cx26 GJC in Nanodiscs

Images of the Cx26 GJC in nanodiscs were collected were collected at the UVa Molecular Electron Microscopy Core (MEMC) (Charlottesville, Virginia) on a Titan Krios cryo-electron microscope, operated at 300 kV, equipped with a Falcon 3ec direct electron detector (Thermo Fisher Scientific). Images were collected using an automated procedure in EPU (Thermo Fisher Scientific) at a magnification corresponding to a 0.85 Å physical pixel size. Images were recorded in electron counting mode as 1872-frame movie equally distributed into 78 fractions with an exposure time of 48.17 s. Total dose of each movie ranged from 40 – 60 e $Å^{-2}$.

CryoEM Data Processing of the Cx26 N176Y Hemichannel in Nanodisc

For data collected on C-flat grids, all movie frames were motion-corrected and integrated using Motioncor2 (115) in a 5 by 5 patch and grouping frames by 3. The contrast transfer function (CTF) was estimated on each integrated image using GCTF (88). In

RELION v2 (85-87), two-dimensional (2D) class averages calculated from 30,000 manually picked particles.

For data collected on PEG UltrAuFoil grids, all movie frames were motion-corrected and integrated in SCIPION (116) using Motioncor2 (115) in a 5 by 5 patch. The contrast transfer function (CTF) was estimated on each integrated image using Gctf (88). Using a single side-view 2D class average, template-based particle picking as implemented in RELION v2.1 (85-87) was used to pick particles on motion-corrected images. 2D and 3D class averaging was performed in cryoSPARC (117). The initial model for 3D class averaging was a 30 Å low-pass filtered hemichannel PDB model from the Cx26 cryoEM structure (**Figure 2.2a-d**). Refinement with C6 symmetry was performed in RELION v2.1 (85-87) using a 3D class average low-pass filtered to 15 Å, resulting in a 4.9 Å resolution map that improved to 4.3 Å upon post-processing (**Extended Data Figure 3.1**). Distribution of particle Euler angles are shown in **Extended Data Figure 3.2**.

CryoEM Data Processing of the Cx26 GJC in Nanodisc

All movie fractions were motion-corrected and integrated using Motioncor2 (115) in a 5 by 5 patch and grouping by 7. The contrast transfer function (CTF) was estimated on each integrated image using GCTF (88). Particles were picked using the template-based automated picking procedure in RELION v2.1 using 2D class averages generated from manually picked particles. Particles were subjected to 3D classification followed by 3D refinement in cryoSparc (117) to generate a 6.5 Å resolution map. Resolution is estimated using the gold-standard Fourier Shell Correlation (FSC).

3.4. Extended data figures and tables

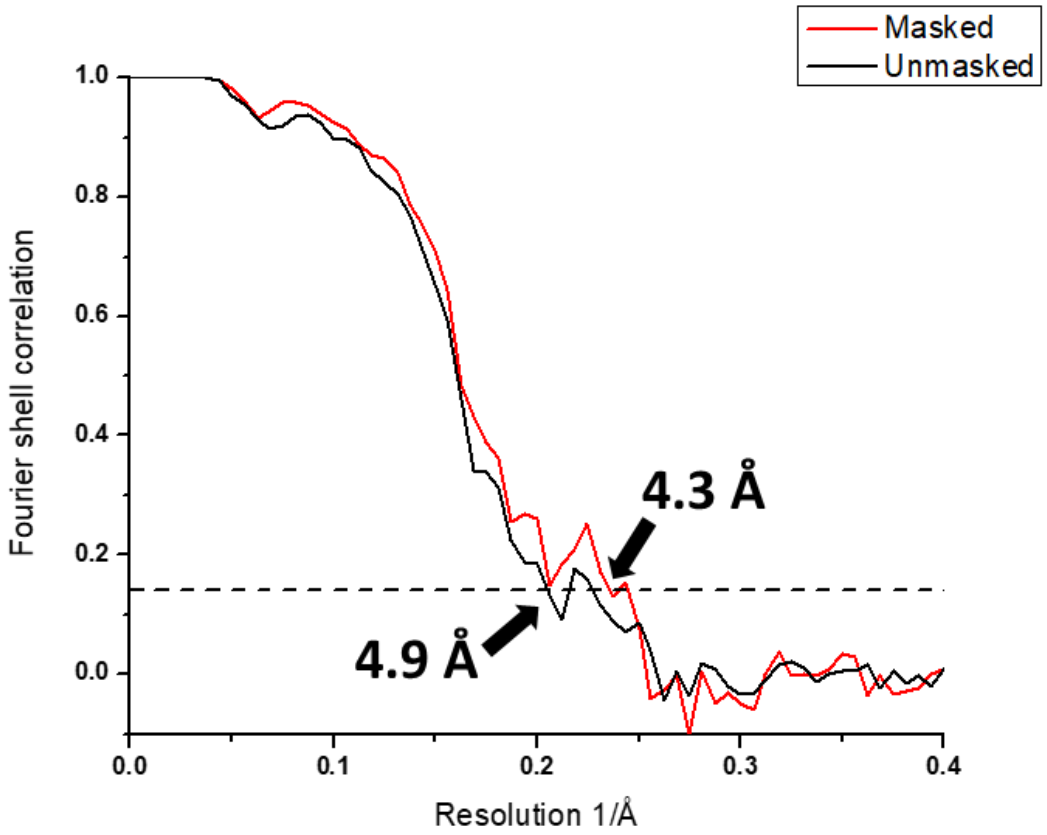

Extended Data Figure 3.1. Gold-standard Fourier Shell Correlation (FSC) shows the global resolution of the hemichannel cryoEM map before and after masking performed in post-processing to be 4.9 Å and 4.3 Å, respectively.

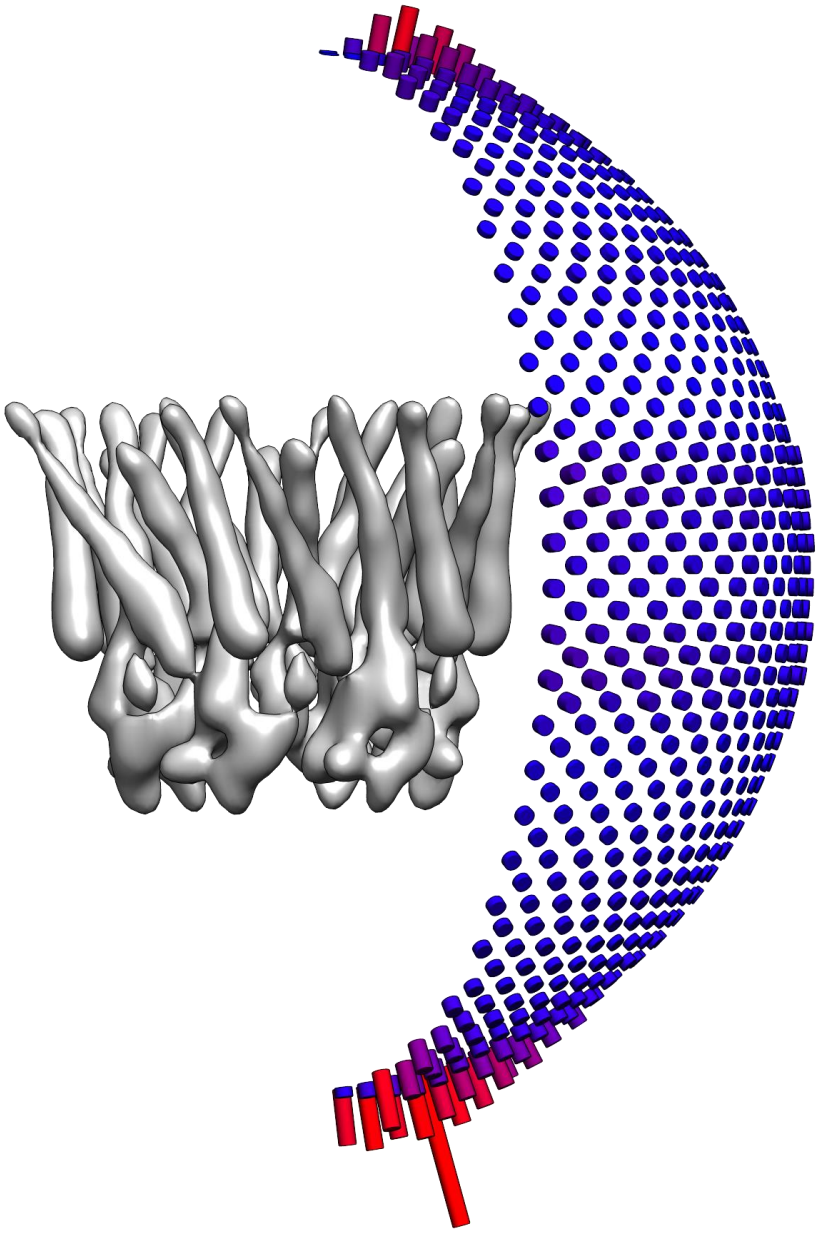

Extended Data Figure 3.2. Euler angle distribution of hemichannel particles depicted as relative cylinder heights. Shortest to longest heights are colored from blue to purple to red.

Chapter 4
Expression, purification, and stabilization of the Cx32 gap junction channel

Ali K. Khan[1], Sandra Poulos[1], Brad C. Bennett[1], and Mark Yeager[1,2,3,4,]

[1] Department of Molecular Physiology and Biological Physics, University of Virginia School of Medicine, Charlottesville, VA 22908 USA. [2] Center for Membrane Biology, University of Virginia School of Medicine, Charlottesville, Virginia 22908, USA. [3] Cardiovascular Research Center, University of Virginia School of Medicine, Charlottesville, Virginia 22908, USA. [4] Department of Medicine, Division of Cardiovascular Medicine, University of Virginia School of Medicine, Charlottesville, Virginia 22908, USA.

A high-resolution structural model of the Cx32 GJC would help elucidate structural changes associated with Cx32 CMT mutations (**Figure 1.14**). This model can provide a basis of comparison for future structures of Cx32 CMT disease mutation constructs and can also be used as a starting model for molecular dynamics (MD) simulation of disease mutants. This chapter describes our efforts towards expression, purification, and stabilization of the Cx32 GJC channel for high-resolution structure determination by either cryoEM.

4.1. Results

We expressed and purified recombinant human Cx32 with a C-terminal truncation at residue 250 (d250) (**Figure 4.1A, B**) from *Sf9* insect cells. Secondary structure

prediction algorithms (118) show the truncated region to be disordered (**Figure 4.2**). In addition, a similar Cx32 construct with a C-terminal truncation at residue 247 has been previously purified for NMR studies (119) and shows no changes to expression or voltage-dependence (120). Negatively-stained EM images of the purified protein in FA-3 detergent (121, 122) show monodispersed and homogeneous particles (**Figure 4.3C**) in both *en face* and side view orientations similar to the Cx26 GJC (**Extended Data Figure 2.2A**).

For cryoEM studies, we exchanged the channel into a nanodisc (**Figure 4.4**) and amphipol A8-35 (**Figure 4.5**) membrane mimetic. While detergent does not prohibit structure determination by single-particle cryoEM, the excess FA-3 required to achieve the critical micelle concentration (CMC) decreases particle contrast. Also, the Cx26 GJC and hemichannel from previous cryoEM studies have shown increased stability in both amphipol (**Extended Data Figure 2.1**) and nanodisc (**Figure 3.4**). In nanodisc, we observed monodispersed and homogenous particles on negatively stained EM grids (**Figure 4.4C**). Particles appeared to be oriented in predominately *en face*, though 10 or fewer side view orientations could be observed in each micrograph. Unfortunately, we were unable to concentrate the channel in nanodisc to more than 0.2 mg/mL, as opposed to FA-3 detergent in which Cx32 d250 could be concentrated to ~1 mg/mL. Even at a concentration of 0.2 mg/mL, cryoEM images displayed predominately aggregated protein and empty nanodisc contamination (**Figure 4.6**). In amphipol, the SEC purification trace (**Figure 4.5A**) resembled that of the channel in FA-3 detergent (**Figure 4.3A**). Unfortunately, the protein appeared to be heterogenous and aggregated when visualized by

negative stain EM (**Figure 4.5B**), and like the nanodisc sample, could not be concentrated to more than 0.2 mg/mL.

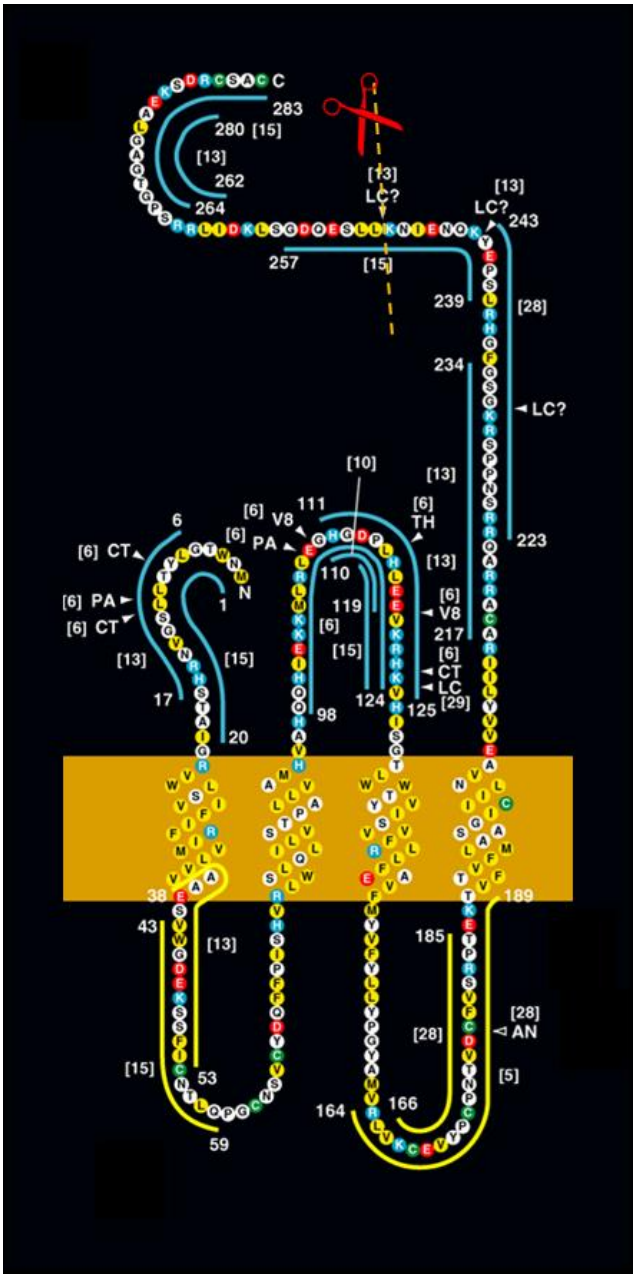

Figure 4.1. Cx32 topology model indicating site of d250 truncation. Site of C-terminal truncation at residue 250 is indicated with a dotted line and red scissors. Figure has been adapted from (10).

MNWTGLYTLLSGVNRHSTAIGRVWLSVIFIFRIMVLV
---HHHHHHHHHH------HHHHHHHHHHHHHHHHHH

VAAESVWGDEKSSFICNTLQPGCNSVCYDQFFPISHV
HH----------EEE--------------------

RLWSLQLILVSTPALLVAMHVAHQQHIEKKMLRLEGH
HHHHHHHHHHHHHHHHHHHHHHHHHHHHHHHHHHHH-

GDPLHLEEVKRHKVHISGTLWWTYVISVVFRLLFEAV
------------------HHHHHHHHHHHHHHHHHH

FMYVFYLLYPGYAMVRLVKCDVYPCPNTVDCFVSRPT
HHHHHHH---------EEEE---------EEEE----

EKTVFTVFMLAASGIRIILNVAEVVYLIIRACARRAQ
HHHHHHHHHHHHHHHHHHHHHHHHHHHHHHHHHHHHH

RRSNPPSRKGSGFGHRLSPEYKQNEINKLLSEQDGSL

KDILRRSPGTGAGLAEKSDRCSAC

Figure 4.2. Secondary structure prediction of Cx32. The amino acid sequence of Cx32 is shown in bold text with corresponding secondary structure prediction result underneath. α-helical, β-sheet, and unstructured residues are marked as H, E, and -, respectively. Notice that the CT is largely unstructured. Secondary structure prediction was performed on the JPred4 online server (118).

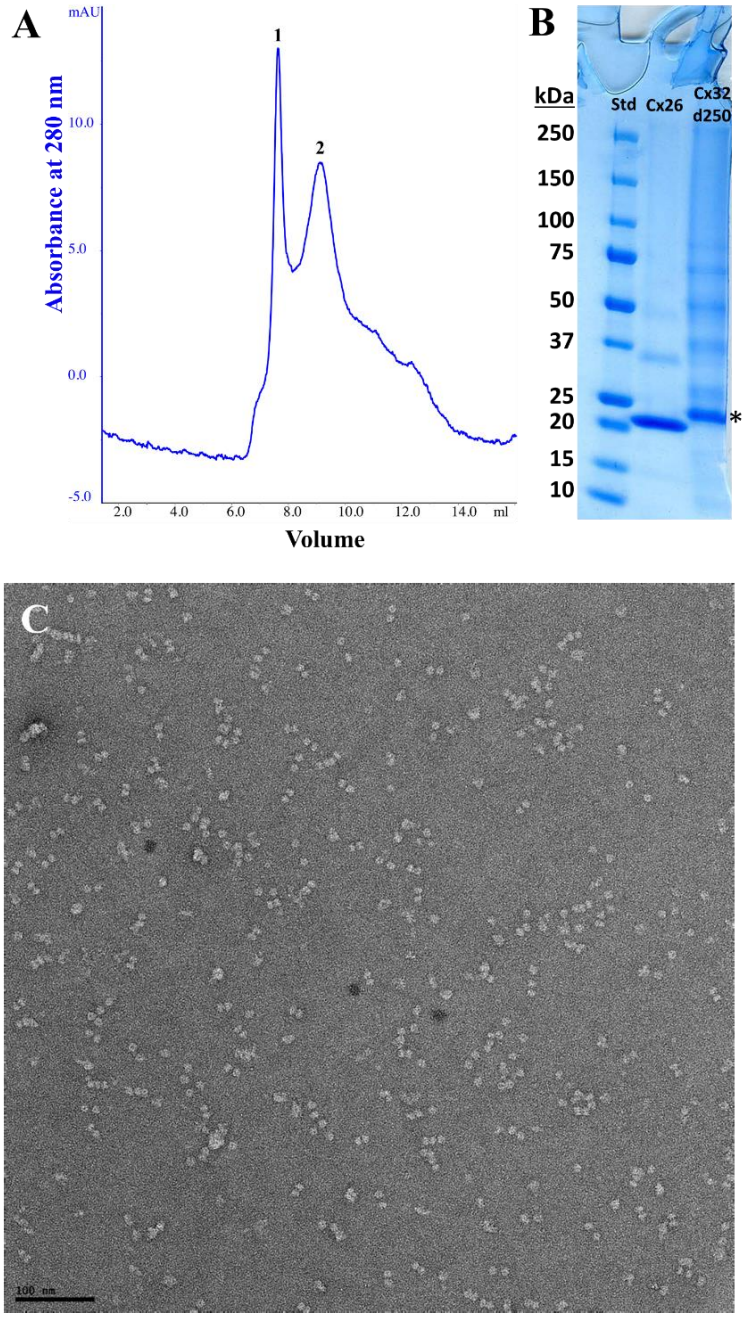

Figure 4.3. Expression and Purification of Cx32 d250. (A) An SEC profile from the purification of Cx32 d250 on Superdex 200 10/300 column. Peaks are labeled: (1) void, (2) Cx32 d250. (B) Coomassie-stained SDS PAGE gel showing (*) Cx32 d250 (29.6 kDa) after SEC purification with molecular weight standards (Std.) and Cx26 (26 kDa) for comparison. (C) Electron micrograph of negatively-stained Cx32 d250 corresponding to apex fraction of peak 2 shown in (A). Scale bar denotes 100 nm. *Purification optimized by Brad Bennett.*

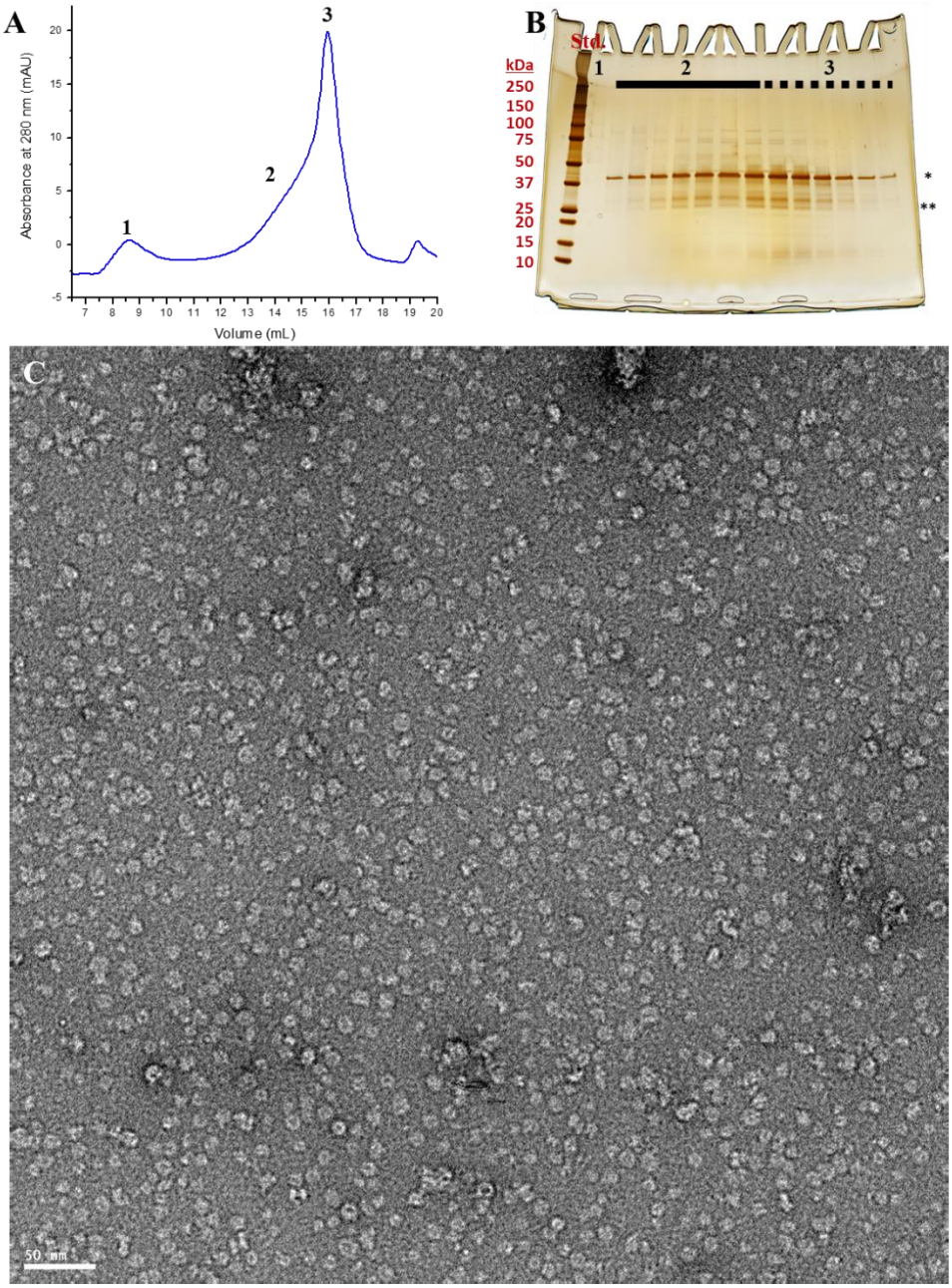

Figure 4.4. Purification of Cx32 d250 in nanodiscs. (A) An SEC profile from the purification of Cx32 d250 after nanodisc reconstitution on Superose 6 Increase 10/300 column. Peaks are labeled: (1) void, (2) Cx32 d250 in nanodisc, and (3) empty nanodisc. (B) Silver-stained SDS PAGE gel of fractions from SEC purification in (A) showing (*) MSP2N2 nanodisc scaffold protein (43 kDa) and (**) Cx32 d250 (29.6 kDa) with molecular weight standards (Std.). (C) Electron micrograph of negatively-stained Cx32 d250 corresponding to peak 2 shown in (A). Particles are predominately *en face* views. Scale bar denotes 50 nm. *Purification optimized by Sandra Poulos.*

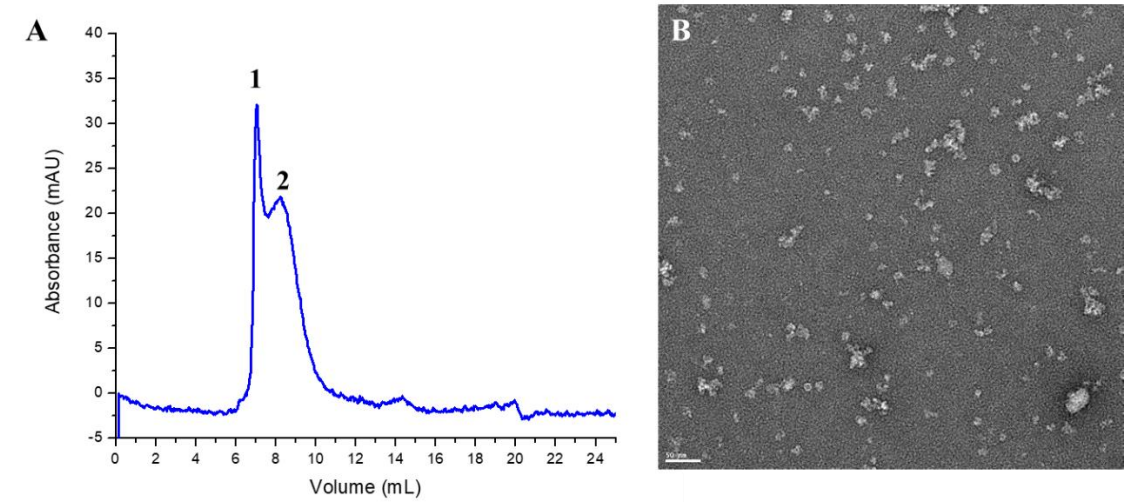

Figure 4.5. Purification of Cx32 d250 in amphipol a8-35. (A) An SEC profile from the purification of Cx32 d250 after amphipol exchange on Superdex 200 10/300 column. Peaks are labeled: (1) void and (2) Cx32 d250 in amphipol. (B) Electron micrograph of negatively-stained Cx32 d250 corresponding to peak 2 shown in (A). Particles are mostly aggregated protein, and a few *en face* views are observed. Scale bar denotes 50 nm. *Purification optimized by Sandra Poulos.*

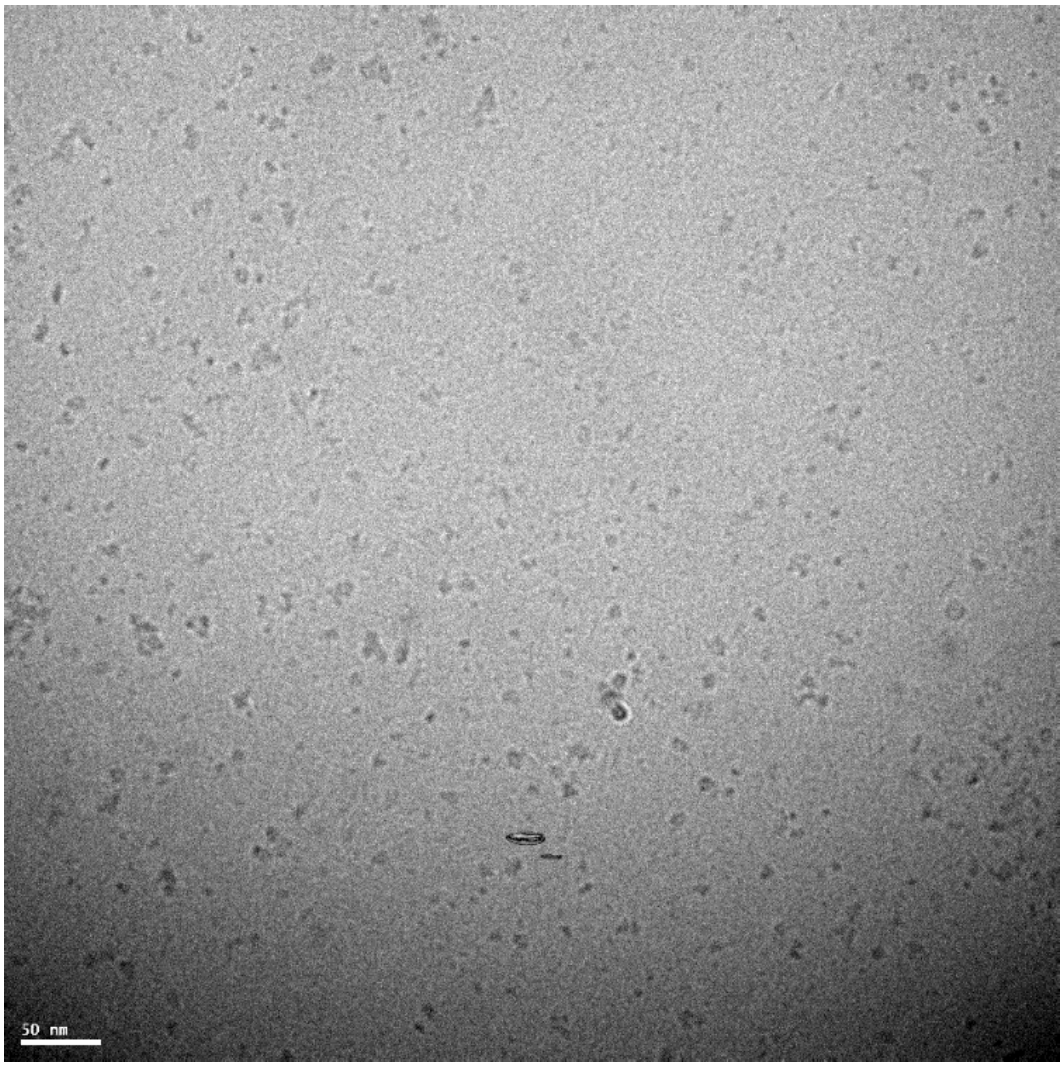

Figure 4.6. CryoEM of Cx32 d250 in nanodisc. CryoEM micrograph Cx32 d250 on pegylated UltrAuFoil holey grids. Particles are mostly aggregated protein and empty nanodisc. Scale bar denotes 50 nm.

4.2. Discussion

The Cx32 GJC forms junctions between myelin sheaths allowing for cytoplasmic continuity within Schwann cells. Mutations in nearly all the residues of the channel result in peripheral nerve degeneration leading to X-linked CMT disease. In order to facilitate structural studies on Cx32 CMT mutants, we have successfully expressed and purified a recombinant Cx32 d250 protein construct for structure determination via cryoEM.

Exchanging Cx32 into membrane mimetics (nanodiscs and amphipol) used for previous cryoEM studies of GJCs prohibited concentration of the channel. This behavior has been previously observed in the purification of the Cx26 GJC requiring a C211S and C218S mutation in the CT to prevent non-native disulfide formation (1). In Cx32, the analogous residues are V210 and C217. Since one of these residues is a cysteine, it may be the case that Cx32 is also forming non-native disulfides prohibiting concentration of the protein. However, unlike Cx26, which showed this behavior in FA-3 detergent, our Cx32 construct can be adequately concentrated in this detergent.

The protocol presented herein can now be applied to generate milligram quantities of Cx32 d250 for structural studies, including single-particle cryoEM and X-ray crystallography. Our results indicate that the protein is stable in FA-3 detergent, which was used previously to crystallize Cx26 (1), and can be concentrated to at least 1 mg/mL. Though the presence of detergent can decrease particle contrast for cryoEM, FA-3 has a relatively low CMC (~0.18 mM) (121, 122), making it more amenable for particle visualization than other detergents.

4.3 Methods

Expression and Purification of Cx32 d250

Expression and purification was adapted from (1). Expression of human Cx32 with a C-terminal hexahistidine tag was performed by infection of *Spodoptera frugiperda* (*Sf9*) insect cells with recombinant baculovirus. Cells were infected at a multiplicity of infection (MOI) of 4 and harvested 50 h post infection. All subsequent steps were performed at 4 °C or on ice, unless otherwise indicated. For lysis, cells were dounce homogenized in low-salt buffer (50mM HEPES pH 7.5, 50mM NaCl, 0.5mM EDTA and Complete protease inhibitor cocktail (Roche) (1 tablet per 100 mL)). Nucleic acids were digested by adding 25 - 29 units of benzonase (EMD Biosciences) per 1 g of cells, adjusting the buffer to include 2.5 mM $MgCl_2$, followed by 10 – 15 min incubation on ice. The lysate was clarified by ultracentrifugation (40,000 rpm for 45 min on a Beckman Coulter Ti-45 rotor), and the pellet was washed with low-salt buffer, high-salt buffer (low-salt buffer with NaCl increased to 1 M) and final wash buffer (high-salt buffer without EDTA). The final pellet contained enriched plasma and organellar membranes. Membranes were stored as aliquots, flash frozen in liquid N_2 and stored at −80 °C until use.

Membranes were thawed on ice and resuspended in extraction buffer (50 mM HEPES, pH 7.5, 1M NaCl, 2.5% (v/v) glycerol, and Complete protease inhibitor cocktail (Roche) (1 tablet per 50 mL). Membranes suspension was dounce homogenized, and *N*-decyl-β-D-maltopyranoside (DM) detergent (Anatrace) was added from a 10% stock solution to the resuspended membranes to a final concentration of 1%

(w/v; ~1 mM; ~10 × critical micelle concentration (CMC)). 10 mM imidazole was added to the solution, and membranes were solubilized overnight on a rotator and followed by ultracentrifugation (40,000 rpm, 45 min) on a Beckman Coulter Ti-45 rotor. Solubilized protein in the supernatant was purified by batch binding the protein to immobilized cobalt affinity resin (Clontech) (preequilibrated with DM wash 1 buffer [50 mM HEPES, pH 7.5, 1M NaCl, 2.5% (v/v) glycerol, and 10 mM imidazole]) at a ratio of approximately 1.5 ml affinity resin per 50 ml detergent extract for 2 h. Slurry was passed through a fritted column, and the beads were washed with at least 6 column volumes (CVs) of DM wash 1 buffer, followed by 5 CVs of DM wash 2 buffer (50 mM HEPES, pH 7.5, 1 M NaCl, 0.5% (w/v) DM, and 25 mM imidazole). To exchange the protein into FA-3 detergent, 1.6 CVs of exchange buffer (50 mM HEPES, pH 7.5, 1 M NaCl, 25 mM imidazole, and 2.5% (v/v) glycerol) containing 0.08% (w/v) FA-3 detergent (4 × CMC) was passed through the column. After the 0.7 CVs had flowed through, the column was capped and incubated for 20 – 25 min before the remaining exchange buffer was flowed through. Column was eluted with 2 CVs of elution buffer (50 mM HEPES, pH 7.5, 1 M NaCl, 25 mM imidazole, 2.5% (v/v) glycerol, and 0.05% (w/v) FA-3 detergent). Imidazole was removed using a G-25 desalting column (GE Healthcare) equilibrated in desalting buffer (50 mM HEPES, pH 7.5, 1.0 M NaCl, 2.5% (v/v) glycerol and 0.025% (w/v) FA-3 detergent). Protein was then further purified by SEC using a Superdex 200 10/300 column.

Cx32 d250 amphipol exchange

The protein sample at 0.8 mg/ml was mixed with amphipol A8-35 (10 mg/ml stock in 50 mM HEPES pH 7.5, 1 M NaCl) at a ratio of 1:2 (w/w) protein to amphipol. The sample was nutated for 2 h at 4 ^{o}C. Additional amphipol solution was added to bring the protein to amphipol ratio to 1:3 (w/w), and solution was nutated for 4 h at 4 ^{o}C. Detergent was removed by adding Bio-Beads SM-2 (BioRad) to a final concentration of 15 mg/ml and overnight nutation at 4 ^{o}C. Bio-beads were then removed over a 0.5 ml disposable fritted column and solution was purified by SEC using a Superdex 200 10/300 column.

Cx32 d250 nanodisc reconstitution

Lipid stock at 7.5 mg/ml (~10 mM) was prepared (Soybean polar lipids, Avanti, Miami, FL). An aliquot of lipid at 25 mg/ml in CHCl3 was transferred into a brown glass vial, dried under an inert gas and solubilized in buffer (25 mM Tris pH 7.5, 150 mM NaCl, 2% n-Octyl-β-D-Glucopyranoside (OG) (w/v)) by vigorous mixing. Purified Cx32 was mixed with nanodisc scaffold protein MSP2N2 and soybean polar lipid extract at a 1:1.5:112 ratio of Cx26 monomer, MSP2N2, and lipid, respectively. Solution was incubated at 4 ^{o}C for 1.75 h on a nutator. Bio-beads SM-2 (BioRad) was added to the solution to a concentration of 10 mg/mL, and solution was incubated at 4 ^{o}C for 3 h on a nutator. A second batch of Bio-Beads SM-2 was added to make a final concentration of 30 mg/mL, and solution was incubated overnight at 4 ^{o}C. Bio-beads were then removed by passing the solution through a 0.5 ml fritted column, eluent was purified further on a Superose 6 column in buffer composed of 25 mM Tris pH 7.5, 150 mM NaCl.

Negative stain EM analysis

For EM of negatively stained samples, a protein sample was applied for 1 min on a glow-discharged, carbon-coated copper grid at a concentration of 0.01 – 0.02 mg/mL. Grid was washed 3 times with ddH_2O followed by 3 washes with 2 % uranyl acetate (UA) pH 4.5, and each wash was followed by blotting with Whatman no. 1 or no. 2 filter paper. For the third wash with UA, the stain was incubated on the grid for 1 min before blotting. EM images were collected using a Tecnai G2 F20 electron microscope (FEI, Hillsboro, OR) equipped with a field-emission electron source, operating at 120 keV. Low electron dose images (~15 e-/$Å^2$) were recorded on a 4K x 4K pixel CCD camera (Gatan, Pleasanton, CA) at 62,000 x magnification (corresponding to 1.8 Å / pixel) with a 1 sec exposure time at a defocus value of approximately -1 to -2 μm.

Chapter 5
Expression, purification, and stabilization of the cardiac gap junction channel Cx43

Ali K. Khan[1] and Mark Yeager[1,2,3,4,]

[1] Department of Molecular Physiology and Biological Physics, University of Virginia School of Medicine, Charlottesville, VA 22908 USA. [2] Center for Membrane Biology, University of Virginia School of Medicine, Charlottesville, Virginia 22908, USA. [3] Cardiovascular Research Center, University of Virginia School of Medicine, Charlottesville, Virginia 22908, USA. [4] Department of Medicine, Division of Cardiovascular Medicine, University of Virginia School of Medicine, Charlottesville, Virginia 22908, USA.

In order to structurally characterize the cardiac gap junction channels Cx40 and Cx43, we seek to determine high-resolution structural models of both isoforms. Cx40 and Cx43 are the primary GJCs in the heart (39). These channels allow for propagation of cadiac action potentials making them potential antiarrhythmic targets (27). In addition, these isoforms share 62% sequence similarity, yet their conductance properties greatly differ (25). High-resolution structures can help elucidate these difference, allowing for a better understanding of GJC ion conduction. This chapter discusses our efforts towards expressing, purifying, and stabilizing the Cx43 GJC for high-resolution structure determination.

For structural characterization of the cardiac connexins, it is essential to purify the channel in at least microgram quantities. In previous X-ray crystallography studies of Cx26, stable recombinant dodecameric channels were purified from *Sf9* insect cells (1, 18), and the group of Guillermo Altenburg has also reported purifying Cx43 hemichannels in this expression system (123, 124). Thus far, while previous members of our group have achieved expression of Cx40 and Cx43 in *Sf9* insect cells (**Figure 5.1**), we have been unable to purify them as channels. Some eukaryotic membrane proteins require specific post-translational modifications, co-factors, or lipid environments that make expression problematic in these systems. To satisfy these expression requirements, we attempted to produce and purify the cardiac connexin Cx43 from human embryonic kidney cell lines (HEK293T and HEK293S GnTI$^-$) (125, 126).

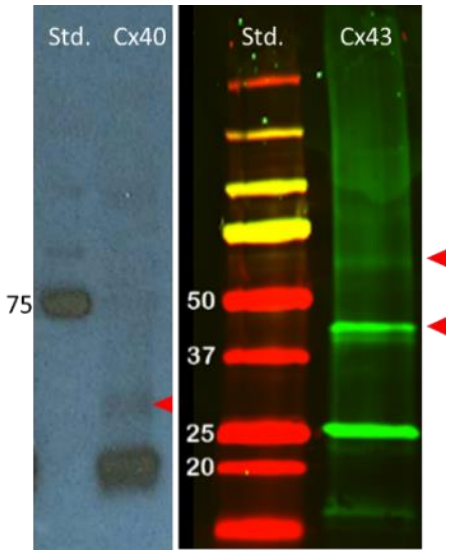

Figure 5.1: Expression of Cx40 and Cx43 in *Sf9* cells. Immunoblots detecting expression of C-terminal truncations of Cx40 and Cx43. Molecular weight of the Cx40 and Cx43 constructs are 31kDa and 28 kDa, respectively. Lanes marked "Std." contain molecular weight standards with the weight (in kDa) indicated. Connexin samples separated by SDS-PAGE typically display bands of SDS-resistant oligomers (red arrows). *Experiments by Brad Bennett*.

5.1. Results

5.1.1. *FSEC analysis of Cx43 orthologues*

We screened eGFP membrane protein fusions from transiently transfected cells in a 9.6 cm^2 culture area for expression level using fluorescence-detection size-exclusion chromatography (fSEC) (126). Shown in **Figure 5.2** is our screen on various Cx43 orthologues. In one step, we inserted connexin genes from several species into a pcDNA3 vector with a cleavable C-terminal GFP and affinity tag (polyhistidine or FLAG-One-Strep [FOS] Tag (127)) for easy purification. FSEC of the crude solubilized membranes from transfected cells reveals relative expression levels among orthologues with the chicken, dog, human, and rat Cx43 constructs displaying the highest degree of expression. Though expression in mammalian cells was achieved, all Cx43 orthologues were primarily purified in the non-physiological monomeric state.

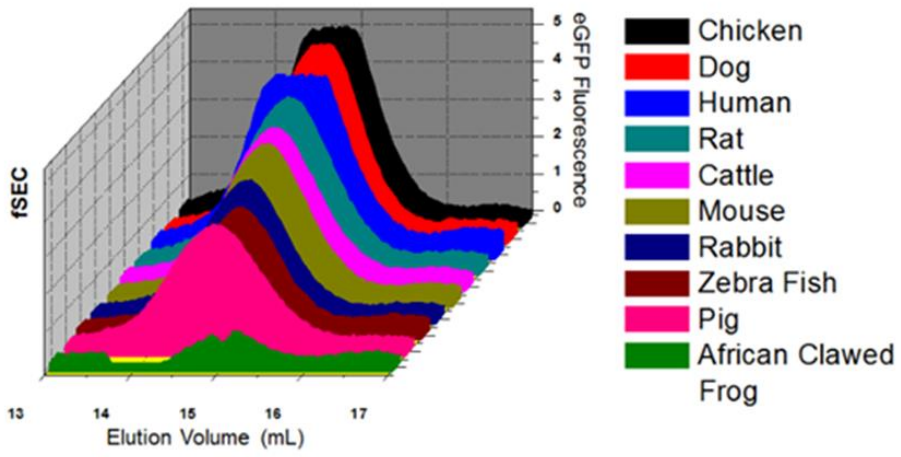

Figure 5.2. Screening of Cx43 Orthologues. FSEC traces of Cx43-eGFP fusions reveals relative expression. All orthologues eluted at a molecular weight corresponding to the monomeric state.

5.1.2 *Stabilization of hexameric and dodecameric channels by engineered disulfide crosslinks*

We used the X-ray crystal structure of Cx26 (PDB 5ERA) (1) to engineer single disulfide crosslinks between adjacent subunits of human Cx43. The sites of potential crosslinks were determined by locating homologous amino acid residues on adjacent Cx26 protomers that had a Cβ - Cβ atom distance less than 8 Å or a Cα- Cα atom distance less than 5 Å. We were pleased to see that if a crosslink was engineered in the transmembrane domain near the cytoplasmic region of the Cx43 channel, our fSEC screening revealed an enriched population corresponding to the molecular weight of the physiologically relevant hemichannel species (**Figure 5.8 – 5.10**). In addition, if a crosslink is engineered in the extracellular domain, fSEC showed a peak corresponding to the molecular weight of the full Cx43 gap junction channel (GJC) (**Figure 5.3 – 5.7**). We noticed that crosslinks L90C V28C (**Figure 5.9**) and L91C W25C (**Figure 5.10**), in particular, had high expression of the hexameric state compared to the monomer. In an attempt to boost the expression of the dodecameric species, we engineered double disulfide crosslinked constructs, which combined the L90C V28C and L91C W25C mutations from the high expressing hexameric constructs with the D67C R202C, D67C T204C, and G60C F199C mutations that resulted in the dodecameric species. Unfortunately, the fSEC traces of the double disulfide constructs (**Figure 5.11 – 5.15**) recapitulated the profile of the single crosslinked dodecameric species.

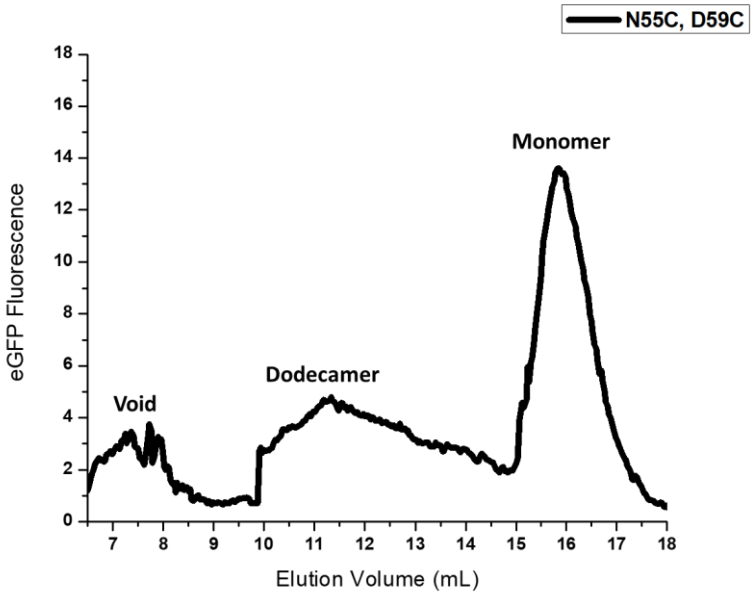

Figure 5.3. FSEC of human Cx43 N55C D59C.

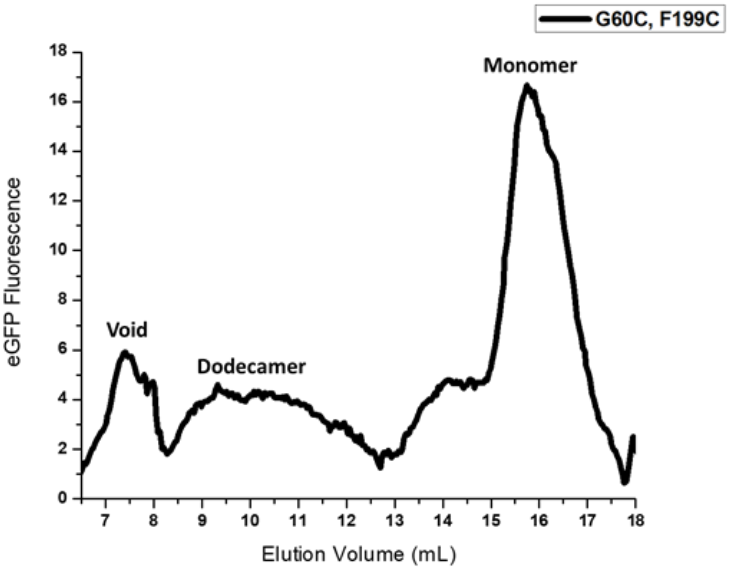

Figure 5.4. FSEC of human Cx43 G60C F199C.

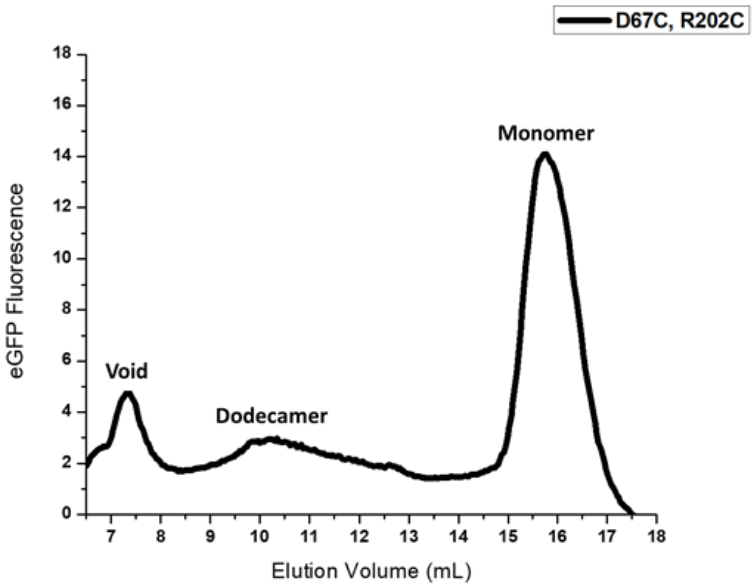

Figure 5.5. FSEC of human Cx43 D67C, R202C.

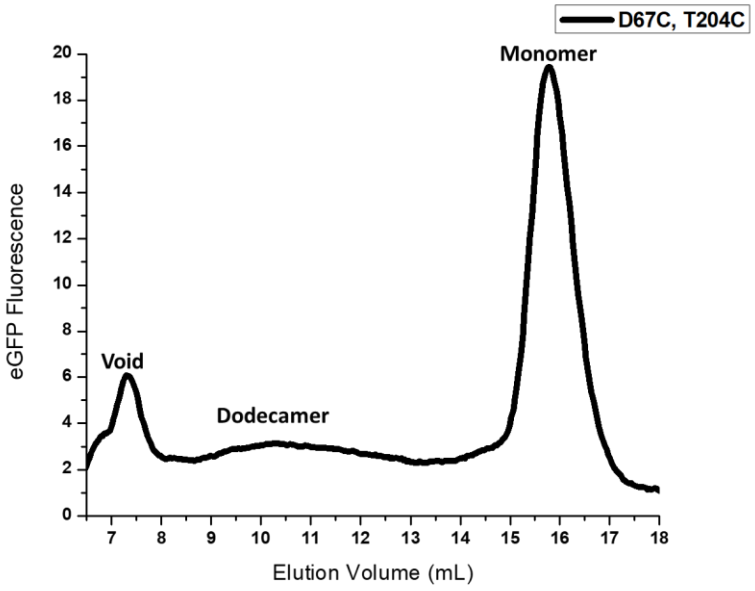

Figure 5.6. FSEC of human Cx43 D67C, T204C.

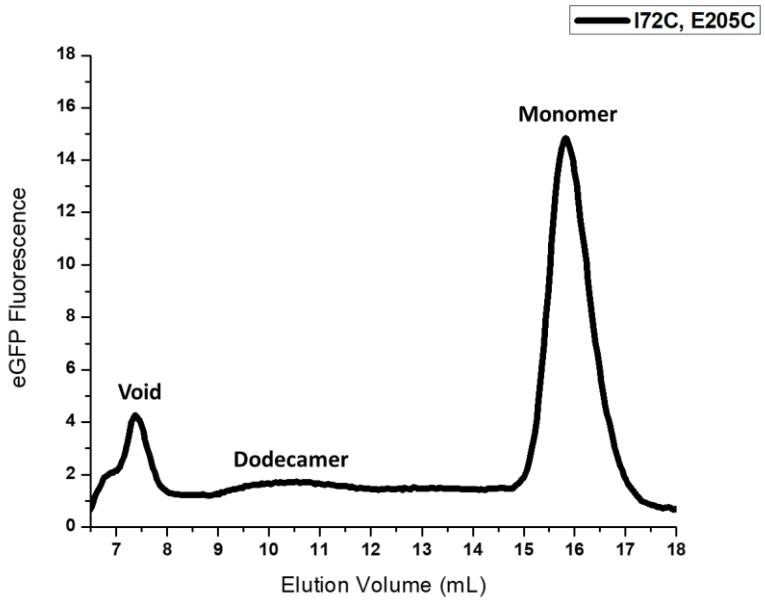

Figure 5.7. FSEC of human Cx43 I72C, E205C.

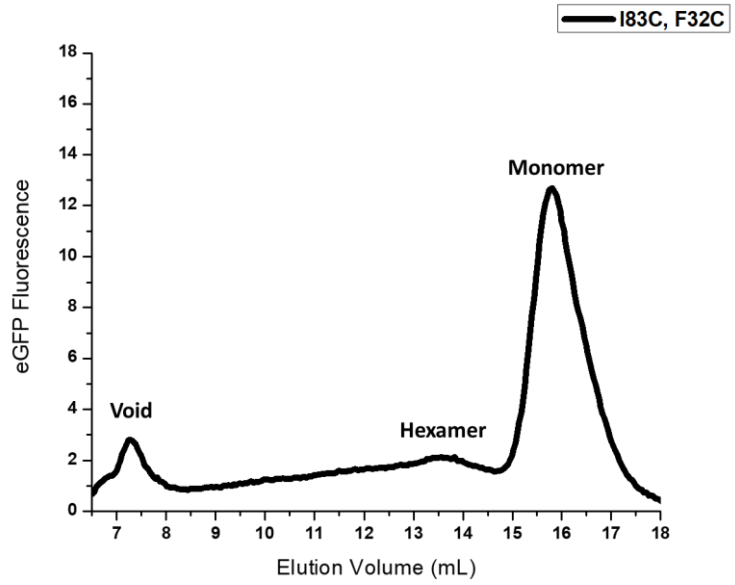

Figure 5.8. FSEC of human Cx43 I83C, F32C.

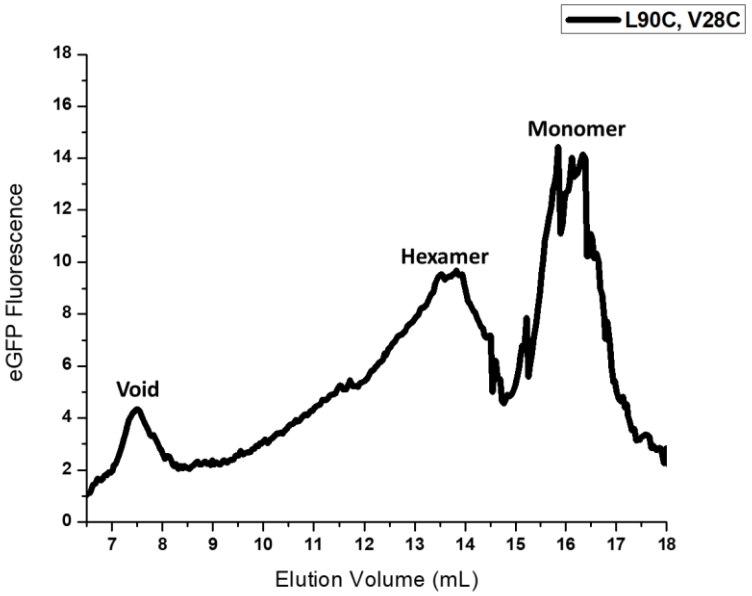

Figure 5.9. FSEC of human Cx43 L90C, V28C.

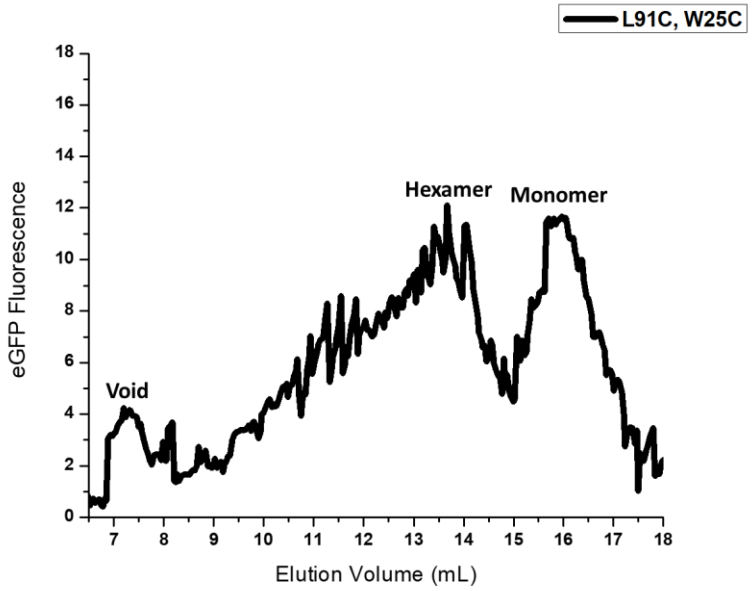

Figure 5.10. FSEC of human Cx43 L91C W25C.

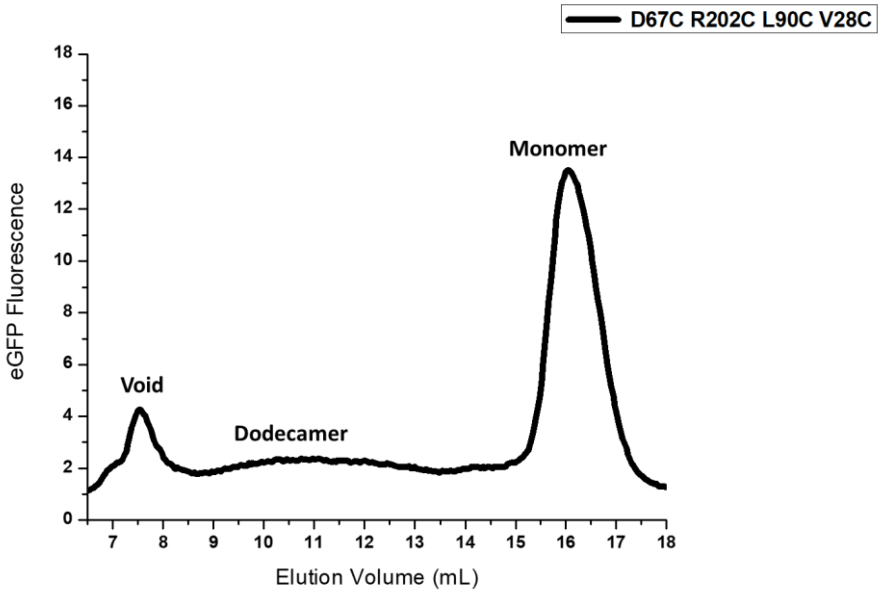

Figure 5.11. FSEC of human Cx43 D67C R202C L90C V28C.

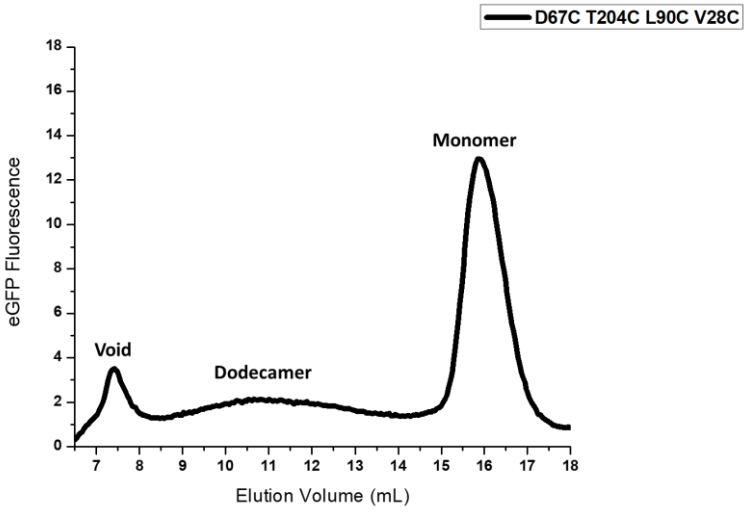

Figure 5.12. FSEC of human Cx43 D67C T204C L90C V28C.

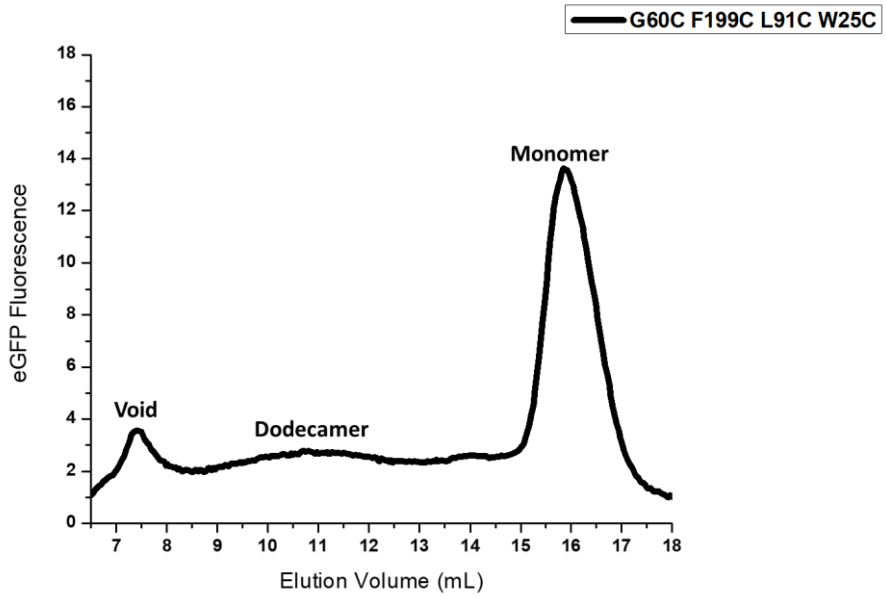

Figure 5.13. FSEC of human Cx43 G60C F199C L91C W25C.

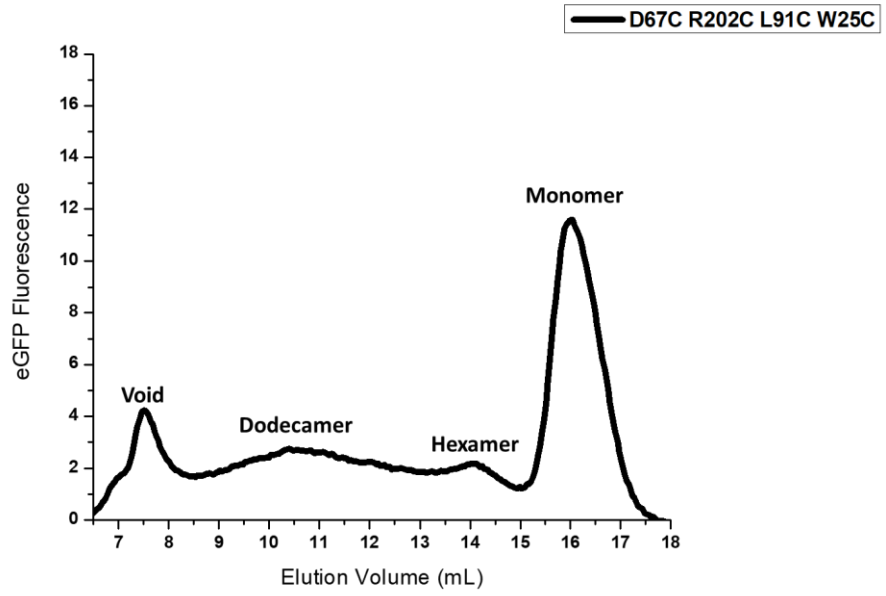

Figure 5.14. FSEC of human Cx43 D67C R202C L91C W25C.

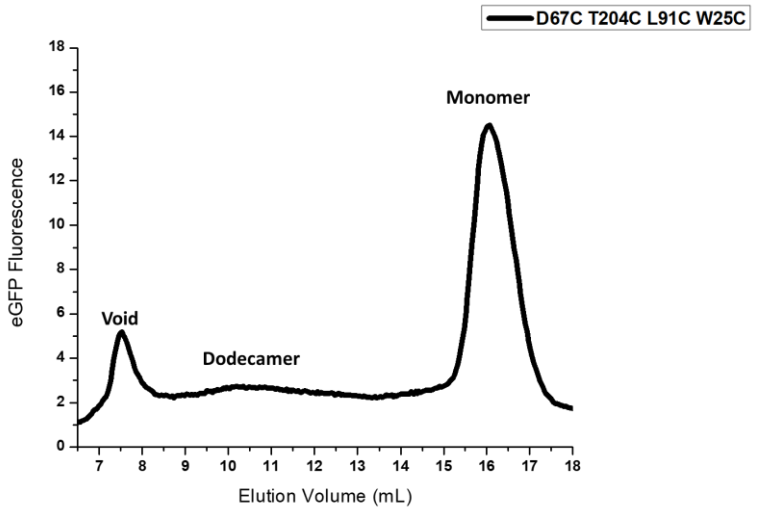

Figure 5.15. FSEC of human Cx43 D67C T204C L91C W25C.

5.2. Discussion

Although the functional properties of cardiac connexins have been characterized for over three decades, structural characterization has been elusive. While sharing 62% sequence identity (75% in the TMD), the cardiac connexins Cx40 and Cx43 greatly differ in conduction profile, ion selectivity, and size selectivity (25, 50, 51). High-resolution structures of these channels may help elucidate these stark differences and could pave the way for rational drug design of new antiarrhythmic medications.

In this chapter, we have described our efforts toward recombinant expression, purification, and stabilization of the Cx43 channel for structural studies. Since previous

efforts of purifying this channel from *Sf9* cells proved futile, we resorted to expressing Cx43 in a mammalian cell line. We chose the HEK293 cell line because it endogenously expresses Cx43 (128) and because recent studies show that protein expression can be scaled to a level sufficient for both X-ray crystallography and cryoEM experiments (108, 126, 129-131).

While we are able to express various Cx43 orthologues in HEK293 cells, our fSEC experiments show that the protein is purified in the monomeric form. Most likely, the resulting monomeric state is an artifact of detergent solubilization because previous studies have shown that functional Cx43 channels can be expressed in HEK293 cells with and without a C-terminal GFP tag (132). Using the structure of Cx26 (1), we then attempted to stabilize the physiologically relevant oligomeric state of the protein by engineering disulfide crosslinks between adjacent protomers. Disulfide crosslinks in the TMD closer in proximity to the cytoplasmic domains resulted in purification of both the monomeric and hexameric form of the protein (**Figure 5.8 – 5.10**). This observation supports that our expression in HEK293 cells results in the proper assembly of the Cx43 hemichannel in the membrane.

Disulfide crosslinks engineered in the extracellular domain resulted in purification of both monomeric and dodecameric species **(Figure 5.3 – 5.7**). These particular crosslinks appear to dictate the oligomeric state because engineering additional disulfide crosslinks results in little or no change to the quantity of dodecameric species in the fSEC profiles (**Figure 5.11 – 5.15**). It is likely that these extracellular domain crosslinks not only stabilize the adjacent protomer-protomer interface within a hemichannel, but also stabilize the

extracellular interface that mediates docking between hemichannels. Currently, structural differences between GJCs and hemichannels are not well understood. Our crosslinking results suggest that the Cx43 hemichannel extracellular domains are in a conformationally heterogenous state that are not amenable to hemichannel docking unless it adopts a conformation similar to the Cx26 extracellular docking interface.

5.3. Methods

DNA Cloning of Connexin Orthologues

For FSEC screening, connexin orthologs were cloned into a modified pcDNA3-eGFP (Addgene, plasmid #13031) with a cleavable Tobacco Etch Virus (TEV) site and 6x-polyhistidine tag (HIS) upstream and downstream of GFP site, respectively. Using a Quikchange Lightning Site-Directed Mutagenesis Kit, the TEV site was inserted using a 5'-GCGGCCGCTCGAGGAGAATCTGTATTTCCAGGGAATGGTGAGCAAGG-3' primer with a primer of the reverse sequence, the HIS tag was inserted using a 5'-GGACGAGCTGTACAAGCACCATCACCATCACCATTAATCTAGAGGGCCCT-3' primer with a primer of the reverse sequence. In addition, we also created a pnDNA3 vector with a FOS tag by engineering an AflII restriction site upstream of the HIS tag and using In-Fusion Cloning Kit (Takara Bio USA, Inc) to insert a PCR fragment of the FOS tag with upstream PreScission Protease Site into the AflII site. Cx43 and Cx40 orthologues genes were obtained commercially from Genscript Biotech, and PCR fragments of each orthologue gene was generated with a 5' EcoRV and 3' Xho1 site using a Phusion

polymerase (New England Biolabs). Using an In-Fusion Cloning Kit (Takara Bio USA, Inc), PCR fragments (purified on a 1% agarose gel) were inserted into our modified pcDNA3-eGFP vector, which was previously digested with EcoRV HF and Xho1 restriction enzyme and purified on a 1% agarose gel.

Expression and FSEC analysis of Connexin Orthologues

In a 6-well tissue culture treated tray, 5 x 10^5 HEK293T cells were plated in each well in DMEM media (with 4.5 g/L D-Glucose and L-Glutamine) (Thermo Fisher Scientific) supplemented with 10% heat-inactivated fetal bovine serum, and incubated overnight (37 ^oC, 5% CO_2) till at least a 50% confluency was reached. To prepare transfection complex, 3.3 µg of each plasmid was added to OptiMEM media to a total volume of 155 µL. 9.9 µL of FuGENE HD reagent (Promega Corporation) was mixed with each plasmid solution and incubated at room temperature for 5-10 minutes. 150 µL of each transfection complex solution was added dropwise to each well and mixed by gently shaking the tray. Cells were incubated for roughly 2 days (37 ^oC, 5% CO_2). Media was aspirated from the cells, and cells were rinsed with 2 mL of PBS buffer. Cells were dislodged from tray by repetitive pipetting with 1 mL of PBS buffer and centrifuged at 5000 g for 1 min. Supernatant was discarded, and cells were resuspended in 500 µL of 20 mM Tris pH 8, 150 mM NaCl buffer with cOmplete protease inhibitor cocktail (Sigma-Aldrich). Cells were lysed via sonication for 10 seconds and centrifuged at 8000g for 10 minutes. Supernatant was isolated and centrifuged for 40 min at 100,000 g to pellet membranes. Supernatant was removed, and membrane pellets were flash frozen in liquid

nitrogen and stored in -80 ºC till solubilization for fSEC. Based on previous studies (124), membranes were solubilized in 200 µL of 10 mM Glycine/NaOH pH 10, 2 M NaCl, 10 mM EDTA, 10mM DTT, 1% DM with cOmplete protease inhibitor for 1.5 hour at 4 ºC. Insoluble material was removed by centrifuging sample for 40 min at 100,000 g. FSEC was performed 50 µL of supernatant using a Superose6 column with the fluorescence detector excitation and emission values set at 489 nm and 509 nm, respectively.

Cloning of disulfide stabilized Cx43 constructs

Using the pairwise distances script (133) in PyMOL (134), candidate residue for cysteine mutagenesis were determined by identifying Cα-Cα or Cβ-Cβ distances of less than 8 Å or 5 Å, respectively, between residues on adjacent protomers of the Cx26 crystal structure (PDB 5ERA) (1). Cysteine mutagenesis was performed on the human Cx43 construct in our modified BacMam vector using a QuikChange Multi kit (Agilent) with primers designed using the online QuikChange Primer Design tool (https://www.genomics.agilent.com/primerDesignProgram.jsp).

FSEC of disulfide stabilized Cx43 constructs

Expression in HEK293T cells was performed the same way as for Cx43 orthologues stated above. Cells were resuspended in 500 µL of 20 mM Tris pH 8, 150 mM NaCl buffer (with cOmplete protease inhibitor) and lysed by two rounds of sonication for 5 sec. The resulting solution was centrifuged at 8000 g for 10 min at 4 ºC,

and the supernatant was isolated and centrifuged at 100,000 g for 40 min at 4 ^{o}C to pellet membranes. After removing the supernatant, the membranes were flash frozen in liquid N_2 and stored in a -80 ^{o}C freezer till solubilization. Membranes were solubilized in 200 µL of 10mM HEPES pH 7.5, 1M NaCl, 3% DDM with cOmplete protease inhibitor for 1 h nutating at 4 ^{o}C. The insoluble components of the solution were removed via centrifugation at 100,000 g at 4 ^{o}C for 40 min, and 100 µL of supernatant was loaded on a Superose 6 column for fSEC.

Chapter 6
Future Directions

6.1. pH-gating of Gap Junction Channels: Visualization of a "ball-and-chain" by cryoEM

Future efforts would be directed towards further elucidation of the structural mechanism of pH gating. In terms of the oligomeric "ball-and-chain," we infer from the acidic pH structure that six NTs form the "ball." In K^+ channels, only one N-terminal "ball-and-chain" particle out of four is required to gate the channel (79, 135). While it is difficult to envision only one NT gating the large 15 Å diameter pore of a GJC, it may be that fewer than six NT can form an occluding "ball." Such is the case with closely related pannexin channels, which do not require participation from all channel protomers to achieve C-terminal gating. As was performed with pannexin channels, generating connexin concatemers may be the key for elucidating the required gating stoichiometry for pH regulation (78). By generating a Cx26 concatemer with protease sites between subunits,

we can have strict control over the NT stoichiometry and use functional assays complemented with single-particle cryoEM to characterize the “ball-and-chain” gating. Cx26 concatemers may also be the key to unambiguously identify the protein domain that forms “ball-and-chain” particle. Thus far, attempts to modify the NT region of Cx26 has resulted in severe expression defects. We may be able to generate NT deletions in a concatemer construct and use cryoEM see the effect it has on “ball-and-chain” density.

In this project we also identified unique lysine crosslinking behavior at physiological and acidic pH in the unresolved cytoplasmic domains of the channel. By using modern hybrid and integrative modeling techniques previously used by *Sali et al.* (136, 137), we hope to use the cryoEM maps and the crosslinking results to assist us in further discerning the conformational changes associated with pH gating.

Lastly, since single-particle cryoEM does not require formation of crystals, this work also demonstrates a more efficient method for determining Cx26 GJC structures. Our cryoEM approach can now be used to reconstruct disease mutation constructs in order to elucidate structural changes associated with sensorineural hearing loss (**Figure 1.11**) (1, 58, 138).

6.2. CryoEM structure of a connexin hemichannel

To complement the hemichannel structure, we will functionally characterize the Cx26 N176Y hemichannel. While the equivalent N175Y mutation in Cx32 resulted in functional hemichannels (65, 66), it may be that this mutation in Cx26 is affecting the

open/closed state (139). Using known patch clamping (140) or dye assays (141), we will be able to assess if Cx26 N176Y is functionally equivalent to WT.

It would also be worthwhile to investigate the structural basis of Ca^{2+} and pH mediated regulation of the hemichannel. Currently, it is unknown if the structural mechanism of inhibition is conserved between GJCs and hemichannels. Our group previous proposed that Ca^{2+}-mediated inhibition of GJCs occurs by an electrostatic block (1), which disagreed with the steric camera-iris model of inhibition proposed by *Unwin and Ennis* (12). As has be suggested by AFM studies (139), the steric mechanism of closure may still be relevant for connexin hemichannels. In the context of pH regulation, AFM studies also demonstrated a narrowing of the hemichannel pore in acidic conditions (142), which is not consistent with our low pH occluded GJC structure that shows no changes in the pore diameter (**Chapter 2**). It too may be the case that the mechanism for pH inhibition is not conserved.

Our approach for determining the hemichannel structure can also be applied towards the structural studies of hemichannel disease mutations. Assuming that Cx26 N176Y functions as WT, we can purify hemichannel disease mutation constructs in the N176Y background and evaluate the structural differences via cryoEM.

6.3. Expression, purification, and stabilization of the Cx32 gap junction channel

Our expression and purification protocol of Cx32 d250 enables us to perform single-particle cryoEM to reconstruct the channel. Ultimately, if a high-resolution

reconstruction is obtained, it will serve as a starting model for cryoEM, molecular dynamic simulations and other structural techniques, which will be used to investigate the structural effect of CMT disease mutations.

6.4. Expression, purification, and stabilization of the cardiac gap junction channel Cx43

The ultimate goal of this project is to purify the Cx43 GJC for structure determination by either X-ray crystallography or cryoEM. The first obstacle will be to purify the channel in the correct oligomeric state. The studies highlighted in **Chapter 5** show that unless the protein oligomeric state is stabilized by covalent linkages between protomers, detergent solubilization can result in the channel separating into solely the monomeric form. Even with disulfide crosslinks between adjacent protomers, majority of the protein is still isolated as a monomer; therefore, more optimization of the purification protocol is required. One hypothesis is that components of the lipid membrane are essential for channel assembly. It is known that cardiac gap junction channels are localized in cholesterol-rich membrane environments and that channel conductance is abrogated by changes in membrane fluidity (3, 143). It should also be noted that the previous moderate resolution structures of Cx43 were solved by 2D crystallography of the channel purified in the native lipid membrane, though no bound membrane components were visualized in the maps (11, 13, 14, 16). If assembly is maintained by weak lipid interactions, our stabilized constructs will need to be extensively screened in various detergents to check if a particular detergent can maintain the channel structure. Another strategy is to use styrene maleic acid

co-polymers (SMA) to extract the assembled channel surrounded by native lipids out of the membrane without the use of detergents (144, 145). Such a method has already shown promise for membrane protein structure determination by single-particle cryoEM (146).

Appendix
Summary of single-particle cryoEM image processing

Here we describe the steps for deriving a 3D map of a macromolecular complex by single-particle image analysis of electron micrographs. In summary, once many micrographs of putatively identical molecules in random orientations are obtained, tens of thousands of particles are then aligned and averaged to generate a de novo three-dimensional (3D) reconstruction (129). While direct electron detectors can record images with higher signal-to-noise than either film (**Figure A.1**) or CCD detectors (109), several inconveniences arise in the imaging and experimental data. The sensitivity of biological materials to radiation damage requires that images are recorded under minimal electron dose conditions, which decreases the signal-to-noise ratio (SNR). In order to achieve contrast for particle visualization, a defocus must be applied, which leads to artifacts in the contrast transfer function (CTF) (88, 147). Lastly, cryoEM experimental data are incomplete because the relative orientation of each two-dimensional particle projection with respect to one another in three-dimensional space is unknown (148). Modern image processing methods can compensate for these obstacles. The flowchart in **Figure A.2** describes the image processing steps employed to achieve high-resolution 3D maps, and a summary of the steps is as follows:

1) Images are collected as movies so that the effects of image blurring from beam-induced specimen movement and radiation damage can be corrected in subsequent steps (149). Automated collection programs such as EPU (FEI Company), SerialEM, and Leginon (150) enable thousands of images to be recorded quickly with very little human intervention. Having larger particle datasets compensates for the low SNR that arises from recording images using low-dose conditions.

2) Movie frames are aligned to correct for beam-induced specimen movement. Programs such as Motioncorr (151) and Unblur (152) perform the correction on whole movie frames. The Motioncor2 algorithm, in addition to whole frame correction, subdivides each frame into patches and aligns each patch individually, correcting for local motion that varies across the micrograph (115). Unblur and Motioncor2 can also perform a dose-weighting operation that appropriately weights individual frames to reduce the deleterious effects of radiation damage, hence increasing the SNR of each particle.

3) Micrographs must be corrected for effects of the CTF parameters to obtain a high-resolution reconstruction. Several programs are available to determine the CTF. The most popular are CTFFIND (84) and Gctf (88). Gctf has a GPU-accelerated algorithm that reduces computation time to seconds per micrograph.

4) Particle picking can be performed manually, using several programs and software packages such as RELION (85-87) and EMAN2 (153, 154). Dr. Kai Zhang's program

Gautomatch has semi-automated, particle diameter-based, or template-based, automated picking procedures that substantially increase the picking rate. A common strategy is to manually pick 1000 – 2000 particles and generate two-dimensional (2D) class averages that serve as templates for autopicking.

5) Individual particles are grouped by orientation and averaged to generate 2D class averages with increased SNR. In EMAN2, particles are grouped together using K-means clustering, and RELION employs a maximum likelihood (ML) algorithm (148). 2D class averages provide an excellent initial assessment of particle homogeneity and heterogeneity. Excluding low-quality or nonsensical class averages can remove "bad" particles. For successful high-resolution 3D reconstruction, the expectation is that 2D class averages should display secondary structural features such as α-helices. If these features are not present, there is a very low likelihood that a dataset will result in a high-resolution reconstruction (155).

6) A low-resolution (30-60 Å) initial model is required for the subsequent 3D classification and refinement steps. Several methods can be used, including a negative-stain EM reconstruction, EM tomography, conical-tilt reconstruction, reconstruction by the common-lines method and low-pass filtering of a previously determined atomic model determined by X-ray crystallography. The best practice is to use a *de novo* model generated from the cryoEM data itself. EMAN2 combines different 2D class averages into 3D models using a Monte-Carlo approach and then refines these models using the

class averages (156). RELION and cryoSPARC employ a stochastic gradient descent algorithm (117) using random subsets of particles.

7) For 3D refinement, it would be ideal to use a set of identical particles in random orientations. However, data sets always include some degree of heterogeneity arising from contamination due to incomplete purification and particle degradation due to beam damage, denaturation, aggregation, disassembly and/or proteolysis of the complex. Heterogeneity may also arise from multiple states of a macromolecular complex, which have functional significance. The goal is to center the particles to a common coordinate system and then determine the θ, ϕ and ω Euler angles for each particle, so the 2D projection images can be computationally merged to determine a 3D structure, (The convention is that ω is the rotation angle of the particle in the 2D projection image.)

8) The ML 3D classification algorithm employed in RELION is used to classify and sort particles of different 3D conformations. It is very important to use a low-resolution initial model for this step to prevent model bias. If multiple conformations are present, particles from each 3D class average can be refined independently to yield multiple reconstructions. It is sometimes the case that only one class will refine to high-resolution, while the others refine to low or sub-nanometer resolution.

9) With a particle subset of sufficient homogeneity, a low-resolution initial model (or 3D class average) can be refined to high-resolution. The two primary approaches to refinement are maximum cross-correlation (CC) (implemented in EMAN2) and maximum-likelihood (implemented in cryoSPARC and RELION). In maximum cross-correlation, a particle is compared to 2D projections of the initial model in all θ, ϕ and ω Euler orientation angles and is assigned to the orientation to which it has the highest CC. In the maximum-likelihood approach, particles are compared to 2D projections of the initial model, and the particle has a probability-weighted angular assignment to each orientation based on similarity. In a noiseless data set, both approaches are equivalent; however, maximum-likelihood has better convergence behavior in noisy data, which is typical for low SNR images determined by cryoEM.

10) Using the particle coordinates and aligned movies, the SNR can be further improved using the "particle polishing" procedure (89) in RELION. By this approach the motion for each particle is individually corrected. By estimating an inverse B-factor and a linear intensity factor to describe the resolution-dependent power in each frame, movie frames can be appropriately weighted to minimize the effects of radiation damage and rapid motion, without sacrificing the useful low-resolution information in the down-weighted frames. Computationally, this procedure is very expensive, and refinements may not benefit if the movies were dose-weighted and patch-based aligned (115).

11) The refinement is repeated with the “polished” particles to improve the resolution of the map.

12) Masking out noisy peaks and sharpening by application of an inverse B factor further enhances high-resolution features in the map (**Figure A.3**).

13) Accurate map validation and resolution estimation are required to ensure that the correct particle orientations have been determined, ruling out spurious features arising from noise and overfitting. A useful approach is to examine images of particles at two known rotation angles in the electron microscope (104). By this approach, one can perform a refinement that is independent of the derived orientation angles between the pairs to determine the correctness of the tilt angles and axis. This method can also be used to determine the absolute hand of a 3D structure. An online tilt pair validation server (https://www.ebi.ac.uk/pdbe/emdb/validation/tiltpair/) provides a free and convenient tool for performing these measurements (157).

14) Measuring an accurate resolution for the map dictates the extent of detail that can be built in the model. For example, only α-helices may be positioned in a 7-10 Å map, and the directionality will be uncertain. A 4-6 Å map will indicate directionality and hand, and a Cα model for the polypeptide can be built. Density for bulky aromatic side chains may be evident, but rotamer configurations of side chains will be uncertain. At a resolution of 3 Å or better, side chain positions will be defined, and rotamer

configurations can be refined for many or most. At a resolution of 2 Å or better, density for water molecules may be evident.

15) Currently, the gold-standard is to split the data into two random half-sets and assign the resolution at which the Fourier shell correlation (FSC) equals 0.143 as the global resolution of the model. While many programs can calculate an FSC curve, RELION and cryoSPARC use a gold-standard approach to high-resolution refinement (**Figure A.2** steps 8 and 10), which incorporates the FSC into the refinement to prevent overfitting and the buildup of noise (85, 117, 155).

16) While a global resolution can be assigned, it is apparent that cryoEM maps do not have a uniform resolution. The program ResMap calculates local resolution by detecting the smallest sinusoidal feature above the noise in every voxel of the map (**Figure A.3A**) (104).

17) Using modeling tools (Coot (94, 158), Phenix (159), and CCP4 (160) commonly used in X-ray crystallography, a structural model can be built and real-space refined from the density (**Figure A.3A**).

18) Remember that maps derived by X-ray crystallography display the electron density, whereas maps derived by electron microscopy display the Coulombic potential. The

form factors for X-ray scattering are proportional to z, whereas the form factors for electron scattering are dependent on the local electronic environment. A consequence is that carboxyl groups of acidic amino acids may not be visible in cryoEM maps. (It may also be the case that carboxyl groups are not visible due to radiation damage.)

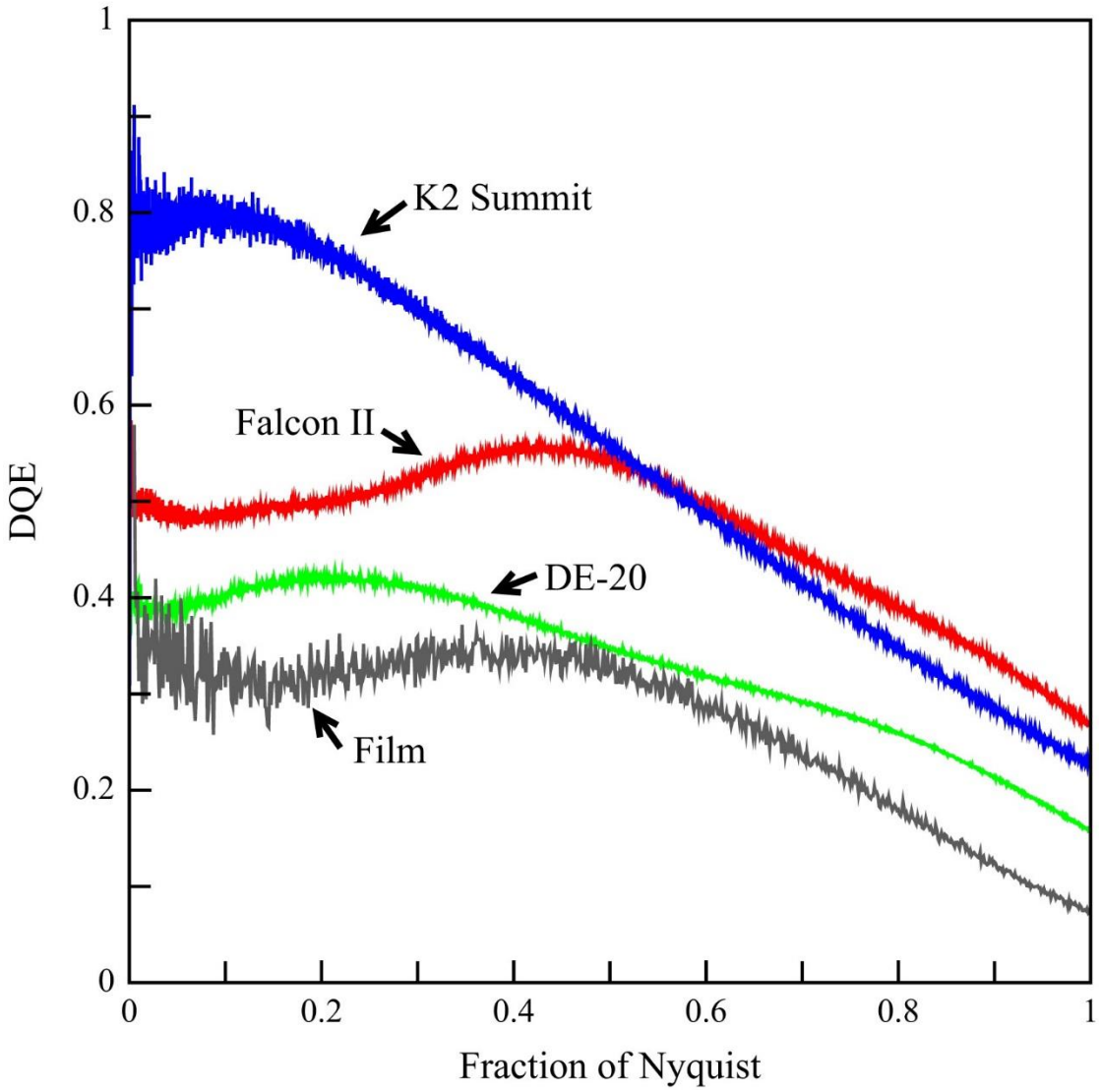

Figure A.1. **Detective quantum efficiency (DQE) of direct electron detectors is better than film.** Measured DQE is plotted as a function of spatial frequency for the DE-20 (green), Falcon II (red), and K2 Summit (blue) direct electron detectors with that of film (black). Image is from (109).

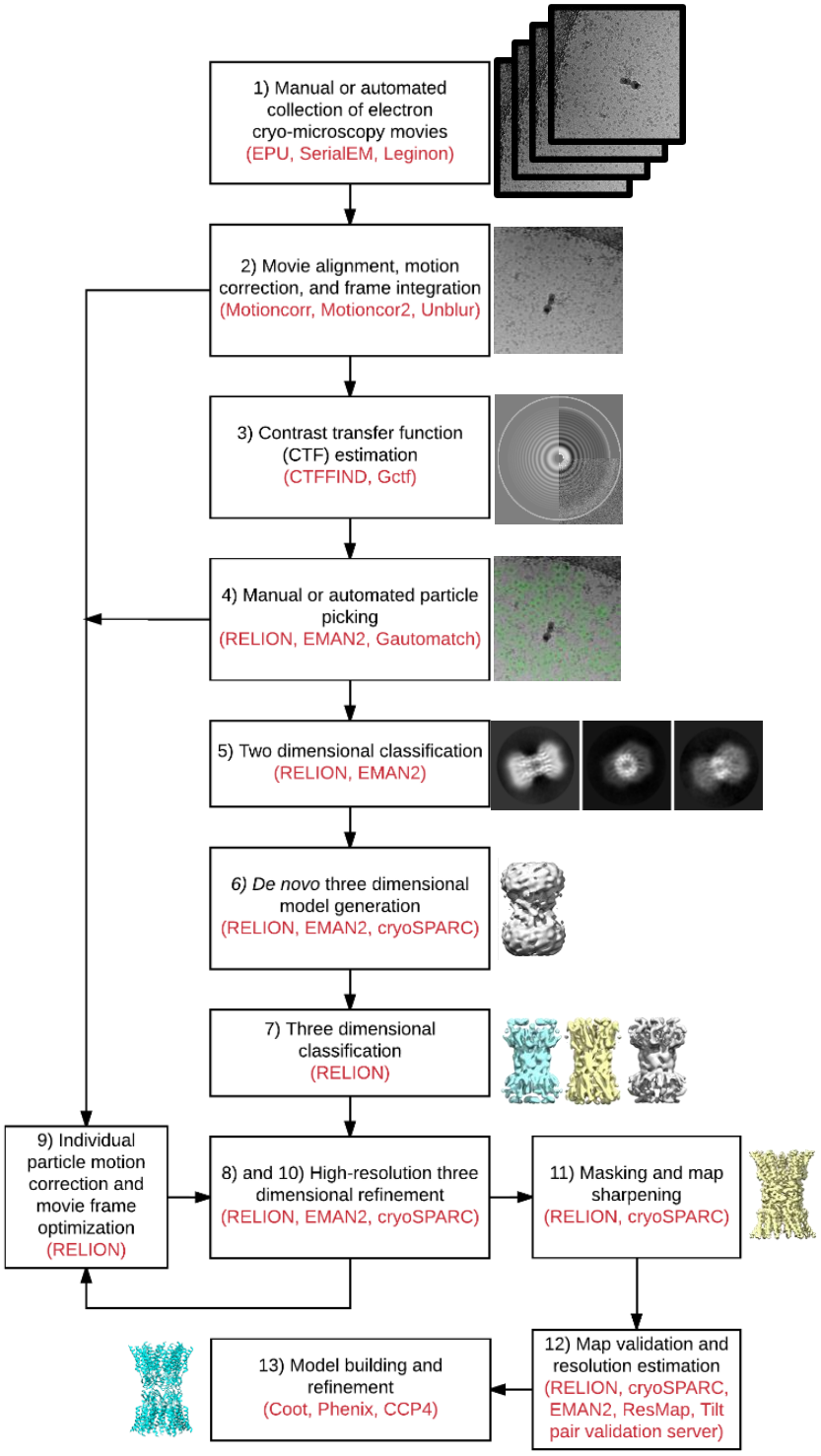

Figure A.2. Flowchart of single-particle cryoEM image processing steps with thumbnail examples from data processing of the human Cx26 gap junction channel. Relevant software is indicated with red text.

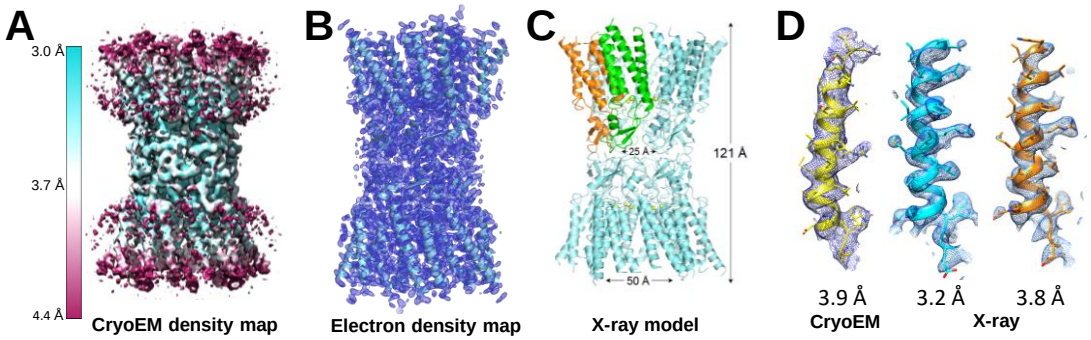

Figure A.3. Cx26 gap junction channel solved by single-particle cryoEM and X-ray crystallography. A) CryoEM density map after high-resolution refinement, masking, and B-factor sharpening in RELION. Map is colored by local resolution calculated using ResMap with color bar shown. Single-particle cryoEM achieves comparable detail to the density (B) and model (C) derived by X-ray crystallography (PDB 5ER7) (1). D) Comparison of Cx26 transmembrane helix 1 solved to by cryoEM and two X-ray models (PDB 5ER7 and 5ERA) with resolutions indicated.

References

1. Bennett BC, Purdy MD, Baker KA, Acharya C, McIntire WE, Stevens RC, Zhang Q, Harris AL, Abagyan R, Yeager M. An electrostatic mechanism for Ca(2+)-mediated regulation of gap junction channels. Nature communications. 2016;7:8770. doi: 10.1038/ncomms9770. PubMed PMID: 26753910.

2. Loewenstein WR. Junctional intercellular communication: the cell-to-cell membrane channel. Physiol Rev. 1981;61(4):829-913. Epub 1981/10/01. doi: 10.1152/physrev.1981.61.4.829. PubMed PMID: 6270711.

3. Harris AL. Emerging issues of connexin channels: biophysics fills the gap. Quarterly Reviews of Biophysics. 2001;34(03). doi: 10.1017/s0033583501003705.

4. Milks LC, Kumar NM, Houghten R, Unwin N, Gilula NB. Topology of the 32-kd liver gap junction protein determined by site-directed antibody localizations. EMBO J. 1988;7(10):2967-75. Epub 1988/10/01. PubMed PMID: 2460334; PMCID: PMC454678.

5. Yeager M, Gilula NB. Membrane topology and quaternary structure of cardiac gap junction ion channels. Journal of molecular biology. 1992;223(4):929-48. Epub 1992/02/20. PubMed PMID: 1371548.

6. Yeager M, Harris AL. Gap junction channel structure in the early 21st century: facts and fantasies. Curr Opin Cell Biol. 2007;19(5):521-8. Epub 2007/10/20. doi: 10.1016/j.ceb.2007.09.001. PubMed PMID: 17945477; PMCID: PMC2819411.

7. Kumar NM, Gilula NB. The gap junction communication channel. Cell. 1996;84(3):381-8. PubMed PMID: 8608591.

8. Beyer EC, Paul DL, Goodenough DA. Connexin43: a protein from rat heart homologous to a gap junction protein from liver. J Cell Biol. 1987;105(6 Pt 1):2621-9. Epub 1987/12/01. PubMed PMID: 2826492; PMCID: PMC2114703.

9. Yeager M. Structure of cardiac gap junction intercellular channels. J Struct Biol. 1998;121(2):231-45. Epub 1998/06/06. doi: 10.1006/jsbi.1998.3972. PubMed PMID: 9615440.

10. Yeager M, Nicholson BJ. Structure of gap junction intercellular channels. Current Opinion in Structural Biology. 1996;6(2):183-92. doi: https://doi.org/10.1016/S0959-440X(96)80073-X.

11. Unger VM, Kumar NM, Gilula NB, Yeager M. Expression, two-dimensional crystallization, and electron cryo-crystallography of recombinant gap junction membrane channels. J Struct Biol. 1999;128(1):98-105. Epub 1999/12/22. doi: 10.1006/jsbi.1999.4184. PubMed PMID: 10600564.

12. Unwin PN, Ennis PD. Two configurations of a channel-forming membrane protein. Nature. 1984;307(5952):609-13. Epub 1984/02/16. PubMed PMID: 6320017.

13. Unger VM, Kumar NM, Gilula NB, Yeager M. Projection structure of a gap junction membrane channel at 7 A resolution. Nat Struct Biol. 1997;4(1):39-43. Epub 1997/01/01. PubMed PMID: 8989321.

14. Unger VM, Kumar NM, Gilula NB, Yeager M. Three-dimensional structure of a recombinant gap junction membrane channel. Science. 1999;283(5405):1176-80. PubMed PMID: 10024245.

15. Perkins GA, Goodenough DA, Sosinsky GE. Formation of the gap junction intercellular channel requires a 30 degree rotation for interdigitating two apposing connexons. Journal of molecular biology. 1998;277(2):171-7. Epub 1998/06/06. PubMed PMID: 9514740.

16. Fleishman SJ, Unger VM, Yeager M, Ben-Tal N. A C alpha model for the transmembrane alpha helices of gap junction intercellular channels. Molecular cell. 2004;15(6):879-88. doi: 10.1016/j.molcel.2004.08.016. PubMed PMID: 15383278.

17. Kronengold J, Trexler EB, Bukauskas FF, Bargiello TA, Verselis VK. Single-channel SCAM identifies pore-lining residues in the first extracellular loop and first transmembrane domains of Cx46 hemichannels. The Journal of general physiology. 2003;122(4):389-405. Epub 2003/09/17. doi: 10.1085/jgp.200308861. PubMed PMID: 12975451; PMCID: PMC2233777.

18. Maeda S, Nakagawa S, Suga M, Yamashita E, Oshima A, Fujiyoshi Y, Tsukihara T. Structure of the connexin 26 gap junction channel at 3.5 A resolution. Nature. 2009;458(7238):597-602. doi: 10.1038/nature07869. PubMed PMID: 19340074.

19. Verselis VK, Ginter CS, Bargiello TA. Opposite voltage gating polarities of two closely related connexins. Nature. 1994;368(6469):348-51. Epub 1994/03/24. doi: 10.1038/368348a0. PubMed PMID: 8127371.

20. Lin X, Fenn E, Veenstra RD. An amino-terminal lysine residue of rat connexin40 that is required for spermine block. The Journal of physiology. 2006;570(Pt 2):251-69. Epub 2005/11/15. doi: 10.1113/jphysiol.2005.097188. PubMed PMID: 16284078; PMCID: PMC1464307.

21. Gemel J, Lin X, Veenstra RD, Beyer EC. N-terminal residues in Cx43 and Cx40 determine physiological properties of gap junction channels, but do not influence heteromeric assembly with each other or with Cx26. J Cell Sci. 2006;119(Pt 11):2258-68. Epub 2006/05/26. doi: 10.1242/jcs.02953. PubMed PMID: 16723732; PMCID: PMC3237058.

22. Bargiello TA, Tang Q, Oh S, Kwon T. Voltage-dependent conformational changes in connexin channels. Biochimica et biophysica acta. 2012;1818(8):1807-22. Epub 2011/10/08. doi: 10.1016/j.bbamem.2011.09.019. PubMed PMID: 21978595; PMCID: PMC3367129.

23. Oshima A, Tani K, Hiroaki Y, Fujiyoshi Y, Sosinsky GE. Three-dimensional structure of a human connexin26 gap junction channel reveals a plug in the vestibule. Proceedings of the National Academy of Sciences of the United States of America. 2007;104(24):10034-9. doi: 10.1073/pnas.0703704104. PubMed PMID: 17551008; PMCID: 1886001.

24. Oshima A, Tani K, Toloue MM, Hiroaki Y, Smock A, Inukai S, Cone A, Nicholson BJ, Sosinsky GE, Fujiyoshi Y. Asymmetric configurations and N-terminal rearrangements in connexin26 gap junction channels. Journal of molecular biology. 2011;405(3):724-35. doi: 10.1016/j.jmb.2010.10.032. PubMed PMID: 21094651; PMCID: 3026138.

25. Moreno AP. Biophysical properties of homomeric and heteromultimeric channels formed by cardiac connexins. Cardiovasc Res. 2004;62(2):276-86. Epub 2004/04/20. doi: 10.1016/j.cardiores.2004.03.003. PubMed PMID: 15094348.

26. Muller A, Gottwald M, Tudyka T, Linke W, Klaus W, Dhein S. Increase in gap junction conductance by an antiarrhythmic peptide. Eur J Pharmacol. 1997;327(1):65-72. Epub 1997/05/26. PubMed PMID: 9185837.

27. Gomes J, Lambiase PD. Putative druggable targets for selective enhancement of cardiac conduction. Curr Opin Pharmacol. 2009;9(2):154-9. Epub 2008/12/26. doi: 10.1016/j.coph.2008.11.008. PubMed PMID: 19109070.

28. Hagen A, Dietze A, Dhein S. Human cardiac gap-junction coupling: effects of antiarrhythmic peptide AAP10. Cardiovasc Res. 2009;83(2):405-15. Epub 2009/01/30. doi: 10.1093/cvr/cvp028. PubMed PMID: 19176598.

29. Kjolbye AL, Haugan K, Hennan JK, Petersen JS. Pharmacological modulation of gap junction function with the novel compound rotigaptide: a promising new principle for prevention of arrhythmias. Basic Clin Pharmacol Toxicol. 2007;101(4):215-30. Epub 2007/09/12. doi: 10.1111/j.1742-7843.2007.00123.x. PubMed PMID: 17845503.

30. Locke D, Kieken F, Tao L, Sorgen PL, Harris AL. Mechanism for modulation of gating of connexin26-containing channels by taurine. The Journal of general physiology. 2011;138(3):321-39. doi: 10.1085/jgp.201110634. PubMed PMID: 21844220; PMCID: 3171079.

31. Morley GE, Ek-Vitorin JF, Taffet SM, Delmar M. Structure of connexin43 and its regulation by pHi. J Cardiovasc Electrophysiol. 1997;8(8):939-51. Epub 1997/08/01. PubMed PMID: 9261721.

32. Yeager M, Unger VM, Falk MM. Synthesis, assembly and structure of gap junction intercellular channels. Curr Opin Struct Biol. 1998;8(4):517-24. Epub 1998/09/08. PubMed PMID: 9729745.

33. Abrams CK, Islam M, Mahmoud R, Kwon T, Bargiello TA, Freidin MM. Functional Requirement for a Highly Conserved Charged Residue at Position 75 in the Gap Junction Protein Connexin 32. Journal of Biological Chemistry. 2013;288(5):3609-19. doi: 10.1074/jbc.M112.392670. PubMed PMID: WOS:000314397900065.

34. Ambrosi C, Walker AE, DePriest AD, Cone AC, Lu C, Badger J, Skerrett M, Sosinsky GE. Analysis of Trafficking, Stability and Function of Human Connexin 26 Gap Junction Channels with Deafness-Causing Mutations in the Fourth Transmembrane Helix. PloS one. 2013;8(8). doi: ARTN e70916

10.1371/journal.pone.0070916. PubMed PMID: WOS:000323378000024.

35. Sanchez HA, Bienkowski R, Slavi N, Srinivas M, Verselis VK. Altered inhibition of Cx26 hemichannels by pH and Zn2+ in the A40V mutation associated with keratitis-ichthyosis-deafness syndrome. The Journal of biological chemistry. 2014;289(31):21519-32. Epub 2014/06/19. doi: 10.1074/jbc.M114.578757. PubMed PMID: 24939841; PMCID: PMC4118113.

36. Muller DJ, Hand GM, Engel A, Sosinsky GE. Conformational changes in surface structures of isolated connexin 26 gap junctions. The EMBO Journal. 2002;21: 3598-607.

37. Barr L, Dewey MM, Berger W. Propagation of Action Potentials and the Structure of the Nexus in Cardiac Muscle. The Journal of general physiology. 1965;48:797-823. Epub 1965/05/01. PubMed PMID: 14324989; PMCID: PMC2213773.

38. Spach MS. The role of cell-to-cell coupling in cardiac conduction disturbances. Adv Exp Med Biol. 1983;161:61-77. Epub 1983/01/01. PubMed PMID: 6869083.

39. Severs NJ, Bruce AF, Dupont E, Rothery S. Remodelling of gap junctions and connexin expression in diseased myocardium. Cardiovasc Res. 2008;80(1):9-19. Epub 2008/06/04. doi: 10.1093/cvr/cvn133. PubMed PMID: 18519446; PMCID: PMC2533424.

40. Siddiqui A, Kowey PR. Sudden death secondary to cardiac arrhythmias: mechanisms and treatment strategies. Curr Opin Cardiol. 2006;21(5):517-25. Epub 2006/08/11. doi: 10.1097/01.hco.0000240591.06839.39. PubMed PMID: 16900017.

41. Arshad A, Mandava A, Kamath G, Musat D. Sudden cardiac death and the role of medical therapy. Prog Cardiovasc Dis. 2008;50(6):420-38. Epub 2008/05/14. doi: 10.1016/j.pcad.2007.12.003. PubMed PMID: 18474285.

42. Cascio WE, Johnson TA, Gettes LS. Electrophysiologic changes in ischemic ventricular myocardium: I. Influence of ionic, metabolic, and energetic changes. J Cardiovasc Electrophysiol. 1995;6(11):1039-62. Epub 1995/11/01. PubMed PMID: 8589873.

43. Myerburg RJ. Implantable cardioverter-defibrillators after myocardial infarction. N Engl J Med. 2008;359(21):2245-53. Epub 2008/11/21. doi: 10.1056/NEJMra0803409. PubMed PMID: 19020326.

44. Echt DS, Liebson PR, Mitchell LB, Peters RW, Obias-Manno D, Barker AH, Arensberg D, Baker A, Friedman L, Greene HL, et al. Mortality and morbidity in patients receiving encainide, flecainide, or placebo. The Cardiac Arrhythmia Suppression Trial. N Engl J Med. 1991;324(12):781-8. Epub 1991/03/21. doi: 10.1056/NEJM199103213241201. PubMed PMID: 1900101.

45. Cardiac Arrhythmia Suppression Trial III. Effect of the antiarrhythmic agent moricizine on survival after myocardial infarction. N Engl J Med. 1992;327(4):227-33. Epub 1992/07/23. doi: 10.1056/NEJM199207233270403. PubMed PMID: 1377359.

46. Harris A, Locke D. Connexins : a guide. New York, N.Y.: Springer; 2009. xvi, 573 p. p.

47. Stergiopoulos K, Alvarado JL, Mastroianni M, Ek-Vitorin JF, Taffet SM, Delmar M. Hetero-Domain Interactions as a Mechanism for the Regulation of Connexin Channels. Circulation Research. 1999;84(10):1144-55. doi: 10.1161/01.res.84.10.1144.

48. Werner R, Levine E, Rabadan-Diehl C, Dahl G. Gating properties of connexin32 cell-cell channels and their mutants expressed in Xenopus oocytes. Proc Biol Sci. 1991;243(1306):5-11. Epub 1991/01/22. doi: 10.1098/rspb.1991.0002. PubMed PMID: 1673244.

49. Sanchez HA, Slavi N, Srinivas M, Verselis VK. Syndromic deafness mutations at Asn 14 differentially alter the open stability of Cx26 hemichannels. The Journal of general physiology. 2016;148(1):25-42. doi: 10.1085/jgp.201611585. PubMed PMID: 27353444; PMCID: 4924935.

50. Bukauskas FF, Elfgang C, Willecke K, Weingart R. Biophysical Properties of Gap Junction Channels Formed by Mouse Connexin40 in Induced Pairs of Transfected Human Hela-Cells. Biophysical journal. 1995;68(6):2289-98. doi: Doi 10.1016/S0006-3495(95)80411-X. PubMed PMID: WOS:A1995RH66000010.

51. Veenstra RD. Size and selectivity of gap junction channels formed from different connexins. Journal of bioenergetics and biomembranes. 1996;28(4):327-37. Epub 1996/08/01. PubMed PMID: 8844330.

52. Beblo DA, Veenstra RD. Monovalent Cation Permeation through the Connexin40 Gap Junction Channel. The Journal of general physiology. 1997;109:509-22.

53. Wang HZ, Veenstra RD. Monovalent ion selectivity sequences of the rat connexin43 gap junction channel. The Journal of general physiology. 1997;109(4):491-507. Epub 1997/04/01. PubMed PMID: 9101407; PMCID: PMC2219435.

54. Benjamin W, Andrej S. Comparative Protein Structure Modeling Using MODELLER. Current Protocols in Bioinformatics. 2016;54(1):5.6.1-5.6.37. doi: doi:10.1002/cpbi.3.

55. Marti-Renom MA, Stuart AC, Fiser A, Sanchez R, Melo F, Sali A. Comparative protein structure modeling of genes and genomes. Annu Rev Biophys Biomol Struct. 2000;29:291-325. Epub 2000/08/15. doi: 10.1146/annurev.biophys.29.1.291. PubMed PMID: 10940251.

56. Laird DW, Naus CC, Lampe PD. SnapShot: Connexins and Disease. Cell. 2017;170(6). doi: ARTN 1260.e1

10.1016/j.cell.2017.08.034. PubMed PMID: WOS:000424595900001.

57. Chan DK, Chang KW. GJB2-Associated Hearing Loss: Systematic Review of Worldwide Prevalence, Genotype, and Auditory Phenotype. Laryngoscope. 2014;124(2):E34-E53. doi: 10.1002/lary.24332. PubMed PMID: WOS:000329929900003.

58. Xu J, Nicholson BJ. The role of connexins in ear and skin physiology - functional insights from disease-associated mutations. Biochimica et biophysica acta. 2013;1828(1):167-78. doi: 10.1016/j.bbamem.2012.06.024.

59. Lilly E, Sellitto C, Milstone LM, White TW. Connexin channels in congenital skin disorders. Semin Cell Dev Biol. 2016;50:4-12. Epub 2016/01/18. doi: 10.1016/j.semcdb.2015.11.018. PubMed PMID: 26775130; PMCID: PMC4779425.

60. Bergoffen J, Scherer SS, Wang S, Scott MO, Bone LJ, Paul DL, Chen K, Lensch MW, Chance PF, Fischbeck KH. Connexin mutations in X-linked Charcot-Marie-Tooth disease. Science. 1993;262(5142):2039-42. Epub 1993/12/24. PubMed PMID: 8266101.

61. Abrams CK, Freidin M. GJB1-associated X-linked Charcot-Marie-Tooth disease, a disorder affecting the central and peripheral nervous systems. Cell and tissue research. 2015;360(3):659-73. Epub 2014/11/06. doi: 10.1007/s00441-014-2014-6. PubMed PMID: 25370202.

62. Roa BB, Garcia CA, Suter U, Kulpa DA, Wise CA, Mueller J, Welcher AA, Snipes GJ, Shooter EM, Patel PI, Lupski JR. Charcot-Marie-Tooth Disease Type-1a - Association with a Spontaneous Point Mutation in the Pmp22 Gene. New Engl J Med. 1993;329(2):96-101. doi: Doi 10.1056/Nejm199307083290205. PubMed PMID: WOS:A1993LL19600005.

63. Kleopa KA, Abrams CK, Scherer SS. How do mutations in GJB1 cause X-linked Charcot-Marie-Tooth disease? Brain Res. 2012;1487:198-+. doi: 10.1016/j.brainres.2012.03.068. PubMed PMID: WOS:000313086800021.

64. Inherited Peripheral Neuropathies Mutation Database 2007. Available from: http://www.molgen.ua.ac.be/CMTMutations/Mutations/.

65. Nakagawa S, Gong XQ, Maeda S, Dong YH, Misumi Y, Tsukihara T, Bai DL. Asparagine 175 of Connexin32 Is a Critical Residue for Docking and Forming Functional Heterotypic Gap Junction Channels with Connexin26. Journal of Biological Chemistry.

2011;286(22):19672-81. doi: 10.1074/jbc.M110.204958. PubMed PMID: WOS:000291027700050.

66. Gong XQ, Nakagawa S, Tsukihara T, Bai DL. A mechanism of gap junction docking revealed by functional rescue of a human-disease-linked connexin mutant. Journal of Cell Science. 2013;126(14):3113-+. doi: 10.1242/jcs.123430. PubMed PMID: WOS:000321747400014.

67. Niemann A, Berger P, Suter U. Pathomechanisms of mutant proteins in Charcot-Marie-Tooth disease. NeuroMolecular Medicine. 2006;8(1):217-41. doi: 10.1385/nmm:8:1-2:217.

68. Sanchez HA, Bienkowski R, Slavi N, Srinivas M, Verselis VK. Altered Inhibition of Cx26 Hemichannels by pH and Zn2+ in the A40V Mutation Associated with Keratitis-Ichthyosis-Deafness Syndrome. The Journal of biological chemistry. 2014;289(31):21519-32. doi: 10.1074/jbc.M114.578757.

69. Purnick PE, Benjamin DC, Verselis VK, Bargiello TA, Dowd TL. Structure of the amino terminus of a gap junction protein. Archives of biochemistry and biophysics. 2000;381(2):181-90. doi: 10.1006/abbi.2000.1989. PubMed PMID: 11032405.

70. Gould TD, O'Donnell KC, Dow ER, Du J, Chen G, Manji HK. Involvement of AMPA receptors in the antidepressant-like effects of lithium in the mouse tail suspension test and forced swim test. Neuropharmacology. 2008;54(3):577-87. doi: 10.1016/j.neuropharm.2007.11.002. PubMed PMID: 18096191; PMCID: 2275050.

71. Shi JM, Pei J, Liu EQ, Zhang L. Bis(sulfosuccinimidyl) suberate (BS3) crosslinking analysis of the behavior of amyloid-beta peptide in solution and in

phospholipid membranes. PloS one. 2017;12(3):e0173871. doi: 10.1371/journal.pone.0173871. PubMed PMID: 28323849; PMCID: 5360245.

72. Schmidt C, Robinson CV. A comparative cross-linking strategy to probe conformational changes in protein complexes. Nature protocols. 2014;9(9):2224-36. doi: 10.1038/nprot.2014.144. PubMed PMID: 25144272; PMCID: 4172966.

73. Zhao A, Hao G, Gu J. Chemical crosslinking and mass spectrometric identification of interaction sites within soluble aggregate of protein therapeutics. Journal of pharmaceutical and biomedical analysis. 2013;73:99-102. doi: 10.1016/j.jpba.2012.05.006. PubMed PMID: 22677652.

74. Armstrong CM, Bezanilla F. Inactivation of the sodium channel. II. Gating current experiments. The Journal of general physiology. 1977;70(5):567-90. PubMed PMID: 591912; PMCID: 2228472.

75. Zagotta WN, Hoshi T, Aldrich RW. Restoration of inactivation in mutants of Shaker potassium channels by a peptide derived from ShB. Science. 1990;250(4980):568-71. PubMed PMID: 2122520.

76. Liu S, Taffet S, Stoner L, Delmar M, Vallano ML, Jalife J. A structural basis for the unequal sensitivity of the major cardiac and liver gap junctions to intracellular acidification: the carboxyl tail length. Biophysical journal. 1993;64(5):1422-33. doi: 10.1016/S0006-3495(93)81508-X. PubMed PMID: 8391867; PMCID: 1262467.

77. Ek-Vitorin JF, Calero G, Morley GE, Coombs W, Taffen SM, Delmar M. pH Regulation of Connexin43: Molecular Analysis of the Gating Particle. Biophysical journal. 1996;71:1273-84.

78. Chiu YH, Jin X, Medina CB, Leonhardt SA, Kiessling V, Bennett BC, Shu S, Tamm LK, Yeager M, Ravichandran KS, Bayliss DA. A quantized mechanism for activation of pannexin channels. Nature communications. 2017;8:14324. Epub 2017/01/31. doi: 10.1038/ncomms14324. PubMed PMID: 28134257; PMCID: PMC5290276.

79. Zhou M, Morais-Cabral JH, Mann S, MacKinnon R. Potassium channel receptor site for the inactivation gate and quaternary amine inhibitors. Nature. 2001;411(6838):657-61. doi: 10.1038/35079500. PubMed PMID: 11395760.

80. Noble D, Noble PJ. Late sodium current in the pathophysiology of cardiovascular disease: consequences of sodium-calcium overload. Heart. 2006;92 Suppl 4:iv1-iv5. Epub 2006/06/16. doi: 10.1136/hrt.2005.078782. PubMed PMID: 16775091; PMCID: PMC1861316.

81. Kalogeris T, Baines CP, Krenz M, Korthuis RJ. Cell biology of ischemia/reperfusion injury. International review of cell and molecular biology. 2012;298:229-317. Epub 2012/08/11. doi: 10.1016/B978-0-12-394309-5.00006-7. PubMed PMID: 22878108; PMCID: PMC3904795.

82. Tang G, Peng L, Baldwin PR, Mann DS, Jiang W, Rees I, Ludtke SJ. EMAN2: an extensible image processing suite for electron microscopy. Journal of Structural Biology. 2007;157(1):38-46. doi: 10.1016/j.jsb.2006.05.009.

83. Li X, Mooney P, Zheng S, Booth CR, Braunfeld MB, Gubbens S, Agard DA, Cheng Y. Electron counting and beam-induced motion correction enable near-atomic-resolution single-particle cryo-EM. Nature methods. 2013;10(6):584-90. doi: 10.1038/nmeth.2472. PubMed PMID: 23644547; PMCID: 3684049.

84. Rohou A, Grigorieff N. CTFFIND4: Fast and accurate defocus estimation from electron micrographs. J Struct Biol. 2015;192(2):216-21. doi: 10.1016/j.jsb.2015.08.008. PubMed PMID: 26278980.

85. Scheres SH. RELION: implementation of a Bayesian approach to cryo-EM structure determination. J Struct Biol. 2012;180(3):519-30. doi: 10.1016/j.jsb.2012.09.006. PubMed PMID: 23000701; PMCID: 3690530.

86. Kimanius D, Forsberg BO, Scheres SH, Lindahl E. Accelerated cryo-EM structure determination with parallelisation using GPUs in RELION-2. eLife. 2016;5. doi: 10.7554/eLife.18722. PubMed PMID: 27845625; PMCID: 5310839.

87. Fernandez-Leiro R, Scheres SHW. A pipeline approach to single-particle processing in RELION. Acta crystallographica Section D, Structural biology. 2017;73(Pt 6):496-502. doi: 10.1107/S2059798316019276. PubMed PMID: 28580911; PMCID: 5458491.

88. Zhang K. Gctf: Real-time CTF determination and correction. J Struct Biol. 2016;193(1):1-12. doi: 10.1016/j.jsb.2015.11.003. PubMed PMID: 26592709; PMCID: 4711343.

89. Scheres SH. Beam-induced motion correction for sub-megadalton cryo-EM particles. eLife. 2014;3:e03665. doi: 10.7554/eLife.03665. PubMed PMID: 25122622; PMCID: 4130160.

90. Rosenthal PB, Henderson R. Optimal determination of particle orientation, absolute hand, and contrast loss in single-particle electron cryomicroscopy. Journal of molecular biology. 2003;333(4):721-45. PubMed PMID: 14568533.

91. Pettersen EF, Goddard TD, Huang CC, Couch GS, Greenblatt DM, Meng EC, Ferrin TE. UCSF Chimera--a visualization system for exploratory research and analysis. Journal of Computational Chemistry. 2004;25(13):1605-12. doi: 10.1002/jcc.20084. PubMed PMID: 15264254.

92. Adams PD, Afonine PV, Bunkoczi G, Chen VB, Davis IW, Echols N, Headd JJ, Hung LW, Kapral GJ, Grosse-Kunstleve RW, McCoy AJ, Moriarty NW, Oeffner R, Read RJ, Richardson DC, Richardson JS, Terwilliger TC, Zwart PH. PHENIX: a comprehensive Python-based system for macromolecular structure solution. Acta Crystallographica Section D Biological Crystallography. 2010;66(Pt 2):213-21. doi: 10.1107/S0907444909052925.

93. Yonekura K, Maki-Yonekura S. Refinement of cryo-EM structures using scattering factors of charged atoms. Journal of Applied Crystallography. 2016;49(5):1517-23. doi: 10.1107/s1600576716011274.

94. Emsley P, Lohkamp B, Scott WG, Cowtan K. Features and development of Coot. Acta crystallographica Section D, Biological crystallography. 2010;66(Pt 4):486-501. doi: 10.1107/S0907444910007493. PubMed PMID: 20383002; PMCID: 2852313.

95. Chen VB, Arendall WB, 3rd, Headd JJ, Keedy DA, Immormino RM, Kapral GJ, Murray LW, Richardson JS, Richardson DC. MolProbity: all-atom structure validation for macromolecular crystallography. Acta Crystallographica Section D Biological Crystallography. 2010;66(Pt 1):12-21. doi: 10.1107/S0907444909042073.

96. Barad BA, Echols N, Wang RY, Cheng Y, DiMaio F, Adams PD, Fraser JS. EMRinger: side chain-directed model and map validation for 3D cryo-electron

microscopy. Nature methods. 2015;12(10):943-6. doi: 10.1038/nmeth.3541. PubMed PMID: 26280328; PMCID: 4589481.

97. Alexandrov AI, Mileni M, Chien EY, Hanson MA, Stevens RC. Microscale fluorescent thermal stability assay for membrane proteins. Structure. 2008;16(3):351-9. doi: 10.1016/j.str.2008.02.004.

98. Chalmers MJ, Busby SA, Pascal BD, He Y, Hendrickson CL, Marshall AG, Griffin PR. Probing protein ligand interactions by automated hydrogen/deuterium exchange mass spectrometry. Analytical chemistry. 2006;78(4):1005-14. doi: 10.1021/ac051294f. PubMed PMID: 16478090.

99. Busby SA, Chalmers MJ, Griffin PR. Improving digestion efficiency under H/D exchange conditions with activated pepsinogen coupled columns. International Journal of Mass Spectrometry. 2007;259(1-3):130-9. doi: 10.1016/j.ijms.2006.08.006.

100. Pascal BD, Willis S, Lauer JL, Landgraf RR, West GM, Marciano D, Novick S, Goswami D, Chalmers MJ, Griffin PR. HDX workbench: software for the analysis of H/D exchange MS data. Journal of the American Society for Mass Spectrometry. 2012;23(9):1512-21. doi: 10.1007/s13361-012-0419-6. PubMed PMID: 22692830; PMCID: 3808162.

101. West GM, Pascal BD, Ng LM, Soon FF, Melcher K, Xu HE, Chalmers MJ, Griffin PR. Protein conformation ensembles monitored by HDX reveal a structural rationale for abscisic acid signaling protein affinities and activities. Structure. 2013;21(2):229-35. doi: 10.1016/j.str.2012.12.001. PubMed PMID: 23290725; PMCID: 3570687.

102. Coales SJ, E SY, Lee JE, Ma A, Morrow JA, Hamuro Y. Expansion of time window for mass spectrometric measurement of amide hydrogen/deuterium exchange reactions.

Rapid communications in mass spectrometry : RCM. 2010;24(24):3585-92. doi: 10.1002/rcm.4814. PubMed PMID: 21108306.

103. Xu H, Freitas MA. MassMatrix: a database search program for rapid characterization of proteins and peptides from tandem mass spectrometry data. Proteomics. 2009;9(6):1548-55. doi: 10.1002/pmic.200700322. PubMed PMID: 19235167; PMCID: 2759086.

104. Kucukelbir A, Sigworth FJ, Tagare HD. Quantifying the local resolution of cryo-EM density maps. Nature methods. 2014;11(1):63-5. Epub 2013/11/12. doi: 10.1038/nmeth.2727. PubMed PMID: 24213166; PMCID: PMC3903095.

105. Banerjee S, Huber T, Sakmar TP. Rapid incorporation of functional rhodopsin into nanoscale apolipoprotein bound bilayer (NABB) particles. Journal of molecular biology. 2008;377(4):1067-81. doi: 10.1016/j.jmb.2008.01.066. PubMed PMID: WOS:000255108900008.

106. Ritchie TK, Grinkova YV, Bayburt TH, Denisov IG, Zolnerciks JK, Atkins WM, Sligar SG. Chapter 11 - Reconstitution of membrane proteins in phospholipid bilayer nanodiscs. Methods Enzymol. 2009;464:211-31. Epub 2009/11/12. doi: 10.1016/S0076-6879(09)64011-8. PubMed PMID: 19903557; PMCID: PMC4196316.

107. Gao Y, Cao E, Julius D, Cheng Y. TRPV1 structures in nanodiscs reveal mechanisms of ligand and lipid action. Nature. 2016;534(7607):347-51. Epub 2016/06/10. doi: 10.1038/nature17964. PubMed PMID: 27281200; PMCID: PMC4911334.

108. Liao M, Cao E, Julius D, Cheng Y. Structure of the TRPV1 ion channel determined by electron cryo-microscopy. Nature. 2013;504(7478):107-12. Epub 2013/12/07. doi: 10.1038/nature12822. PubMed PMID: 24305160; PMCID: PMC4078027.

109. McMullan G, Faruqi AR, Clare D, Henderson R. Comparison of optimal performance at 300keV of three direct electron detectors for use in low dose electron microscopy. Ultramicroscopy. 2014;147:156-63. doi: 10.1016/j.ultramic.2014.08.002. PubMed PMID: 25194828; PMCID: PMC4199116.

110. Meyerson JR, Rao P, Kumar J, Chittori S, Banerjee S, Pierson J, Mayer ML, Subramaniam S. Self-assembled monolayers improve protein distribution on holey carbon cryo-EM supports. Sci Rep. 2014;4:7084. Epub 2014/11/19. doi: 10.1038/srep07084. PubMed PMID: 25403871; PMCID: PMC4235105.

111. Bygrave FL, Benedetti A. What is the concentration of calcium ions in the endoplasmic reticulum? Cell Calcium. 1996;19(6):547-51. doi: https://doi.org/10.1016/S0143-4160(96)90064-0.

112. Xue S, Nicoud MR, Cui J, Jovin DJA. High concentration of calcium ions in Golgi apparatus. Cell Research. 1994;4:97. doi: 10.1038/cr.1994.10.

113. Kucharska I, Edrington TC, Liang B, Tamm LK. Optimizing nanodiscs and bicelles for solution NMR studies of two beta-barrel membrane proteins. J Biomol NMR. 2015;61(3-4):261-74. Epub 2015/04/15. doi: 10.1007/s10858-015-9905-z. PubMed PMID: 25869397; PMCID: PMC4397663.

114. Mastronarde DN. Automated electron microscope tomography using robust prediction of specimen movements. Journal of Structural Biology. 2005;152(1):36-51. doi: 10.1016/j.jsb.2005.07.007. PubMed PMID: WOS:000232572300004.

115. Zheng SQ, Palovcak E, Armache JP, Verba KA, Cheng Y, Agard DA. MotionCor2: anisotropic correction of beam-induced motion for improved cryo-electron microscopy. Nat Methods. 2017;14(4):331-2. doi: 10.1038/nmeth.4193. PubMed PMID: 28250466.

116. de la Rosa-Trevin JM, Quintana A, del Cano L, Zaldivar A, Foche I, Gutierrez J, Gomez-Blanco J, Burguet-Castell J, Cuenca-Alba J, Abrishami V, Vargas J, Oton J, Sharov G, Vilas JL, Navas J, Conesa P, Kazemi M, Marabini R, Sorzano COS, Carazo JM. Scipion: A software framework toward integration, reproducibility and validation in 3D electron microscopy. Journal of Structural Biology. 2016;195(1):93-9. doi: 10.1016/j.jsb.2016.04.010. PubMed PMID: WOS:000377735300010.

117. Punjani A, Rubinstein JL, Fleet DJ, Brubaker MA. cryoSPARC: algorithms for rapid unsupervised cryo-EM structure determination. Nat Methods. 2017;14(3):290-6. doi: 10.1038/nmeth.4169. PubMed PMID: 28165473.

118. Drozdetskiy A, Cole C, Procter J, Barton GJ. JPred4: a protein secondary structure prediction server. Nucleic acids research. 2015;43(W1):W389-94. Epub 2015/04/18. doi: 10.1093/nar/gkv332. PubMed PMID: 25883141; PMCID: PMC4489285.

119. Batir Y, Bargiello TA, Dowd TL. Structural studies of N-terminal mutants of Connexin 26 and Connexin 32 using (1)H NMR spectroscopy. Archives of biochemistry and biophysics. 2016;608:8-19. doi: 10.1016/j.abb.2016.06.019. PubMed PMID: 27378082; PMCID: 5051353.

120. Kwon T, Tang Q, Bargiello TA. Voltage-dependent gating of the Cx32*43E1 hemichannel: conformational changes at the channel entrances. The Journal of general physiology. 2013;141(2):243-59. Epub 2013/01/16. doi: 10.1085/jgp.201210839. PubMed PMID: 23319727; PMCID: PMC3557306.

121. Lee SC, Bennett BC, Hong WX, Fu Y, Baker KA, Marcoux J, Robinson CV, Ward AB, Halpert JR, Stevens RC, Stout CD, Yeager MJ, Zhang Q. Steroid-based facial amphiphiles for stabilization and crystallization of membrane proteins. Proceedings of the

National Academy of Sciences of the United States of America. 2013;110(13):E1203-11. Epub 2013/03/13. doi: 10.1073/pnas.1221442110. PubMed PMID: 23479627; PMCID: PMC3612649.

122. Zhang Q, Ma X, Ward A, Hong WX, Jaakola VP, Stevens RC, Finn MG, Chang G. Designing facial amphiphiles for the stabilization of integral membrane proteins. Angew Chem Int Ed Engl. 2007;46(37):7023-5. Epub 2007/08/11. doi: 10.1002/anie.200701556. PubMed PMID: 17691085.

123. Bao X, Reuss L, Altenberg GA. Regulation of purified and reconstituted connexin 43 hemichannels by protein kinase C-mediated phosphorylation of Serine 368. The Journal of biological chemistry. 2004;279(19):20058-66. Epub 2004/02/20. doi: 10.1074/jbc.M311137200. PubMed PMID: 14973142.

124. Bao X, Lee SC, Reuss L, Altenberg GA. Change in permeant size selectivity by phosphorylation of connexin 43 gap-junctional hemichannels by PKC. Proceedings of the National Academy of Sciences of the United States of America. 2007;104(12):4919-24. Epub 2007/03/16. doi: 10.1073/pnas.0603154104. PubMed PMID: 17360407; PMCID: PMC1817834.

125. Goehring A, Lee C, Wang KH, Michel JC, Claxton DP, Baconguis I, Althoff T, Fischer S, Garcia KC, Gouaux E. Screening and large-scale expression of membrane proteins in mammalian cells for structural studies. Nat Protoc. 2014;9(11):2574-85.

126. Paulsen CE, Armache JP, Gao Y, Cheng Y, Julius D. Structure of the TRPA1 ion channel suggests regulatory mechanisms. Nature. 2015.

127. Fletcher AJ, Christensen DE, Nelson C, Tan CP, Schaller T, Lehner PJ, Sundquist WI, Towers GJ. TRIM5alpha requires Ube2W to anchor Lys63-linked ubiquitin chains and

restrict reverse transcription. EMBO J. 2015;34(15):2078-95. doi: 10.15252/embj.201490361. PubMed PMID: 26101372; PMCID: 4551353.

128. Patel D, Zhang X, Veenstra RD. Connexin hemichannel and pannexin channel electrophysiology: How do they differ? Febs Letters. 2014;588(8):1372-8. doi: 10.1016/j.febslet.2013.12.023. PubMed PMID: WOS:000334317600023.

129. Liao M, Cao E, Julius D, Cheng Y. Single particle electron cryo-microscopy of a mammalian ion channel. Curr Opin Struct Biol. 2014;27:1-7. Epub 2014/04/01. doi: 10.1016/j.sbi.2014.02.005. PubMed PMID: 24681231; PMCID: PMC4176607.

130. Dukkipati A, Park HH, Waghray D, Fischer S, Garcia KC. BacMam system for high-level expression of recombinant soluble and membrane glycoproteins for structural studies. Protein Expr Purif. 2008;62(2):160-70. Epub 2008/09/11. doi: 10.1016/j.pep.2008.08.004. PubMed PMID: 18782620; PMCID: PMC2637115.

131. Goehring A, Lee CH, Wang KH, Michel JC, Claxton DP, Baconguis I, Althoff T, Fischer S, Garcia KC, Gouaux E. Screening and large-scale expression of membrane proteins in mammalian cells for structural studies. Nature protocols. 2014;9(11):2574-85. Epub 2014/10/10. doi: 10.1038/nprot.2014.173. PubMed PMID: 25299155; PMCID: PMC4291175.

132. John SA, Kondo R, Wang SY, Goldhaber JI, Weiss JN. Connexin-43 hemichannels opened by metabolic inhibition. Journal of Biological Chemistry. 1999;274(1):236-40. doi: DOI 10.1074/jbc.274.1.236. PubMed PMID: WOS:000077900200035.

133. Gatti-Lafranconi P. Pairwise distances - PyMOLWiki. Available from: https://pymolwiki.org/index.php/Pairwise_distances.

134. Schrodinger, LLC. The PyMOL Molecular Graphics System, Version 1.8. 2015.

135. Aldrich RW. Fifty years of inactivation. Nature. 2001;411(6838):643-4. Epub 2001/06/08. doi: 10.1038/35079705. PubMed PMID: 11395746.

136. Vallat B, Webb B, Westbrook JD, Sali A, Berman HM. Development of a Prototype System for Archiving Integrative/Hybrid Structure Models of Biological Macromolecules. Structure. 2018. Epub 2018/04/17. doi: 10.1016/j.str.2018.03.011. PubMed PMID: 29657133.

137. Kim SJ, Fernandez-Martinez J, Nudelman I, Shi Y, Zhang W, Raveh B, Herricks T, Slaughter BD, Hogan JA, Upla P, Chemmama IE, Pellarin R, Echeverria I, Shivaraju M, Chaudhury AS, Wang J, Williams R, Unruh JR, Greenberg CH, Jacobs EY, Yu Z, de la Cruz MJ, Mironska R, Stokes DL, Aitchison JD, Jarrold MF, Gerton JL, Ludtke SJ, Akey CW, Chait BT, Sali A, Rout MP. Integrative structure and functional anatomy of a nuclear pore complex. Nature. 2018;555(7697):475-82. Epub 2018/03/15. doi: 10.1038/nature26003. PubMed PMID: 29539637.

138. Chan DK, Schrijver I, Chang KW. Connexin-26-associated deafness: phenotypic variability and progression of hearing loss. Genetics in medicine : official journal of the American College of Medical Genetics. 2010;12(3):174-81. doi: 10.1097/GIM.0b013e3181d0d42b. PubMed PMID: 20154630.

139. Sosinsky GE, Nicholson BJ. Structural organization of gap junction channels. Biochimica et biophysica acta. 2005;1711(2):99-125. doi: 10.1016/j.bbamem.2005.04.001. PubMed PMID: 15925321.

140. Lopez W, Liu Y, Harris AL, Contreras JE. Divalent regulation and intersubunit interactions of human connexin26 (Cx26) hemichannels. Channels (Austin). 2014;8(1):1-

4. Epub 2013/10/16. doi: 10.4161/chan.26789. PubMed PMID: 24126106; PMCID: PMC4048337.

141. Tao L, Harris AL. 2-aminoethoxydiphenyl borate directly inhibits channels composed of connexin26 and/or connexin32. Mol Pharmacol. 2007;71(2):570-9. Epub 2006/11/11. doi: 10.1124/mol.106.027508. PubMed PMID: 17095584.

142. Yu J, Bippes CA, Hand GM, Muller DJ, Sosinsky GE. Aminosulfonate modulated pH-induced conformational changes in connexin26 hemichannels. The Journal of biological chemistry. 2007;282(12):8895-904. doi: 10.1074/jbc.M609317200. PubMed PMID: 17227765.

143. Bastiaanse EML, Jongsma HJ, Vanderlaarse A, Takenskwak BR. Heptanol-Induced Decrease in Cardiac Gap Junctional Conductance Is Mediated by a Decrease in the Fluidity of Membranous Cholesterol-Rich Domains. J Membrane Biol. 1993;136(2):135-45. doi: Doi 10.1007/Bf02505758. PubMed PMID: WOS:A1993MH77000004.

144. Lee SC, Knowles TJ, Postis VLG, Jamshad M, Parslow RA, Lin YP, Goldman A, Sridhar P, Overduin M, Muench SP, Dafforn TR. A method for detergent-free isolation of membrane proteins in their local lipid environment. Nature protocols. 2016;11(7):1149-62. doi: 10.1038/nprot.2016.070. PubMed PMID: WOS:000377489200001.

145. Stroud Z, Hall SCL, Dafforn TR. Purification of membrane proteins free from conventional detergents: SMA, new polymers, new opportunities and new insights. Methods. 2018. doi: https://doi.org/10.1016/j.ymeth.2018.03.011.

146. Parmar M, Rawson S, Scarff CA, Goldman A, Dafforn TR, Muench SP, Postis VLG. Using a SMALP platform to determine a sub-nm single particle cryo-EM membrane

protein structure. Bba-Biomembranes. 2018;1860(2):378-83. doi: 10.1016/j.bbamem.2017.10.005. PubMed PMID: WOS:000424183500016.

147. Russo CJ, Passmore LA. Robust evaluation of 3D electron cryomicroscopy data using tilt-pairs. J Struct Biol. 2014;187(2):112-8. doi: 10.1016/j.jsb.2014.06.006. PubMed PMID: 25016098; PMCID: PMC4136738.

148. Scheres SH. A Bayesian view on cryo-EM structure determination. J Mol Biol. 2012;415(2):406-18. doi: 10.1016/j.jmb.2011.11.010. PubMed PMID: 22100448; PMCID: 3314964.

149. Vinothkumar KR, Henderson R. Single particle electron cryomicroscopy: trends, issues and future perspective. Q Rev Biophys. 2016;49:e13. doi: 10.1017/S0033583516000068. PubMed PMID: 27658821.

150. Suloway C, Pulokas J, Fellmann D, Cheng A, Guerra F, Quispe J, Stagg S, Potter CS, Carragher B. Automated molecular microscopy: the new Leginon system. J Struct Biol. 2005;151(1):41-60. doi: 10.1016/j.jsb.2005.03.010. PubMed PMID: 15890530.

151. Li X, Mooney P, Zheng S, Booth CR, Braunfeld MB, Gubbens S, Agard DA, Cheng Y. Electron counting and beam-induced motion correction enable near-atomic-resolution single-particle cryo-EM. NatMethods. 2013;10(6):584-90.

152. Grant T, Grigorieff N. Measuring the optimal exposure for single particle cryo-EM using a 2.6 A reconstruction of rotavirus VP6. Elife. 2015;4:e06980. doi: 10.7554/eLife.06980. PubMed PMID: 26023829; PMCID: PMC4471936.

153. Ludtke SJ, Baldwin PR, Chiu W. EMAN: semiautomated software for high-resolution single-particle reconstructions. J Struct Biol. 1999;128(1):82-97. doi: 10.1006/jsbi.1999.4174. PubMed PMID: 10600563.

154. Tang G, Peng L, Baldwin PR, Mann DS, Jiang W, Rees I, Ludtke SJ. EMAN2: an extensible image processing suite for electron microscopy. J Struct Biol. 2007;157(1):38-46. doi: 10.1016/j.jsb.2006.05.009. PubMed PMID: 16859925.

155. Scheres SH. Processing of Structurally Heterogeneous Cryo-EM Data in RELION. Methods Enzymol. 2016;579:125-57. doi: 10.1016/bs.mie.2016.04.012. PubMed PMID: 27572726.

156. Bell JM, Chen M, Baldwin PR, Ludtke SJ. High resolution single particle refinement in EMAN2.1. Methods. 2016;100:25-34. doi: 10.1016/j.ymeth.2016.02.018. PubMed PMID: 26931650; PMCID: PMC4848122.

157. Wasilewski S, Rosenthal PB. Web server for tilt-pair validation of single particle maps from electron cryomicroscopy. J Struct Biol. 2014;186(1):122-31. doi: 10.1016/j.jsb.2014.02.012. PubMed PMID: 24582855.

158. Emsley P, Cowtan K. Coot: model-building tools for molecular graphics. Acta Crystallogr D Biol Crystallogr. 2004;60(Pt 12 Pt 1):2126-32. doi: 10.1107/S0907444904019158. PubMed PMID: 15572765.

159. Adams PD, Afonine PV, Bunkoczi G, Chen VB, Davis IW, Echols N, Headd JJ, Hung LW, Kapral GJ, Grosse-Kunstleve RW, McCoy AJ, Moriarty NW, Oeffner R, Read RJ, Richardson DC, Richardson JS, Terwilliger TC, Zwart PH. PHENIX: a comprehensive Python-based system for macromolecular structure solution. Acta Crystallogr D Biol Crystallogr. 2010;66(Pt 2):213-21. doi: 10.1107/S0907444909052925. PubMed PMID: 20124702; PMCID: PMC2815670.

160. Winn MD, Ballard CC, Cowtan KD, Dodson EJ, Emsley P, Evans PR, Keegan RM, Krissinel EB, Leslie AG, McCoy A, McNicholas SJ, Murshudov GN, Pannu NS, Potterton

EA, Powell HR, Read RJ, Vagin A, Wilson KS. Overview of the CCP4 suite and current developments. Acta Crystallogr D Biol Crystallogr. 2011;67(Pt 4):235-42. doi: 10.1107/S0907444910045749. PubMed PMID: 21460441; PMCID: PMC3069738.